

DIFFERENCES BETWEEN SATELLITE MEASUREMENTS AND
THEORETICAL ESTIMATES OF GLOBAL CLOUD LIQUID WATER AMOUNTS

by

Ákos Horváth

Copyright © Ákos Horváth 2004

A Dissertation Submitted to the Faculty of the
DEPARTMENT OF ATMOSPHERIC SCIENCES

In Partial Fulfillment of the Requirements
For the Degree of

DOCTOR OF PHILOSOPHY

In the Graduate College

THE UNIVERSITY OF ARIZONA

2004

UMI Number: 3132230

Copyright 2004 by
Horvath, Akos

All rights reserved.

INFORMATION TO USERS

The quality of this reproduction is dependent upon the quality of the copy submitted. Broken or indistinct print, colored or poor quality illustrations and photographs, print bleed-through, substandard margins, and improper alignment can adversely affect reproduction.

In the unlikely event that the author did not send a complete manuscript and there are missing pages, these will be noted. Also, if unauthorized copyright material had to be removed, a note will indicate the deletion.

UMI[®]

UMI Microform 3132230

Copyright 2004 by ProQuest Information and Learning Company.

All rights reserved. This microform edition is protected against
unauthorized copying under Title 17, United States Code.

ProQuest Information and Learning Company
300 North Zeeb Road
P.O. Box 1346
Ann Arbor, MI 48106-1346

The University of Arizona ®
Graduate College

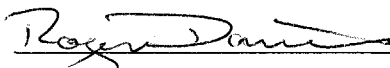
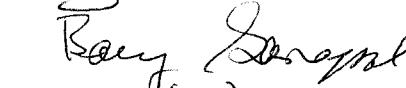
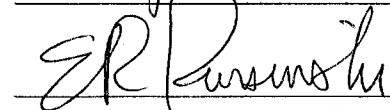
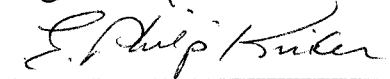
As members of the Final Examination Committee, we certify that we have read the

dissertation prepared by Akos Horvath

entitled DIFFERENCES BETWEEN SATELLITE MEASUREMENTS AND
THEORETICAL ESTIMATES OF GLOBAL CLOUD LIQUID WATER AMOUNTS

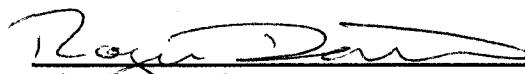
and recommend that it be accepted as fulfilling the dissertation requirement for the

Degree of Doctor of Philosophy

	<u>Roger Davies</u>	<u>4/12/04</u> date
	<u>Barry Ganapol</u>	<u>4/12/04</u> date
	<u>Robert Kursinski</u>	<u>4/12/04</u> date
	<u>Philip Krider</u>	<u>4/12/04</u> date
		<u> </u> date

Final approval and acceptance of this dissertation is contingent upon the candidate's submission of the final copies of the dissertation to the Graduate College.

I hereby certify that I have read this dissertation prepared under my direction and recommend that it be accepted as fulfilling the dissertation requirement.

	<u>Roger Davies</u>	<u>5/11/04</u>
Dissertation Director:		date

STATEMENT BY AUTHOR

This dissertation has been submitted in partial fulfillment of requirements for an advanced degree at The University of Arizona and is deposited in the University Library to be made available to borrowers under rules of the Library.

Brief quotations from this dissertation are allowable without special permission, provided that accurate acknowledgment of source is made. Requests for permission for extended quotation from or reproduction of this manuscript in whole or in part may be granted by the copyright holder.

SIGNED: Alus Hovakimyan

ACKNOWLEDGEMENTS

First and foremost, I would like to thank my family. My parents, Mária Fischer and János Horváth, my brother, Gábor Horváth, and my fiancée, Cynthia J. Archerd, each provided invaluable emotional support during the course of my work, especially when I was coping with homesickness. Second, many thanks go to my supervisor, Professor Roger Davies. He has been a true scientific mentor who has taught me not only technical skills, but also to consistently aim for quality work. Third, Catherine M. Moroney deserves credit for her considerable computational help and friendship over the years. Finally, I thank the entire MISR (Multiangle Imaging SpectroRadiometer) team, and David J. Diner in particular, for their scientific and financial support throughout my graduate studies.

MISR data were provided by the Atmospheric Sciences Data Center (ASDC) at NASA Langley Research Center. SSM/I data and images were produced by Remote Sensing Systems and sponsored by the NASA Pathfinder Program for early Earth Observing System (EOS) products. TMI data and images were produced by Remote Sensing Systems and sponsored by NASA's Earth Science Information Partnerships (ESIP): a federation of information sites for Earth Science, and by NASA's TRMM Science Team.

TABLE OF CONTENTS

LIST OF FIGURES	7
LIST OF TABLES	10
ABSTRACT	12
CHAPTER 1 INTRODUCTION	14
CHAPTER 2 LITERATURE REVIEW	21
2.1 Definition of Key Terms	21
2.2 The Measurement of Cloud Liquid Water Path	25
2.2.1 Aircraft Observations	25
2.2.2 Rawinsonde Measurements	26
2.2.3 Optical Technique	27
2.2.4 Microwave Technique	30
2.3 Global Cloud Liquid Water Estimates	33
CHAPTER 3 METHODOLOGY	50
3.1 Instrument and Dataset Overview	50
3.1.1 The Multiangle Imaging SpectroRadiometer	50
3.1.2 Dataset	54
3.2 Cloud Optical Thickness Retrieval	56
3.2.1 Lookup-Table Interpolation Method	56
3.2.2 Specification of Model Cloud Microphysics	60

TABLE OF CONTENTS - *Continued*

3.3 Atmospheric Correction	69
3.3.1 Ozone Correction	69
3.3.2 Water Vapor Correction.....	76
3.3.3 Rayleigh Correction	78
CHAPTER 4 RESULTS	86
4.1 Improving the Theoretical Estimate	86
4.2 Angular Consistency Study	108
4.3 Comparison of the Optical and Microwave Techniques.....	108
4.4 Global Optical Thickness Distributions	121
CHAPTER 5 SUMMARY AND CONCLUSIONS	133
APPENDIX A: GLOSSARY	143
APPENDIX B: IMAGE COREGISTRATION.....	147
APPENDIX C: CALCULATION OF COLUMNAR OZONE.....	151
APPENDIX D: THE RAYLEIGH CORRECTION ALGORITHM	160
APPENDIX E: ANGULAR CONSISTENCY STUDY	173
APPENDIX F: REMAPPING ALGORITHM.....	190
APPENDIX G: OFF-AXIS CORRECTION	196
REFERENCES.....	202

LIST OF FIGURES

Figure 2.1 Estimates of global mean atmospheric liquid water path.....	35
Figure 3.1 The MISR instrument on the Terra satellite.....	51
Figure 3.2 MISR imaging concept.....	53
Figure 3.3 Processed MISR orbits: 6956-6969 (red), and 15330-15343 (blue).....	55
Figure 3.4 (a) Red band spectral radiance as a function of cloud optical thickness; (b) Relative error of spline interpolation as a function of cloud optical thickness.....	59
Figure 3.5 Single scattering phase functions at $\lambda = 672$ nm.....	62
Figure 3.6 Chappuis band ozone absorption cross-section.....	70
Figure 3.7 Ozone absorption as a function of solar zenith angle.....	73
Figure 3.8 Relative error (in percent) in retrieved cloud optical thickness: (a) without Rayleigh correction, and (b) with Rayleigh correction.....	80
Figure 3.9 Effect of Rayleigh correction on optical thickness distributions.....	82-83
Figure 3.10 Angular cloud optical thickness distributions: (a) without Rayleigh correction, and (b) with Rayleigh correction.....	85
Figure 4.1 Comparison of MISR <i>LWP</i> and TMI <i>LWP</i> for a non-precipitating marine Sc field.....	110
Figure 4.2 (a) MISR nadir optical thickness, (b) TMI liquid water path, and (c) TMI rain rate for a precipitating Cb field.....	112
Figure 4.3 Comparison of MISR <i>LWP</i> and TMI <i>LWP</i> for the precipitating Cb field shown in Figure 4.2. (a) Using a fixed effective radius of $R_e = 8$ μm , and (b) using the parameterization in equation (4.2).....	114
Figure 4.4 (a) Histograms, and (b) cumulative histograms of nadir (A_n) optical thicknesses for the 28 MISR orbits	122
Figure 4.5 (a) Histograms, and (b) cumulative histograms of nadir (A_n) optical thicknesses for water clouds (black), and for the combination of water clouds and the water component of ice/mixed-phase clouds (green).....	125

LIST OF FIGURES - *Continued*

Figure 4.6 Cumulative histograms of the nadir (green), and the minimum (red) and maximum (blue) optical thicknesses for the 28 MISR orbits.....	127
Figure 4.7 Extrapolated cumulative histograms of the nadir, the minimum, and the maximum optical thicknesses.....	131
Figure 5.1 Summary of the main limitations of satellite retrieval techniques.....	137
Figure B1 MISR wind retrieval for block 116 of orbit 15331.....	149
Figure B2 Coregistration example for a mesoscale domain from block 116 of orbit 15331.....	150
Figure C1 The WCRP solar spectral irradiance $I_{0,\lambda}$ vs. wavelength.....	153
Figure C2 TOMS total ozone maps (in DU) for April 9, 2001. (a) Original data, and (b) data gaps filled.....	157
Figure C3 TOMS total ozone maps (in DU) for November 5, 2002. (a) Original data, and (b) data gaps filled.....	158
Figure D1 Rayleigh phase function and water cloud phase function at a wavelength of $\lambda = 0.672 \mu\text{m}$ (MISR red band) vs. scattering angle.....	163
Figure D2 Cloud plane albedo as a function of the cosine of the solar zenith angle for various cloud optical thicknesses and droplet effective radii.....	169
Figure D3 Convergence of the Rayleigh correction algorithm. (a) Thin faint cloud; (b) Thick bright cloud.....	172
Figure E1 Comparison of measured and plane-parallel angular reflectances at a resolution of 275 m. (a) Cloud passes the angular test. (b) Cloud fails the angular test.....	178
Figure E2 Angular test passing rate vs. pixel resolution for $R_e=8 \mu\text{m}$	182
Figure E3 Angular test passing rate vs. number of cameras for $R_e=8 \mu\text{m}$	184
Figure F1 Remapping example for block 117 of orbit 15338. (a) MISR red band BRFs at a resolution of 1.1 km, and (b) MODIS red band BRFs remapped to the MISR grid.....	192

LIST OF FIGURES - *Continued*

Figure F2 (a) Remapped MODIS cloud phase, (b) MISR red band Df BRFs, and (c) MISR red band Da BRFs for block 117 of orbit 15338.....	194
Figure F3 (a) Remapped MODIS cloud top pressure, and (b) remapped TOMS total column ozone for block 117 of orbit 15338.....	195
Figure G1 (a) Old and new calibration coefficients, and correction factor for the nadir camera, and (b) correction factors for the nine MISR cameras.....	199
Figure G2 Off-axis calibration correction of block 116 of orbit 6968.....	200

LIST OF TABLES

Table 2.1 History of global liquid water path estimates.....	34
Table 3.1 Solar spectral irradiance I_0 for the MISR channels.....	57
Table 3.2 Look-up table characteristics.....	57
Table 3.3 Droplet effective radius, asymmetry factor, and relative change in retrieved cloud optical thickness.....	67
Table 3.4 Ozone absorption for a clear tropical atmosphere above a sea surface as calculated by SBDART and equation (3.5).....	75
Table 3.5 Ozone absorption as a function of cloud height as calculated by SBDART for a tropical atmosphere, a cloud with $\tau_c = 50$, $R_e = 10 \mu\text{m}$, C1 phase function, and $\theta_0 = 0^\circ, \theta = 0^\circ, \Delta\phi = 0^\circ$	75
Table 3.6 Water vapor (WV) absorption in the MISR red band for a clear tropical atmosphere above a sea surface as calculated by SBDART and MODTRAN.....	77
Table 4.1 Global average cloud amount, cloud thickness, cloud liquid water content, and cloud liquid water path from PJ95.....	88
Table 4.2 Cloud type amounts (%) according to PJ95, Warren's surface climatology, and ISCCP-D2 satellite dataset.....	90
Table 4.3 Cloud liquid water path (g/m^2) as calculated from equation (4.1) using cloud amounts from PJ95, Warren's surface climatology, and ISCCP-D2 satellite dataset (see Table 4.2). All other parameters are unchanged and are as indicated in Table 4.1	93
Table 4.4 Typical values of cloud liquid water content (g/m^3) published in the literature.....	95
Table 4.5 Cloud liquid water path (g/m^2) as calculated from equation (4.1) using cloud thicknesses from Table 4.1, cloud amounts from Table 4.2, and the minimum cloud liquid water values from Table 4.4.....	97
Table 4.6 Cloud layer thickness according to PJ95, and Poore et al. (1995).....	100
Table 4.7 Cloud liquid water path (g/m^2) as calculated from equation (4.1) using cloud amounts from Table 4.2, the minimum cloud liquid water values from Table 4.4, and the minimum cloud thicknesses (column 4) from Table 4.6.....	103

LIST OF TABLES - *Continued*

Table 4.8 Best guess values for cloud amount, cloud thickness, and cloud liquid water content and the resulting cloud liquid water paths.....	105
Table 4.9 Global average cloud liquid water path (g/m^2) as determined by various instruments for April 9, 2001.....	117
Table 4.10 Global mean atmospheric liquid water path (g/m^2) estimates based on extrapolating the truncated optical thickness distributions.....	131
Table C1 Values of c_λ for MISR and AVHRR channels at various temperatures as calculated from equation (C2).....	153
Table C2 Ozone-weighted average temperature and total column ozone abundance for various atmospheric models.....	156
Table D1 Rayleigh optical thickness for the MISR channels.....	167
Table E1 Average passing rate at a resolution of 275 m vs. effective radius.....	180

ABSTRACT

This dissertation investigated the estimation of global cloud water amounts. The study was prompted by the large discrepancy in published global mean values of cloud liquid water path. Microwave and optical satellite measurements of this quantity range from 25 g/m^2 to 80 g/m^2 . Theoretical estimates are significantly larger with a current best guess value of 380 g/m^2 .

The major limitations of microwave measurements were found to be the inadequate separation of the cloud- and rainwater components, and the lack of retrievals over land. Optical observations were found to be constrained by the truncation of retrieved optical thickness due to saturation effects, the limited knowledge of drop effective radius as a function of optical thickness and rain rate, and plane-parallel retrieval errors due to 3D effects.

An analysis of the potential uncertainties concluded that the current theoretical estimate of the global mean cloud liquid water path of 380 g/m^2 was reasonable with an uncertainty of $\pm 80 \text{ g/m}^2$. Errors in the optical retrievals due to 3D effects were estimated using a multiangle data set. A microwave-optical comparison revealed that a drop effective radius significantly larger than the common assumption of $8\text{--}10 \text{ }\mu\text{m}$ was required to remove the low bias of optical retrievals of cloud liquid water in precipitating systems. The low bias due to saturation effects was accounted for by sigmoidal extrapolation of the cumulative distribution of cloud optical thickness. Overall it was found that the optical measurement of the global mean cloud liquid water path could be increased to a maximum of 150 g/m^2 over the oceans.

The failure to close the gap between satellite measurements and theoretical estimates can partly be attributed to, but cannot be completely explained by, the lack of the most intense continental clouds in the ocean-only data set used in this study. It is unlikely that optical measurements can be corrected to accurately retrieve the largest liquid water amounts. New techniques are required to handle the wettest precipitating clouds.

CHAPTER 1 INTRODUCTION

Clouds play an important role in the climate system by influencing both the hydrological cycle and the radiation budget. Our knowledge of global cloudiness, however, is still rather limited. In fact, the poor treatment of clouds in Global Climate Models (GCMs) was stated by the Intergovernmental Panel on Climate Change (IPCC) as the primary cause of uncertainty in future climate change predictions (Houghton, 2001). The picture emerging about global cloudiness from the ever-increasing amount of satellite observations is, in several ways, in contrast with traditional microphysical theory. For instance, there is no consensus regarding the magnitude of the various components of atmospheric hydrology. The primary focus of this dissertation was to investigate the reasons behind large differences between satellite measurements and theoretical estimates of the amount of liquid water stored in clouds globally. The water stored in the ice phase was beyond the scope of this study. The vast majority of this cloud liquid water resides in the lower 6 km of the atmosphere. Its amount is usually expressed in terms of the mass of liquid water in an atmospheric column over a unit area of the earth. This columnar quantity is called the *cloud liquid water path* (given in g/m^2), which is the vertical integral of the cloud liquid water density (given in g/m^3) alternatively known as the cloud liquid water content.

From a climatological point of view the global cloud liquid water has to satisfy two general constraints. First, at the lower boundary it has to produce the observed annual mean value of surface precipitation. This quantity can be considered as relatively well established, although its historical estimates made by various authors vary from 784

mm/yr to 1130 mm/yr (Hulme, 1995). Recent estimates show a narrower range of uncertainty in annual rainfall from 966 mm/yr to 1041 mm/yr with the latest IPCC report using a value of 984 mm/yr. This canonical value of ~ 1 m/yr global rainfall must be balanced by the same global mean evaporation rate. Second, clouds have to produce the observed shortwave and longwave radiative fluxes at the top of the atmosphere (TOA). These fluxes have been relatively precisely measured by the Earth Radiation Budget Experiment (ERBE) in recent years. An improved version of this experiment, the Clouds and the Earth's Radiant Energy System (CERES), is currently flying on several satellites and is expected to provide TOA radiative fluxes with a factor of 2 to 3 less error than the ERBE (Wielicki et al., 1996).

The problem is that these two relatively precisely known boundary conditions (surface rainfall, and TOA radiative fluxes) alone do not constrain the global mean amount of cloud liquid water well enough. The same global precipitation rate can be maintained by different amounts of atmospheric liquid water. The rainfall rate and cloud liquid water are linked together by the residence time of cloud water with respect to precipitation. A climate with a smaller atmospheric liquid water amount would be characterized by a shorter residence time and a larger annual number of less intensive precipitation events. In case of a larger atmospheric liquid water content the residence time would be longer and the cloud water has to undergo fewer but more intensive precipitation events. The precise value of the residence time of cloud water with respect to precipitation is not known, therefore both a drier and a wetter scenario are possible with the given rainfall rate. Similarly, the observed TOA radiative fluxes can be obtained

by various amounts of cloud water depending primarily on the average size of cloud droplets and the volume distribution of cloud water. Generally speaking, a smaller (effective) drop radius results in brighter clouds. Thus, if the global cloud water mass is distributed into smaller particles a smaller cloud water mass is required to match the measured shortwave TOA fluxes. Conversely, larger cloud drops would require a larger amount of atmospheric cloud water. The globally characteristic value of cloud drop effective radius is also unknown. Cloud brightness also depends on the spatial distribution of cloud water. Spatially homogeneous clouds are usually brighter than heterogeneous clouds for the same liquid water amount. The importance of heterogeneity effects on climate is still an area of intensive research. In summary, the annual mean surface rain rate and the measured TOA fluxes alone do not put hard constraints on the amount of cloud liquid water and allow a wide range of values for this quantity.

Cloud liquid water content thus has to be measured. The measurement of this quantity is problematic because it constitutes only a very small portion of the precipitable water. The global annual-mean precipitable water (vapor) content of the atmosphere is estimated to be 25 kg/m^2 (Peixoto and Oort, 1992). This value is about two orders of magnitude larger than typical estimates of the global mean cloud liquid water amount. Locally, the annual-mean precipitable water can vary from 2.5 kg/m^2 at the poles to 50 kg/m^2 in the Tropics. Locally, too, the time-mean amount of cloud liquid water seems to be no more than a couple of percent of the total water vapor. This means that a small relative change in the global atmospheric water vapor content can potentially result in a very large absolute change in the global cloud liquid water amount. The most precise

measurements of cloud liquid water path are probably obtained from ground-based passive microwave observations and from integrating in-situ aircraft measurements of cloud liquid water density profiles. These observations, however, are rare and thus plagued by serious undersampling. Global coverage can only be achieved with the help of satellite observations. The problem with satellite retrievals is that cloud liquid water path is usually not the main focus of these measurements. Microwave techniques are primarily devised to retrieve rainfall and thus are tuned to produce the observed annual precipitation rate. Optical techniques, which retrieve cloud optical thickness, are tuned to give the observed TOA brightness within the framework of existing (1-D plane-parallel) climate model radiative transfer parameterizations. Consequently, cloud liquid water path is obtained from these retrievals only as some sort of a residual parameter; a treatment that does not reflect the importance of this quantity. As a result of the above, current estimates of the global mean cloud liquid water path show a wide range of variation from as low as 25 g/m^2 (satellite) to as high as 382 g/m^2 (theoretical). Clearly, there is a problem here as demonstrated by the factor of 15 difference between the low and high end of the estimates.

The importance of knowing the global distribution and global mean value of cloud liquid water path is threefold. First and foremost, the generation/prediction of a given amount of liquid water path (condensed water) in a grid box is the first in a series of steps a climate model pass through to ultimately calculate the effect of clouds on the radiative fluxes at the TOA. The absolute amount of cloud liquid water has a direct effect on the overall magnitude of the cloud radiative feedback mechanisms. A climate system

with a smaller amount of cloud water is expected to be more sensitive to changes than one with a larger amount of water stored in clouds. The now classic example of the intercomparison of 19 climate models in Cess et al. (1990) showed a factor of 3 to 4 variation in the modeled sensitivity of the earth's climate. The source of this variation was traced back to considerable differences in the model's depictions of cloud feedback. An update of this comparison (Cess et al., 1996) found smaller differences in net cloud feedback, however, it still reported substantial differences in the (shortwave/longwave) feedback components, indicating that the models still had physical disagreements. The large variations among the different models and among the progressive versions of a given model were attributed to a large extent to differences in the amount of the produced cloud liquid water.

Second, there is growing evidence that clouds play a significant role in the processing of aerosols and other chemical processes in the atmosphere. It has been found, for instance, that the size distribution of aerosol particles entering a cloud can alter significantly after the evaporation of the cloud (e.g. Pruppacher and Jaenicke, 1995 and references therein). In this context, the number of times aerosols are cycled through clouds is a crucial parameter. The number of processing cycles, in turn, depends on the global amount of cloud liquid water and its residence time with respect to condensation, evaporation, and precipitation.

Finally, a well-established global mean value of cloud liquid water amount could be used in climate model validation. One way of determining if the physics built in a model is realistic is to compare certain bulk parameters, e.g. cloud liquid water, surface

precipitation, etc., computed by the model with long-term averages of the same variable obtained from observations. If the climate model is to achieve the highest degree of realism, its cloud parameterization must be able to produce the proper amount of cloud water and simultaneously satisfy the constraints represented by the annual-mean rain rate and by the radiative fluxes at the TOA. Although current climate models are far from this state of realism, the expectation is that they are progressing towards this goal.

In summary, cloud liquid water path is an important parameter in the understanding of atmospheric chemistry and cloud feedback processes. It is also crucial to improve the parameterization of cloud generation, precipitation, and cloud-radiative interactions in climate models. The importance of cloud liquid water path was underlined by the fact that the National Aeronautics and Space Administration's Earth Observing System (EOS) declared it as part of the minimum set of most important cloud observables (Wielicki et al., 1995). The global distribution of this parameter, however, is poorly known as demonstrated by the considerable scatter in published estimates of its mean value.

This dissertation was intended to be a step towards narrowing the range of uncertainty in this quantity and thus ultimately obtaining closure between satellite measurements and cloud microphysical theory. I attempted to put error bars on both satellite observations and theoretical estimates to seek whether the former could be increased and the latter could be decreased in order to obtain a consensus global estimate. At the early stages of the study the rationale was to focus on the optical retrieval technique with the help of the multiangle data set provided by the Multiangle Imaging

SpectroRadiometer (MISR). This explains the considerable attention devoted in this dissertation to the retrieval of cloud optical thickness. Although important limitations of the optical method were found it was later recognized that this multiangle approach did not hold the full answer to the posed question. This necessitated the widening of the study to include discussions on other measurement techniques, particularly comparisons with microwave observations.

This resulted in the following dissertation structure. Chapter 1 is the above introduction. Chapter 2 defines some key terms and gives a literature review of existing global estimates of cloud liquid water amount. Chapter 3 outlines the methodology, including an overview of the data sets used and the cloud optical thickness retrieval technique. Chapter 4 summarizes the results. This chapter includes a study on the consistency of angular cloud optical thicknesses that has already been published in Horváth and Davies (2004). It also contains a critical analysis of the cloud liquid water path estimates obtained from microphysical considerations by Pruppacher and Jaenicke (1995). It then draws some conclusions from case studies of comparisons between the microwave and optical techniques. Finally, it gives estimates of the global mean cloud liquid water path based on extrapolating optical retrievals. Chapter 5 summarizes and concludes the dissertation. Also included in the end of the dissertation are several appendices that contain certain algorithms and methods whose rather technical nature did not warrant their inclusion in the main body of the study.

CHAPTER 2 LITERATURE REVIEW

This chapter first defines some key terms including the main focus of this study: cloud liquid water path. Then follows a discussion of current methods used to measure this quantity. Finally, a review of historic estimates of global cloud liquid water path is given.

2.1 Definition of Key Terms

Consider a cloud with a drop size distribution that varies with the height above cloud base z . If the number concentration of cloud droplets at height z with radii between r and $r + dr$ is denoted as $n(r, z)dr$ then the liquid water content of the cloud is given by

$$w(z) = \frac{4}{3}\pi\rho_w \int_0^\infty n(r, z)r^3 dr, \quad (2.1)$$

where ρ_w is the density of water. The liquid water path is the integral of the liquid water content over the whole vertical extent of the cloud:

$$\begin{aligned} LWP &= \int_0^H w(z)dz \\ &= \frac{4}{3}\pi\rho_w \int_0^H \int_0^\infty n(r, z)r^3 dr dz, \end{aligned} \quad (2.2)$$

where H is the cloud thickness. Strictly speaking the liquid water content and liquid water path should include the mass of all hydrometeors. That is, the integral in (2.1) and (2.2) should be calculated over all drop sizes. In practice, however, the drop size distribution is most often separated into a small drop mode (cloud) and a large drop mode (rain), and w and LWP are computed for these two size ranges separately. Thus, one can distinguish between cloud liquid water path ($CLWP$), rain liquid water path ($RLWP$), and total liquid water path ($TLWP$), which is simply the sum of the cloud and rain components. The actual usage of the term “*liquid water path*” is somewhat ambiguous in the literature. Some authors use it to refer to the cloud component only, while others use it interchangeably with the total (cloud plus rain) liquid water path. The possibility of ambiguity is further increased when the phase of the hydrometeors (liquid or ice) is also considered. In the most general case one can distinguish between cloud and rain size hydrometeors, which can be either liquid or ice. When the mass of the ice phase constituents is also included the proper expression should simply be “*water path*” (i.e. leaving out the reference to liquid). Therefore, one can talk about cloud water path (CWP), rainwater path (RWP), and total water path (TWP), this latter now containing all cloud elements (small and large drops, liquid and ice).

In case of satellite measurements there is an additional complicating factor. Satellite retrievals (both optical and microwave) are classified as either clear or cloudy. This is achieved by putting a threshold on the retrieved/measured quantity. Pixels that are below the threshold are labeled as “clear”, the ones above the threshold are labeled as “cloudy”. When calculating mean quantities, for instance, one can include either the

cloudy pixels only, or all (clear plus cloudy) pixels in the averaging. Considering cloudy pixels only yields, strictly speaking, the cloud liquid water path. When clear pixels are also included in the average the resulting quantity could be termed “*atmospheric liquid water path*” (*ALWP*). Therefore, the global mean *CLWP* is normalized to the area covered by (liquid) clouds, while the global mean *ALWP* is normalized to the entire earth surface area. As a rule of thumb, the mean *CLWP* is about a factor of two larger than the mean *ALWP* because the fractional coverage of clouds containing some amount of liquid (i.e. excluding cirriform clouds) is about 50%. For climate studies *ALWP* is strongly preferred since this, unlike the *CLWP*, does not depend on the details (threshold) of the cloud classification algorithm. As pointed out by Lin and Rossow (1994), the large discrepancies between the various microwave retrievals published in the literature were partly due to differences in their definitions of a cloud.

Finally, this leads us to the issue of separating the cloud component of a drop size distribution from its rain component. Qualitatively speaking a raindrop is a water drop that reaches the surface and contributes to the annual mean rainfall of ~1 m. This straightforward definition becomes slightly ambiguous when expressed in terms of drop sizes. Cloud droplets are smaller and their size distribution is usually approximated by a lognormal or gamma distribution. Raindrops are larger and can be characterized by the Marshall and Palmer (1948) exponential distribution or by the lognormal distribution (Feingold and Levin, 1986; Sauvageot and Lacaux, 1995). The threshold radius separating small drops from large ones, however, varies from author to author. The values that most frequently occur in the literature are 25 μm , 50 μm , and 100 μm . The

American Meteorological Society (AMS) uses the following definitions: $r \leq 100 \text{ } \mu\text{m}$ for cloud drops, $100 < r \leq 250 \text{ } \mu\text{m}$ for drizzle drops, and $r > 250 \text{ } \mu\text{m}$ for raindrops (Glickman, 2000). The distinction between drizzle drops and raindrops is often overlooked and all drops with radii in excess of $100 \text{ } \mu\text{m}$ are called raindrops. The limiting radius of $100 \text{ } \mu\text{m}$ is rather arbitrary, but has been employed because drops of this size fall rapidly enough ($\sim 0.7 \text{ m/s}$) to survive evaporative dissipation for a distance of the order of several hundred meters. It is noted here that active cumulus clouds sometimes contain cloud drops much larger than the threshold size, especially in the presence of strong updrafts.

In summary, it is important to state clearly what is meant by the quantity “liquid water path”. This is underlined by the fact that the large discrepancies in the published values of this parameter are partly due to differences in its definition (whether rain, ice, or clear pixels are included or not). The subject of this dissertation was the liquid component only. Results obtained considering cloudy pixels only were referred to as “cloud liquid water path”. When clear pixels were also included in the calculations the term “atmospheric liquid water path” was used. Cloud drops were defined as having radii less than $100 \text{ } \mu\text{m}$. This definition was in part justified by the fact that most microwave retrieval techniques employ the Rayleigh approximation that is valid over this range only.

2.2 The Measurement of Cloud Liquid Water Path

2.2.1 Aircraft Observations

This technique is based on measuring the vertical in-cloud profile of the liquid water content. The liquid water path is then computed by integrating this profile. The most widely used instruments are hot-wire probes which measure liquid water content from the cooling effect of cloud drops impinging on a heated sensor element that is exposed to the airflow outside the aircraft. Popular versions of this instrument are the Johnson-Williams probe and the CSIRO-King probe (King et al., 1978). A third version, the Nevzorov probe, is described by Nevzorov (1980) and Korolev et al. (1998). These instruments have decreasing detection efficiencies for larger droplets: above a radius of $\sim 15 \mu\text{m}$ for the Johnson-Williams probe, and above a radius of $\sim 30 \mu\text{m}$ for the CSIRO-King and Nevzorov probes. This limitation is due to the increasing probabilities that larger droplets disintegrate on impact, and that some of their mass gets blown off the sensor prior to full evaporation.

An alternative method is to calculate the liquid water content from the measured drop size distribution. This is, however, an inherently imprecise approach because of the third power of size that enters the calculation. The standard tool for drop spectrum measurements is the light-scattering device developed by Particle Measuring Systems, Inc. (PMS), called the Forward Scattering Spectrometer Probe (FSSP) (Knollenberg, 1976, 1981). The main limitation of this instrument is that its detection range extends only to a droplet radius of $25 \mu\text{m}$ in the most widely used configuration. There is a newer

extended version of the instrument that measures drops up to a radius of 50 μm . This is, however, rarely used.

Consequently, one can conclude that in-situ microphysical measurements usually do not cover the full size range traditionally considered as cloud ($r \leq 100 \mu\text{m}$), but truncate the actual drop size distribution at a radius of 25-30 μm . This leaves a gap in the data between 30 μm and 100 μm , which might affect the reported cloud liquid water content and cloud drop effective radius values (i.e. they might be biased low). For example, Los and Duynkerke (2000) found that for drizzling marine Sc the effective droplet radius increased, on average, by 40% when the larger cloud droplets were included in the calculations. The increase in some cases was as large as a factor of 2-3. Gultepe et al. (2001) reported, also for low stratiform clouds, that truncating the drop size distribution can lead to an underestimation of 2-6 μm in the effective drop radius. The importance of this is that the cloud microphysics (effective radius, drop size distribution, liquid water content) assumed in radiative transfer calculations is usually based on in-situ measurements. Therefore, the effects of truncated observations can propagate to these calculations as well.

2.2.2 Rawinsonde Measurements

Radiosonde observations do not contain direct information about the cloud liquid water content. However, w can be parameterized based on the measured relative humidity and temperature profiles (see e.g. Karstens et al., 1994). Cloud layers can be identified as having relative humidity exceeding a certain threshold, say 95%. The adiabatic liquid

water content at altitude z above cloud base can then be defined as the difference between the saturation water vapor mixing ratio at cloud base and its value at level z . The adiabatic value represents the upper limit of cloud liquid water content. Aircraft observations indicate, for instance, that the ratio of observed to adiabatic liquid water content decreases with height above cloud base (Warner, 1955). A parameterization can be devised that reflects this behavior and thus simulates the effects of mixing with entrained drier air, freezing of drops, and precipitation, all of which can significantly reduce the liquid water content. The main limitation of this method is that it is rather empirical. In addition, rawinsonde measurements are unreliable below a temperature of about -40°C and they are also likely to undersample the most vigorous convective cloud types.

2.2.3 Optical Technique

This technique calculates the cloud liquid water path from the retrieved visible optical thickness and the retrieved/assumed drop effective radius. Cloud optical thickness, τ , is defined as the integral of the volume extinction coefficient, β_e , over the whole cloud depth, H , i.e.

$$\tau(\lambda) = \int_0^H \beta_e(\lambda, z) dz, \quad (2.3)$$

where λ is the wavelength. For a given drop size distribution $n(r, z)$ the volume extinction coefficient is defined as

$$\beta_e(\lambda, z) = \pi \int_0^\infty Q_e(x, z) r^2 n(r, z) dr, \quad (2.4)$$

where $x = 2\pi r / \lambda$ is the size parameter, and Q_e is the extinction efficiency given by Mie theory. The value of Q_e oscillates with decreasing amplitude as the size parameter increases, and asymptotes to the value of 2 in the large-drop limit. In the visible wavelength region it is usually assumed that $Q_e \approx 2$. This approximation introduces an error less than 5%. Finally, assuming a vertically homogeneous cloud and invoking the definition of the effective radius, which is the ratio of the third to the second moment of the drop size distribution

$$r_e = \frac{\int_0^\infty n(r) r^3 dr}{\int_0^\infty n(r) r^2 dr}, \quad (2.5)$$

the cloud liquid water path in (2.2) can be expressed with the help of (2.3), (2.4), and (2.5) as

$$LWP \approx \frac{2}{3} \rho_w \tau r_e. \quad (2.6)$$

If the value of $\rho_w = 1 \text{ g/cm}^3$ is used and r_e is given in micron then (2.6) gives the liquid water path in g/m^2 . Even though this formula is widely used, it is only as good as its input parameters. Cloud optical thickness is most often retrieved using plane-parallel theory, which assumes a horizontally infinite and uniform cloud, and thus neglects the three-dimensional effects occurring in real clouds. The errors introduced by this 1D approach have been well documented in the literature (e.g. Loeb and Davies, 1996). Even with the proper (3D) treatment of cloud-radiation interactions the fact remains that cloud visible reflectance saturates with optical thickness. This results in a value of $\tau \approx 100$ as the practical upper limit of the optical depth retrievals.

The retrieval of the drop effective radius can be problematic too. In the absence of absorption channel measurements, a predetermined constant value of r_e has to be used for all clouds. It is common to assume a fixed value of $r_e = 10 \text{ }\mu\text{m}$. It seems reasonable to assume that the effective radius has a tendency to increase with increasing optical thickness (i.e. increasing probability of rain). Even though the actual shape of the drop size distribution in active, precipitating clouds is poorly observed in-situ, both dynamical cloud models (e.g. Mugnai and Smith, 1988) and statistical drop-growth models (e.g. Berry and Reinhardt, 1974) indicate that these wettest and optically thickest clouds tend to have broad, often bimodal size distributions, for which a value of $r_e = 10 \text{ }\mu\text{m}$ is likely to be an underestimate. Therefore, the errors introduced by using a fixed drop effective radius that is characteristic of relatively thin marine Sc clouds do not cancel, and can result in a global mean liquid water path that is biased low. When absorption channel data

are available the effective radius can be retrieved. These satellite-retrieved effective radii, however, are only representative of the upper portions of the cloud that are within an optical depth of 2-3 from cloud top (Platnick and Valero, 1995). This topmost cloud layer contains large amounts of ice in the thickest cumulus towers. Therefore, these clouds, as seen by satellites, are likely to be classified as ice clouds and the retrieved effective radius is representative of ice crystals rather than liquid drops. Hence, one can conclude that it is difficult to measure the effective radius of the liquid water portion of the thickest clouds, even with the absorption technique. Consequently, the ability of the optical technique to determine the liquid water path of the wettest clouds seems seriously limited.

2.2.4 Microwave Technique

It is not my intention to give a comprehensive review of the huge literature concerning this technique. Only the most important aspects of this method that are relevant to my study are discussed. A nice review of the early period from 1968 to 1980, including the pioneering Russian efforts, can be found in Lovejoy and Austin (1980). The extensive Russian research in this field was also covered by a two-volume book (Burtsev et al., 1971; Vinnichenko and Gorelik, 1971), and by Matveev (1984). A review of estimating climate-scale rainfall from satellites up to 1989 can be found in Arkin and Ardanuy (1989). Early methods used data from radiometers on the Cosmos-243, Cosmos-384, and Meteor-18 satellites and from the Electrically Scanning Microwave Radiometer (ESMR) on board Nimbus-5, and the Scanning Multichannel Microwave Radiometer

(SMMR) on board SeaSat and Nimbus 7. The most recent methods were developed for the Special Sensor Microwave/Imager (SSM/I) and for the TRMM Microwave Imager (TMI) instruments. The SSM/I's fly on board the Defense Meteorological Satellite Program (DMSP) satellites, while the TMI is on the Tropical Rainfall Measuring Mission (TRMM). This dissertation used SSM/I and TMI data since these represent the most comprehensive and most widely used datasets.

The retrievals using microwave brightness temperature measurements were devised mainly to obtain precipitation rate. In addition to rain rate, these algorithms usually also yield other geophysical parameters, such as columnar water vapor, columnar cloud liquid water, and near-surface wind speed. Some early algorithms connecting geophysical parameters to brightness temperatures were statistically based (e.g. Alishouse et al., 1990; Petty, 1990; Goodberlet et al., 1989). The most successful methods, however, are physically based and model the transfer of microwave radiation through a cloudy atmosphere. Simpler algorithms include only cloud emission and absorption (e.g., Greenwald et al., 1993). These emission-based models are adequate for clouds containing mainly small liquid and ice drops. Absorption by ice is usually negligible and small drops do not scatter significantly. More sophisticated algorithms also include the scattering produced by large precipitation-sized cloud and rain elements, both liquid and ice (e.g., Smith et al., 1992; Liu and Curry, 1992). These scattering-based methods have been used to estimate heavy rain rates. The relative importance of emission/scattering also depends on the employed frequency, with higher frequencies usually requiring the modeling of scattering.

One of the major limitations of microwave techniques is that most of them are applicable over ocean only. Over land the highly variable emissivity of the warm surface poses serious difficulties. Another problem is the so-called beam filling effect, which arises when the relatively large (on the order of tens of kilometers) microwave footprints are filled by horizontally inhomogeneous clouds or when they are only partially filled by clouds (broken cloudiness). The beam filling effect leads to underestimates of the cloud liquid water path. This problem can be remedied by applying empirical correction factors or by using ancillary visible imagery that can provide cloud fraction information. From the point of view of this dissertation, however, the most serious problem is the inadequate separation of cloud- and rainwater. This fundamental limitation of the microwave technique means that it is impossible, even with multifrequency observations, to uniquely separate and retrieve rain rate and cloud liquid water content. One must make a priori assumptions regarding the relative proportion of these two quantities. Early models did not attempt to separate these two components, hence retrieved total liquid water path, or only included a rather primitive treatment of the non-raining cloud. Wilheit et al. (1977), for instance, assumed a fixed cloud component with a liquid water path of 250 g/m^2 and a geometrical thickness of 0.5 km. This popular model was also invoked by many later methods (e.g. Lin and Rossow, 1994, 1997). Current state-of-the-art algorithms either employ a predefined set of rain cloud models, or parameterize the cloud component based on the rain rate. Kummerow and Giglio (1994), for example, use a set of 27 cloud structures, 18 of which are defined as convective, and 9 as stratiform precipitation. Their algorithm then identifies potential structures among this limited set. Wentz and Spencer

(1998), on the other hand, parameterized the cloud liquid water path as a function of rain rate. This parameterization is based on the assumptions that *CLWP* generally increases with rain rate, and that it tends to level off at very high rain rates. Their formula allows a maximum *CLWP* between 1000 g/m^2 and 2000 g/m^2 , depending on the height of the rain column. This essentially means that *CLWP* is not really retrieved, but rain rate is. Despite these efforts, our very limited knowledge of the drop size distribution in precipitating clouds continues to hamper the retrieval of *CLWP* in these clouds. Some hope in this area is offered by a new technique (Czekala et al., 2001), which uses the polarization signal produced by precipitation particles to independently estimate the cloud and rain liquid water fractions. This dual polarization method, however, has only been used for ground-based radiometry and has not found its way yet to satellite retrievals.

2.3 Global Cloud Liquid Water Estimates

In this section I review the history of global cloud liquid water measurements. Table 2.1 and Figure 2.1 summarize the published estimates. Each entry in the table is discussed below.

Junge (1963)

Junge (1963) used data from De Bary and Möller (1960) on the vertical distribution of cloud frequencies, based on 4 years of aircraft observations in Central Europe. From the annual average frequency of all types of clouds as a function of altitude they estimated that in these latitudes, on average, around 32% of the volume of the lower

Table 2.1 History of global liquid water path estimates.

Author	Mean <i>ALWP</i> (g/m ²)	Mean <i>CLWP</i> (g/m ²)
Junge (1963)	900 ^a	1800 ^a
Akvilonova et al. (1973)	249	-
Pruppacher and Klett (1978)	750	1500
Njoku and Swanson (1983)	70	-
Prabhakara et al. (1983)	55	183
Matveev (1984)	264	-
Greenwald et al. (1993)	69	80
Karstens et al. (1994)	63	126
Greenwald et al. (1995)	61 ^{b/-}	113 ^b /95 ^c
Pruppacher and Jaenicke (1995)	382 ^d	750
Rossow and Schiffer (1999)	22 ^h	65 ^e /24 ^f /92 ^g
SSM/I data for 1987-2003	62	128
Weng and Grody (1994) algorithm		
SSM/I data from REMSS	84	94
Wentz and Spencer (1998) algorithm		

^aEurope only^ball clouds, ^clow clouds only (CTP > 680 mb)^ddue to rounding errors the authors quoted a value of 388 g/m²^egiven in paper, ^fmaximum from $WP = 6.292\tau$, ^gland only for 1990 (from Wang et al., 2000)^haverage of e and f with assuming a 50% liquid cloud cover

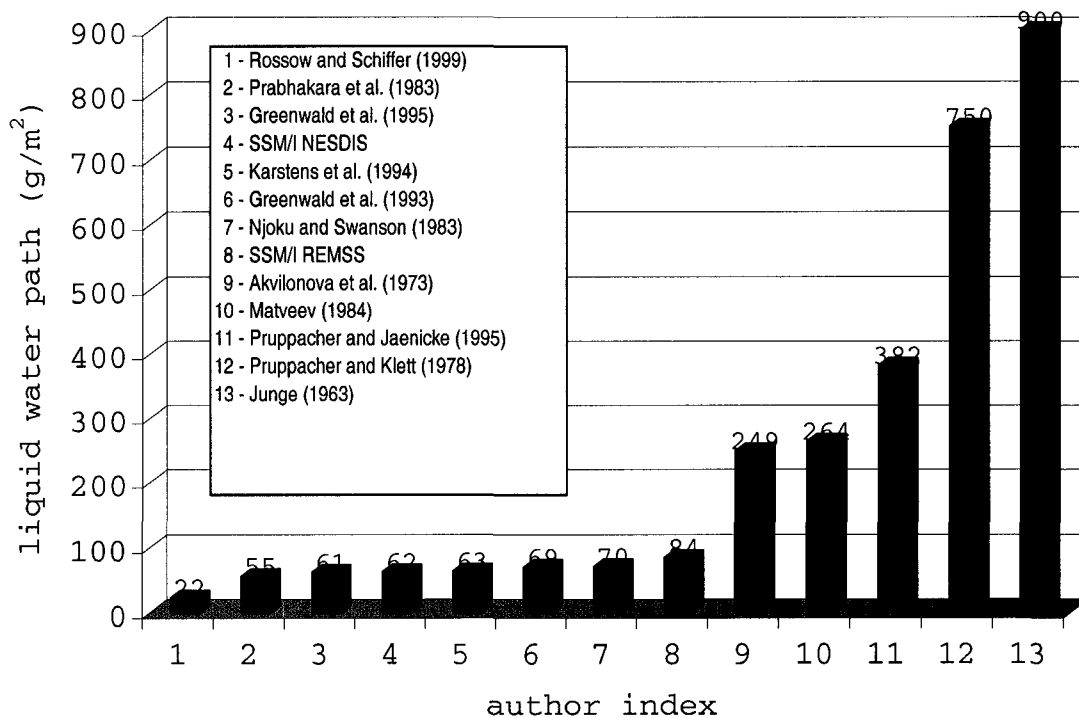


Figure 2.1 Estimates of global mean atmospheric liquid water path (column 2 from Table 2.1). Blue bars correspond to satellite and radiosonde measurements, red bars refer to theoretical estimates.

troposphere between 0 km and 5.5 km is filled with clouds. Junge (1963) assumed an average liquid water content of 0.5 g/m^3 in clouds, which resulted in a mean columnar atmospheric liquid water amount of

$$\begin{aligned}\overline{ALWP} &= 5500 \text{ m} \times 0.32 \times 0.5 \text{ g/m}^3 \\ &= 880 \text{ g/m}^2 \approx 900 \text{ g/m}^2\end{aligned}$$

Assuming an area cloud cover of 50% for liquid clouds this leads to a mean *CLWP* of 1800 g/m^2 .

Akvilonova et al. (1973)

From microwave measurements obtained by the Cosmos-384 satellite Akvilonova et al. (1973) found that the total global cloud liquid water mass in the marine environment averaged over 5 days from September 23 to 27, 1968 was about 8.7×10^{13} kg. Considering that the surface area of Earth's oceans is $A_o = 0.7 \times 5 \times 10^{14} \text{ m}^2$ this corresponds to a global mean atmospheric liquid water path of 249 g/m^2 over the oceans. It is noted here that no attempt was made to separate rain from clouds, therefore the reported *LWP* values are most likely to include rainwater as well.

Pruppacher and Klett (1978)

Pruppacher and Klett (1978) arrived at a global liquid water path estimate by assuming characteristic values for cloud parameters. They assumed that on global

average the cloud thickness is ~3 km, the cloud fraction is ~50%, and the cloud liquid water content is ~0.5 g/m³. This leads to a global mean atmospheric liquid water path of

$$\begin{aligned}\overline{ALWP} &= 3000 \text{ m} \times 0.5 \text{ g/m}^3 \times 0.5 \\ &= 750 \text{ g/m}^2\end{aligned}$$

Because the assumed global cloud fraction is 50% this also means that the global mean cloud liquid water path is twice as much that is 1500 g/m². It is noted that the global *LWP* values here are most likely overestimates due to the unrealistic assumption on cloud thickness. Considering the frequent occurrence of thin boundary layer clouds (e.g., marine Sc) a global mean cloud thickness of 3 km seems unreasonably large. Radiosonde data sets indicate a value about half of that (Poore et al., 1995; Wang et al., 2000).

Njoku and Swanson (1983)

Njoku and Swanson (1983) presented liquid water retrievals over the oceans derived from microwave data obtained by the SMMR on the Seasat satellite. In their study no cloud filtering was performed therefore the retrieved quantity was atmospheric liquid water rather than cloud liquid water. Their global mean atmospheric liquid water path, estimated from both daytime and nighttime data, was 70 g/m² for the entire Seasat mission (11 July-10 October 1978).

Prabhakara et al. (1983)

Prabhakara et al. (1983) reported the zonal distribution of liquid water between 50°S and 50°N calculated from Nimbus 7 SMMR data for August 1979. The data included both the cloud and the rain components. The global mean atmospheric *LWP* was found to be 55 g/m². They estimated that around 30% of all observations contained clouds. This translates to a global mean cloud *LWP* of 183 g/m².

Matveev (1984)

Matveev (1984) reported microwave data obtained with the Cosmos-243 satellite over the oceans and averaged over the observation period 23-27 September 1968. His Figure 4.12 (p. 133) shows the average meridional profile of cloud water reserves between 60°N and 60°S. Because the actual data values were not available Figure 4.12 was scanned and the liquid water path as a function of latitude was determined from the digitized plot. The meridional values weighted by the area of the oceans resulted in a global mean liquid water path of 264 g/m². This is very close to the value given by Akvilonova et al. (1973). Matveev (1984) and Akvilonova et al. (1973) obviously reported data covering the same observation period but obtained with two different satellites. As before in Akvilonova et al. (1973) the retrieved *LWP* included the contribution from rain as well.

Greenwald et al. (1993)

Greenwald et al. (1993) developed a method to derive integrated liquid water over the oceans using microwave brightness temperatures obtained from the SSM/I on board the DMSP F-8 satellite. Cloudy areas were determined with the help of Geostationary Operational Environmental Satellite (GOES) imagery. For areas labeled as “clear” by the GOES cloud mask they reported very small retrieved liquid water paths with a standard deviation of 16 g/m^2 . The lowest retrieved value of liquid water was around 40 g/m^2 for these pixels. This means that the GOES cloud mask applied in their study was practically equivalent to using a (cloud) threshold on the liquid water path somewhere between 16 g/m^2 and 40 g/m^2 . The identification of rainfall was also achieved by simple thresholding. Pixels with a liquid water path above 500 g/m^2 were flagged as potentially contaminated by precipitation. For the purpose of minimizing biases in the monthly mean liquid water, which would probably occur if cloud water was neglected in precipitating systems, the liquid water path was set to the (rain) threshold value of 500 g/m^2 for pixels identified as being rain contaminated.

For the global oceans as a whole the average cloud liquid water was determined to be about 80 g/m^2 . The global mean was found to be greater for the northern hemisphere summer than for the winter with respective values of 81 g/m^2 and 75 g/m^2 for August 1987 and February 1988. The total global cloud liquid water mass over the oceans was determined to be about $2.4 \times 10^{13} \text{ kg}$. Dividing this value by the surface area of Earth's oceans, A_o , yields 69 g/m^2 for the global mean atmospheric liquid water path over the oceans. Comparing the global mean atmospheric and cloud liquid water paths also yields

an oceanic cloud fraction, i.e. percentage of retrievals exceeding the cloud threshold, of approximately 86%, if it is assumed that clear pixels contain no liquid water. If clear pixels were included in the averaging with a liquid water path of 16 g/m^2 , or 40 g/m^2 then the respective oceanic cloud fractions would be 83%, or 73%.

Karstens et al. (1994)

Karstens et al. (1994) presented a method to infer cloud liquid water path over the ocean from microwave measurements of SSM/I on board the DMSP F-8 satellite. They derived maps of monthly mean liquid water path over the Atlantic Ocean for the Octobers of 1987-1991. The global mean *LWP*, however, was not calculated from the actual SSM/I monthly maps. Instead, they gave a mean *LWP* value derived from radiosonde observations. Radiosonde observations were used to calculate cloud *LWP* and as input data for a microwave radiative transfer model used to simulate brightness temperatures for the spectral intervals of SSM/I. The actual satellite-based *LWP* retrieval algorithm was then derived by applying multiple linear regression between the simulated brightness temperatures and the radiosonde-determined *LWP*. More than 3000 radiosonde ascents launched from ships were available for the study. Although the measurements covered the Atlantic Ocean only, the authors claimed that their results were globally representative. Since radiosonde observations do not contain direct information about cloud water this quantity was parameterized based on the relative humidity and temperature profiles. The vertical distribution of cloud liquid water content was calculated from a modified adiabatic profile, which attempted to include the effects of

entrainment, precipitation, and freezing; these usually reduce the water content. The authors also used a threshold on *LWP* to filter out rainwater. Based on investigations by Oelke (1992) and their own direct observations during ICE'89 (International Cirrus Experiment 1989) they concluded that clouds start raining if the *LWP* exceeds 500 g/m^2 . Thus they assumed that 500 g/m^2 is the maximum cloud water path a cloud can contain. If the calculated *LPW* exceeded this threshold it was set to 500 g/m^2 . The maximum retrieved *LWP* was 2500 g/m^2 .

With the above caveats they found that the global mean *CLWP* for non-precipitating clouds was 126 g/m^2 with a standard deviation of 130 g/m^2 . Assuming a global liquid cloud fraction of 50% this yields an *ALWP* of 63 g/m^2 . Based on the satellite-derived maps they found a large interannual variability of monthly mean *LWP*. They also compared their results to the modeled cloud water content of the climate model ECHAM-T42 (Roeckner et al., 1989) of the Max-Planck-Institut für Meteorologie in Hamburg. Large differences were found between the measured and modeled *LWP*, which were attributed to the fact that the model's cloud scheme (Roeckner et al., 1991) was tuned to produce the proper shortwave and longwave fluxes measured by ERBE rather than the proper hydrology.

Greenwald et al. (1995)

Greenwald et al. (1995) presented monthly mean marine cloud liquid water statistics on a $2.5^\circ \times 2.5^\circ$ grid over a 53-month period beginning July 1987 and ending in December 1991. This study used the same instrument, SSM/I on the DMSP F-8 satellite,

and essentially the same retrieval method (although slightly modified) as the Greenwald et al. (1993) study. Compared to the earlier study the main differences seem to be that the data spanned a longer period (4.5 years), the retrieval algorithm underwent some unspecified modifications, and that the thresholds used to discriminate between clear and cloudy pixels and precipitating and non-precipitating clouds were slightly different in this later study. The clear-cloudy threshold was set to 48 g/m^2 (as opposed to somewhere between 16 g/m^2 and 40 g/m^2). This threshold was selected for two reasons. First, the $0\text{--}48 \text{ g/m}^2$ range covered nearly the entire spread of the clear sky retrievals. Second, monthly mean cloudiness derived from the *LWP* data using this threshold were reasonably consistent with cloud amounts measured by the International Satellite Cloud Climatology Project (ISCCP). The precipitation threshold was reduced from 500 g/m^2 to 400 g/m^2 . A further subtle difference between the two studies was that in Greenwald et al. (1993) “raining” pixels were included in the averaging with a cloud liquid water path of 500 g/m^2 (i.e. the precipitation threshold), while in Greenwald et al. (1995) “precipitating” pixels exceeding the 400 g/m^2 threshold were excluded from the analysis.

The global average cloud *LWP* was determined to be 113 g/m^2 . The seasonal variation of the global mean value showed a minimum of 111 g/m^2 in April and a maximum of 116 g/m^2 in December. The Northern Hemisphere exhibited greater seasonal change, with a low hemispheric mean of 107 g/m^2 in March and a peak value of 118 g/m^2 in August. In the Southern Hemisphere the seasonal variability was slightly less, the lowest cloud *LWP* values were spread out over a 4-5 month period (May-September) and gradually increased to a maximum of 117 g/m^2 in January. The seasonal

departures of monthly mean cloud *LWP*, when averaged over $2.5^\circ \times 2.5^\circ$ regions, were typically between 15% and 25% of the annual mean and were largest in the Tropics and northern midlatitudes. The zonally averaged structure of cloud *LWP* was found to be distinctly trimodal. The maxima in the midlatitudes (40°N/S) were probably due to baroclinic storm activity. The peak near the equator (5°N) was caused mainly by the Intertropical Convergence Zone (ITCZ). It is also interesting to note that the retrievals indicated an overall decline in the cloud *LWP* towards the highest latitudes (poleward of about 55°). This is in contrast with 1D optical thickness retrievals that usually increase with latitude. This discrepancy may be explained by systematic optical thickness retrieval errors due to 3D effects, a decrease in drop effective radius towards the poles, or by the fact that microwave measurements are not sensitive to the ice component while the optical retrievals are.

When clear pixels were also included in the averaging the resulting *LWP* values were often nearly a factor of 2 smaller than those for the cloud only dataset. The global mean atmospheric (i.e. cloud plus clear) *LWP* was 61 g/m^2 . If it is assumed that clear pixels, by definition, contain 0 g/m^2 liquid water then contrasting the cloud and atmospheric *LWP* values reveals a cloud fraction of about 54%. That is 54% of *LWP* retrievals exceeded 48 g/m^2 . Greenwald et al. (1995) also calculated the global mean *LWP* separately for clouds that were categorized by the ISCCP as low clouds that is cumulus, stratocumulus, and stratus. Low clouds were defined as clouds with cloud-top pressures between 680 and 1000 mb and were identified with the help of ISCCP measurements. The global average *LWP* for low clouds was found to be 95 g/m^2 .

Recalling that they obtained a mean value of 113 g/m^2 for all clouds, one can conclude that low clouds dominated their dataset.

Pruppacher and Jaenicke (1995)

Pruppacher and Jaenicke (1995) improved upon their previous estimate given in Pruppacher and Klett (1978) by breaking down the calculation to individual cloud types. Rather than using global all-cloud estimates for cloud fraction, cloud thickness, and cloud liquid water content, they presented characteristic values of these parameters separately for 5 different cloud groups. The mean cloud liquid water path was computed for each cloud group, and then the global mean was determined by adding up the 5 individual estimates. This particular study will be analyzed in greater detail in section 4.1, so here only the final results are presented. The global mean atmospheric liquid water path was estimated to be 382 g/m^2 – the authors actually quoted a slightly erroneous value of 388 g/m^2 that could be traced back to rounding errors. The total cloud cover computed from the individual cloud-type amounts assuming random overlap was 51%. Therefore, the global mean cloud liquid water path was determined to be $\sim 750 \text{ g/m}^2$.

Rossow and Schiffer (1999)

Rossow and Schiffer (1999) reported global, annual mean cloud properties from the ISCCP D2 dataset for the period from July 1983 through December 1997. They estimated that the global mean cloud water path was 61 g/m^2 over ocean and 74 g/m^2 over land. Considering that the ratio of the surface area of the ocean to that of land is

70:30 this gave a global mean cloud water path of $0.7 \times 61 + 0.3 \times 74 \approx 65 \text{ g/m}^2$ for the entire planet. They also determined the cloud water path separately for certain cloud types. The following global (ocean plus land) results were found: 23 g/m^2 for cirrus and cirrostratus, 261 g/m^2 for deep convective clouds, 60 g/m^2 for middle-level clouds (that is ISCCP cloud types altocumulus, altostratus, and nimbostratus), and finally 51 g/m^2 for low-level clouds (that is ISCCP cloud types cumulus, stratocumulus, and stratus).

It is interesting to reflect here on the way ISCCP calculates cloud water path. For each cloudy pixel the optical thickness τ is determined from the observed radiances at visible wavelengths ($\approx 0.6 \text{ }\mu\text{m}$). This optical thickness is then converted into liquid water path (*LWP*) or ice water path (*IWP*) using an empirical formula whose actual form depends on the assumed drop size distribution. For liquid water clouds ISCCP assumes a gamma drop size distribution with an effective radius of $10 \text{ }\mu\text{m}$ and an effective variance of 0.15 (Hansen and Travis, 1974). This approximately yields $LWP = 6.292\tau$, where *LWP* is given in g/m^2 . Ice clouds are assumed to be composed of fractal polycrystals (Macke et al., 1996) with a -2 power-law size distribution between $20 \text{ }\mu\text{m}$ and $50 \text{ }\mu\text{m}$, giving an effective radius of $30 \text{ }\mu\text{m}$, and an effective variance of 0.1 (see Mishchenko et al., 1996). For this drop size distribution Rossow and Schiffer (1999) gives the following formula: $IWP = 10.5\tau$. Ice and liquid clouds are separated based on the cloud top temperature T_c . If $T_c < 260 \text{ K}$ the entire cloud column is assumed to be composed of ice even though there might be liquid water or mixed layers below the topmost ice layer. This most likely results in an overestimation of the global *IWP* and an underestimation of the global *LWP*.

Comparison of the above *LWP* and *IWP* formulas show that for the same optical thickness ice clouds contain more (equivalent) water than do liquid clouds. What is actually given in Rossow and Schiffer (1999) is not the cloud liquid water path but the total cloud water path, which is the sum of the liquid and ice water paths, that is $TWP = LWP + IWP$. The given *TWP* values, however, seem to be inconsistent with the given cloud optical thicknesses, if indeed the above *LWP* and *IWP* formulas were used to convert between the two. The authors determined the following cloud optical thickness values: 3.8 for the global mean, 2.2 for cirrus and cirrostratus, 35.6 for deep convective clouds, 4.8 for middle-level clouds, and finally 4.7 for low-level clouds. The cirrus/cirrostratus category, by definition, only contains ice clouds. For this group the quoted mean *IWP* and mean τ are consistent: $IWP = 10.5 \times 2.2 = 23.1 \text{ g/m}^2$. All the other categories can contain both liquid and ice clouds, thus the mean optical thickness is a weighted sum of the liquid and ice portions: $\tau = f_i \tau_i + (1 - f_i) \tau_L$. Here f_i is the fraction of ice clouds in the dataset and τ_i , and τ_L are the mean ice and liquid cloud optical thicknesses, respectively. An upper limit on the *TWP* can be obtained if it is assumed that all the clouds are ice (i.e. $f_i = 1$), because ice clouds contain more (equivalent) water than do liquid clouds for the same optical thickness. This way one gets the following results. For the global mean, $TWP_{\max} = 10.5 \times 3.8 \approx 40 \text{ g/m}^2$, which is less than the quoted value of 65 g/m^2 . In turn, if it is assumed that the global mean cloud optical thickness is due solely to liquid water clouds, one gets $CLWP = 6.292 \times 3.8 \approx 24 \text{ g/m}^2$ as an upper limit on the global cloud liquid water content according to ISCCP data. For middle-level

clouds, $TWP_{\max} = 10.5 \times 4.8 \approx 50 \text{ g/m}^2$, which is again less than the quoted value of 60 g/m^2 . For low-level clouds, $TWP_{\max} = 10.5 \times 4.7 \approx 49 \text{ g/m}^2$, which is at odds with the quoted value of 51 g/m^2 if it is considered that most of these clouds are likely to be liquid water, hence the water path should be closer to $TWP = 6.292 \times 4.7 \approx 30 \text{ g/m}^2$. For deep convective clouds the quoted TWP and τ values are consistent if it is assumed that $\sim 75\%$ of the mean optical thickness is due to liquid water and $\sim 25\%$ is due to ice, since then $TWP = 35.6 \times (6.292 \times 0.75 + 10.5 \times 0.25) \approx 261 \text{ g/m}^2$. In summary, with the exception of the cirrus/cirrostratus and deep convective cloud categories the presented TWP and τ values, and the empirical formulas connecting these two parameters were inconsistent.

Finally, Wang et al. (2000) also gives a global mean LWP estimate citing ISCCP data. They calculated the annual mean LWP over land from 1 year (1990) of ISCCP D2 data collocated to rawinsonde stations. Their value of 92 g/m^2 is about 40% larger than the long-term (ocean plus land) average reported in Rossow and Schiffer (1999). This discrepancy may indicate a land-ocean contrast and/or potentially large interannual variations.

SSM/I data from NESDIS

A 16-year dataset of the entire SSM/I archive was compiled by the Hydrology Team of the NOAA/NESDIS/Office of Research and Applications/Atmospheric Research and Applications Division. The data used in this study covered the period from July 1987 to July 2003. The DMSP F-8 satellite was used from July 1987 through December 1991. The DMSP F-11 satellite was used from January 1992 through April 1995. The DMSP F-

13 satellite was used from May 1995 to the present. Due to DMSP F-8 instrument failures there were no valid data for December 1987, and from July 1990 through December 1991. The intersensor calibration of the DMSP SSM/I's is described in Colton and Poe (1999). An overview of the available products can be found in Ferraro et al. (1996). Here the monthly mean marine cloud liquid water product was used. The data were given on a $1^\circ \times 1^\circ$ grid and were downloaded from the National Climatic Data Center's (NCDC) web site (<http://lwf.ncdc.noaa.gov/oa/satellite/ssmi/ssmipproducts.html>). The algorithm to retrieve liquid water is described by Weng and Grody (1994). This technique cannot separate liquid water in the form of raindrops from cloud droplets, so that the *LWP* product includes both forms of liquid water. The clear-cloudy threshold was set to 20 g/m^2 . The 16-year global average cloud liquid water path over the oceans was determined to be 128 g/m^2 . The individual annual mean values showed only a slight (2-3%) variation about the long-term 16-year average. The frequency of clouds, or cloudiness fraction (*CFR*), which is the percentage of the time when the *LWP* exceeds 20 g/m^2 , was also included in this dataset. The product of *LWP* and *CFR* (~48%) yielded the mean *LWP* under both clear and cloudy conditions. This atmospheric liquid water path was found to be 62 g/m^2 .

SSM/I data from REMSS

The entire SSM/I archive (1987-2004) was also available from Remote Sensing Systems (REMSS; <http://www.remss.com>). This SSM/I Pathfinder dataset was produced with the Wentz algorithm (Wentz, 1997; Wentz and Spencer, 1998). Global averages

were calculated from monthly mean *LWP* data that were available on a 0.25-degree grid. There was no explicit cloud screening in this dataset. The global mean atmospheric *LWP* was determined to be 84 g/m². When using the same clear-cloudy threshold as in Greenwald et al. (1995), i.e. 48 g/m², the global mean cloud *LWP* was found to be 94 g/m². Note the relatively small increase from *ALWP* to *CLWP*.

CHAPTER 3 METHODOLOGY

This chapter covers the details of retrieving cloud optical thickness from visible MISR reflectances. First, the multiangle dataset is described. Then, the traditional lookup-table retrieval algorithm is discussed. Finally, a summary of the atmospheric corrections applied to the raw reflectances follows. This includes corrections due to ozone-, and water vapor absorption and Rayleigh scattering.

3.1 Instrument and Dataset Overview

3.1.1 The Multiangle Imaging SpectroRadiometer

The Multiangle Imaging SpectroRadiometer (MISR) was launched on 18 December 1999 aboard Terra, the first of the Earth Observing System (EOS) spacecraft (Diner et al., 2002). The instrument measures reflected sunlight with nine pushbroom sensors oriented at different angles along-track (see Figure 3.1). One camera (designated An) points toward the nadir, one bank of four cameras (designated Af, Bf, Cf, and Df) points in the forward direction, and the other bank of four cameras (designated Aa, Ba, Ca, and Da) points in the aft (backward) direction, with respect to the direction of flight. The nominal view zenith angles, relative to the earth's surface, are 0° , 26.1° , 45.6° , 60° , and 70.5° for An, Af/Aa, Bf/Ba, Cf/Ca, and Df/Da, respectively. In order to compensate for earth's rotation, the oblique MISR cameras also feature small nominal cross-track offsets of 1° , 1.7° , 2.3° , and 2.7° for the Af/Aa, Bf/Ba, Cf/Ca, and Df/Da cameras, respectively (Diner et al., 1998). Due to this cross-track offset oblique forward cameras

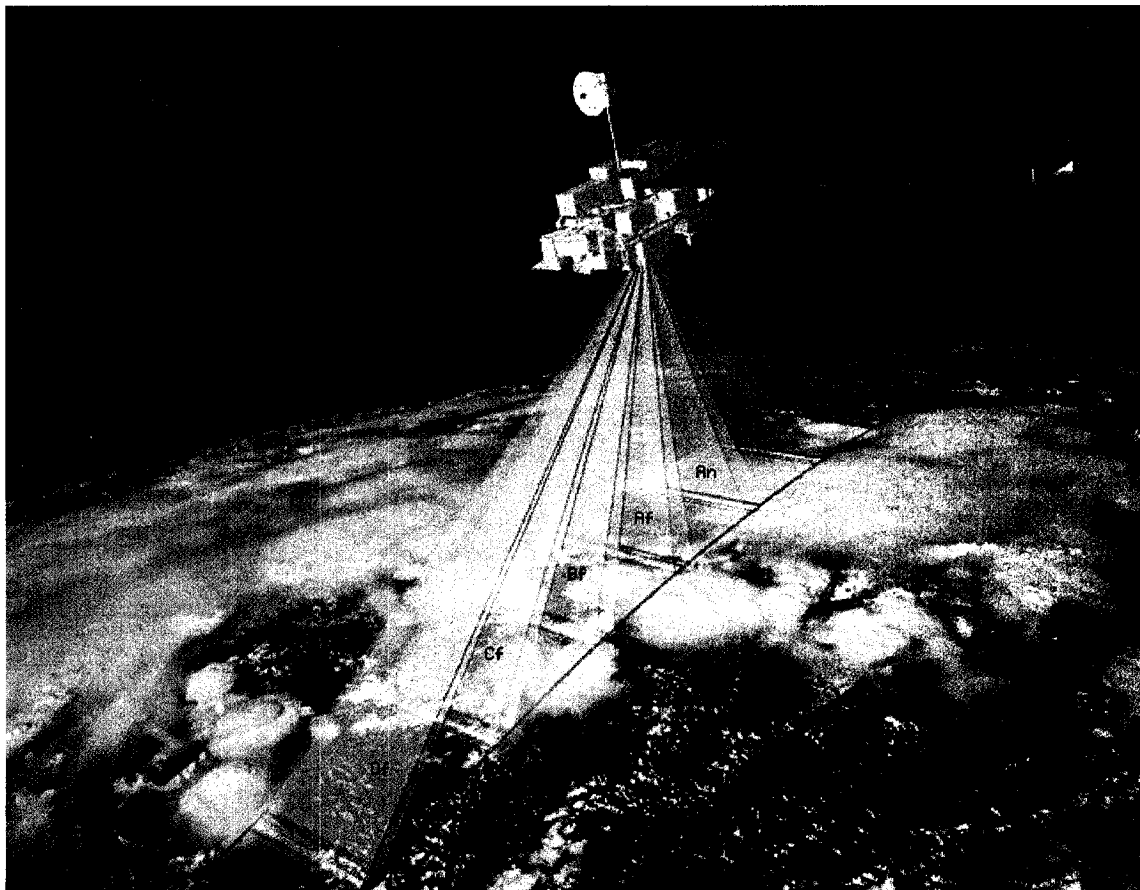


Figure 3.1 The MISR instrument on the Terra satellite. Direction of flight is toward the lower left. The translucent surfaces illustrate the actual locations imaged by the nine cameras along the earth's surface. Image courtesy of Shigeru Suzuki and Eric M. De Jong, Solar System Visualization Project; JPL image P-49081.

point slightly west while oblique aft cameras point slightly east. Each of the nine cameras measures radiances in four, approximately Gaussian, spectral bands centered at 446 nm (blue), 558 nm (green), 672 nm (red), and 866 nm (near-infrared).

The Terra satellite flies at an altitude of 705 km in a near-polar, sun-synchronous descending orbit with a 10:45 am equator crossing time. The inclination of the orbit is 98° , which allows observations up to 82° latitude. The swath width is 376 km in the nadir and 413 km off-nadir. The width of the zonal overlap swath (that is, the swath seen in common by all nine cameras along a line of constant latitude) is 360 km, which yields multiangle coverage of an entire latitude circle in nine days at the equator, and two days near the poles. The spacecraft covers 233 unique orbits in a 16-day repeat cycle.

Out of the four available spectral channels, only the red band (672 nm) was used in this study since this offered the highest resolution. The ground-projected instantaneous field of view (GIFOV) is 275 m in the cross-track direction, while the along-track GIFOV increases with view angle from 214 m at nadir to 707 m at the most oblique angle (D_f/D_a). The sample spacing, in both the cross-track and along-track directions, is 275 m for all cameras. Since the time interval between the two most oblique observations is 7 min, the instrument allows almost instantaneous sampling of the bi-directional reflectance field of clouds and the surface (see Figure 3.2). The sampling, however, is limited to the nine fixed angles in a single azimuthal plane determined by the flight direction with respect to the sun. The situation is slightly more complicated in reality than in Figure 3.2, because clouds are not stationary but are advected by winds during the 7-min observation period. This effect has to be removed in order to generate representative

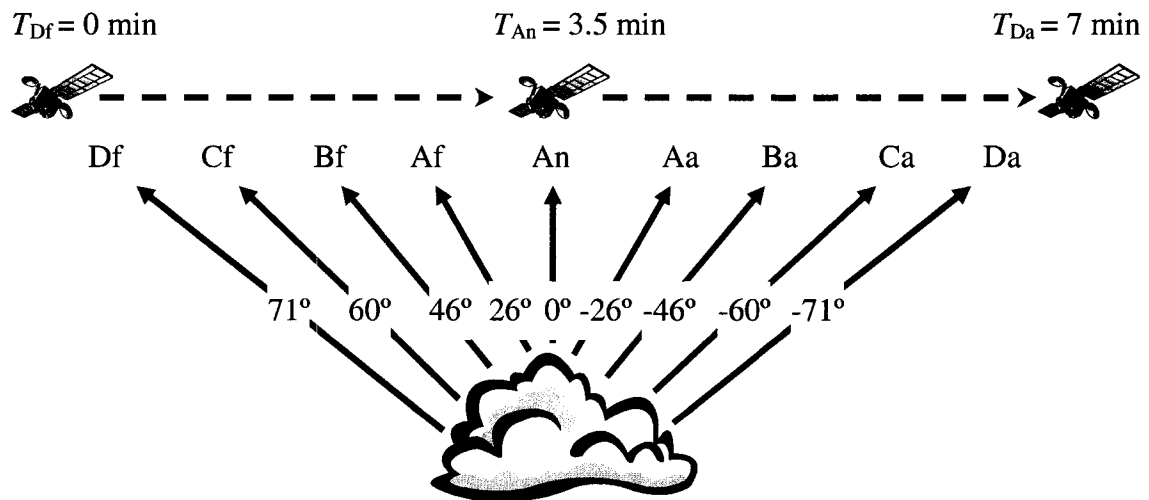


Figure 3.2 MISR imaging concept. Blue arrows represent the cloud bi-directional reflectances. Positive/negative view zenith angles correspond to the forward/aft cameras. Dashed arrows represent the direction of flight.

cloud bi-directional reflectance distributions from the multiangle measurements (see Appendix B).

The absolute uncertainty in MISR reflectances is estimated to be within 4% (1 sigma level of confidence) for bright uniform targets. Camera- and band-relative uncertainties are within 2%, while pixel-relative uncertainties are within 0.5%. These values apply over uniform targets. For contrast scenes there might be additional scene-dependent errors, such as point-spread-function effects, ghost-image effects, etc. For a detailed discussion on MISR radiometric calibration the reader is referred to Bruegge et al. (2002), Chrien et al. (2002), Abdou et al. (2002), and Appendix G.

3.1.2 Dataset

The actual data that were used in this study are depicted in Figure 3.3. A total of 28 orbits from two particular days were analyzed: orbits 6956-6969 acquired on April 9, 2001, and orbits 15330-15343 collected on November 5, 2002. Only maritime clouds were considered. Areas contaminated with sea ice were carefully removed from each orbit. This resulted in coverage between 60°N and 60°S. MISR spectral radiances are available in two formats: reprojected to the terrain or reprojected to the World Geodetic System 1984 (WGS84) surface ellipsoid (NIMA, 1997) using the Space-Oblique Mercator (SOM) projection. In this study the ellipsoid-referenced data were used. MISR data come in blocks, which consist of 2048 (cross-track) x 512 (along-track) pixels of 275 m resolution. A whole orbit comprises of 180 blocks.

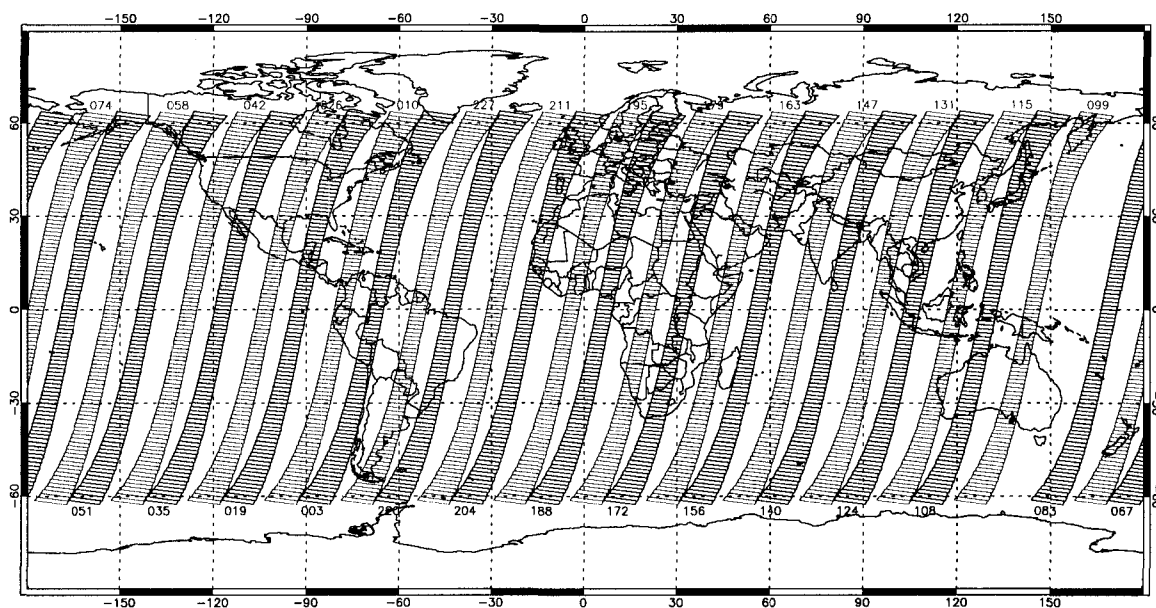


Figure 3.3 Processed MISR orbits: 6956-6969 (red), and 15330-15343 (blue). The plotted block range is 40-140 (block 90 refers to the equator). The three-digit numbers indicate to which path the given orbit corresponds out of the possible 233 unique MISR paths.

3.2 Cloud Optical Thickness Retrieval

3.2.1 Lookup-Table Interpolation Method

The MISR spectral radiances L , given in $\text{W/m}^2/\mu\text{m}/\text{sr}$, were first converted to equivalent bi-directional reflectances ρ_{BRF} by

$$\rho_{BRF} = \frac{\pi L}{I_0 \cos \theta_0} d^2. \quad (3.1)$$

Here θ_0 is the solar zenith angle, $d = d_{ES}/1 \text{ AU}$ is the ratio of the actual Earth-Sun distance d_{ES} to one astronomical unit ($1 \text{ AU} = 149,598,000 \text{ km}$), and I_0 , given in $\text{W/m}^2/\mu\text{m}$, is the solar spectral irradiance corresponding to 1 AU. The value of I_0 for the four MISR bands is given in Table 3.1. The computed bi-directional reflectances were then corrected for ozone absorption (see section 3.3.1) and Rayleigh scattering effects (see section 3.3.3). Finally, cloud optical thickness was determined by comparing the corrected MISR red band reflectance measurements with model generated values stored in look-up tables (LUTs). Simulated red band reflectances were generated by the discrete ordinate radiative transfer code DISORT v.2.1 (Stamnes et al., 1988) for a single plane-parallel cloud layer above a Lambertian ocean surface with an albedo of 5%, with no aerosols and atmospheric effects included in the simulations. Model reflectances were computed for a wide range of solar and view geometries and cloud optical thicknesses. The characteristics of LUTs are summarized in Table 3.2. A separate LUT was generated for each of the nine MISR cameras. For each camera, calculations had to be done only for

Table 3.1 Solar spectral irradiance I_0 for the MISR channels.

Channel	I_0 (W/m ² /μm)
blue	1867
green	1843
red	1524
NIR	978

Table 3.2 Look-up table characteristics.

LUT Dimension	Range	Grid Spacing
solar zenith angle	0°-80°	1°
solar azimuth angle	0°-180°	1°
An view zenith angle	0°-17°	1°
Af/Aa view zenith angle	25°-32°	1°
Bf/Ba view zenith angle	45°-49°	1°
Cf/Ca view zenith angle	59°-62°	1°
Df/Da view zenith angle	70°-72°	1°
cloud optical thickness	1-100	^a N/A

^acubic spline fit with fitting point at $\tau_c = 1, 2, 3, 4, 5, 11, 21, 41, 61, 81, 100$

a relatively narrow range of view zenith angles around the nominal camera view zenith angle. The camera-specific view zenith angle range was largest for the nadir (An) camera and got smaller and smaller for oblique cameras.

To obtain the cloud optical thickness corresponding to a particular reflectance measurement trilinear interpolation was used along the solar zenith angle, view zenith angle, and relative solar azimuth angle dimensions of the LUT and cubic spline interpolation was used along the optical thickness dimension of the LUT. Model reflectances were calculated only for 11 cloud optical thickness values ($\tau_c = 1, 2, 3, 4, 5, 11, 21, 41, 61, 81, 100$) and were interpolated for intermediate values using cubic splines. An example is shown in Figure 3.4. Panel (a) shows the reflectance as a function of cloud optical thickness for a particular solar and view geometry. The reflectance first quickly increases with optical thickness then tends to saturate at larger optical thickness values. The very smoothly varying reflectance vs. optical thickness curve can be easily fitted with splines using just a few fitting points. The original curve (black) and the fitted one (blue) are almost indistinguishable. The relative error of the fit is plotted in panel (b). The error fluctuates around zero; its largest value is a mere $\sim 0.2\%$. Therefore, spline interpolation did not seem to be a major source of error. The total interpolation error was estimated in general to be less than 3%, most of which was caused by trilinear interpolation along the solar/view zenith and relative solar azimuth angles.

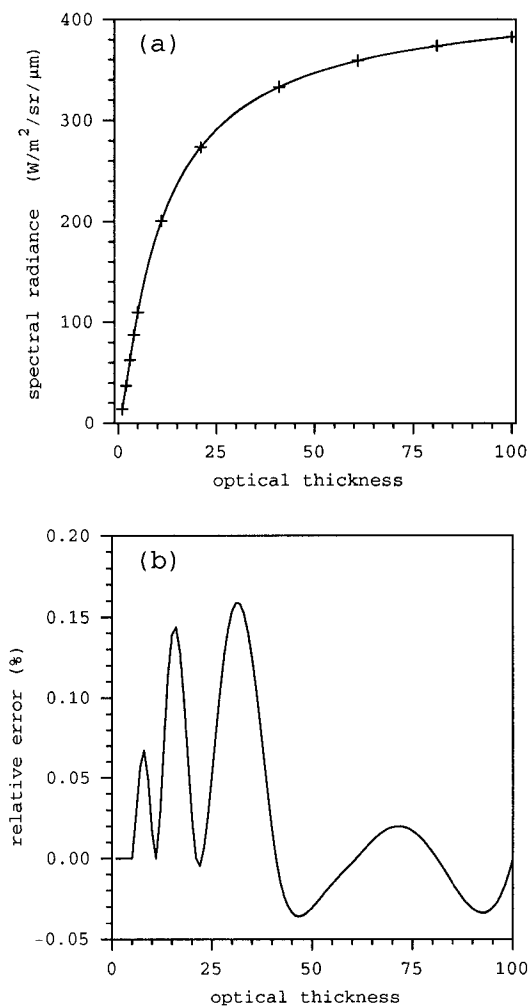


Figure 3.4 (a) Red band spectral radiance as a function of cloud optical thickness. The black curve is the original and the blue one is the spline fit. Plus signs indicate the fitting points for spline interpolation. (b) Relative error of spline interpolation as a function of cloud optical thickness. This example is for the B camera, and for a solar zenith angle of 30° and a relative solar azimuth of 45° .

3.2.2 Specification of Model Cloud Microphysics

The generation of reflectance LUTs with DISORT required the specification of cloud single scattering properties. The single scattering albedo was set to 1, that is conservative scattering was assumed. Several studies claimed the existence of excess absorption in clouds (e.g., Cess et al., 1995; Ramanathan et al., 1995; Pilewskie and Valero, 1995). If this so-called anomalous absorption did occur it would have affected my cloud optical thickness retrievals. However, recent studies based on data from the Atmospheric Radiation Measurement (ARM) program found no excess absorption at solar and near-infrared wavelengths (e.g., Ackerman et al., 2003; Sengupta and Ackerman, 2003). They concluded that measured and calculated fluxes were essentially in agreement, both for clear and cloudy columns, when observational and model uncertainties were taken into account. Therefore, I ruled out the possibility of anomalous absorption and concluded that conservative scattering was an accurate assumption for the MISR red band used in this study.

The cloud single scattering phase function was obtained from Mie calculations assuming a gamma distribution of spherical water particles. Computations were made with the MAKE_MIE_TABLE code, which is part of the spherical harmonics discrete ordinate method (SHDOM) radiative transfer package (Evans, 1998). The gamma distribution of cloud droplet sizes is

$$n(r) = ar^\alpha \exp(-br), \quad (3.2)$$

where r is the droplet radius, and the parameters a , b , and α specify the gamma distribution. The effective radius of the distribution is $R_e = (\alpha + 3)/b$, while the effective variance is $V_e = 1/(\alpha + 3)$. The parameter α controls the width of the drop size distribution. An exponential distribution is obtained with $\alpha = 0$, while a large value of α gives close to a monodisperse distribution. In this study $\alpha = 7$ was used which resulted in a narrow gamma distribution with an effective variance of $V_e = 0.1$. Boers et al. (2000) found that this is an excellent value to use for stratocumulus clouds. Because the index of refraction of water changes very slightly over the narrow MISR red band it was not necessary to integrate Mie calculations over the specific wavelength range. It was adequate to compute the single scattering phase function only at the central wavelength of the red band (672 nm). LUTs were generated for three different cloud droplet effective radii. In addition to the reference case with $R_e = 8 \mu\text{m}$, calculations were also made for $R_e = 5 \mu\text{m}$ and $R_e = 15 \mu\text{m}$. The corresponding single scattering phase functions are depicted in Figure 3.5. In general, the phase function becomes more anisotropic (more forward peaked) as the effective radius increases. The positions and magnitudes of other local phase function maxima (e.g. rainbow peak, etc.) also systematically change with effective radius.

It is noted that DISORT actually required the Legendre-expansion representation of the phase function. The number of Legendre terms increased with increasing effective radius and ranged from 300 to 1000 between $R_e = 5 \mu\text{m}$ and $R_e = 15 \mu\text{m}$. Prior to version 2.1 DISORT used only the first $NSTR$ Legendre components, where $NSTR$ is the number

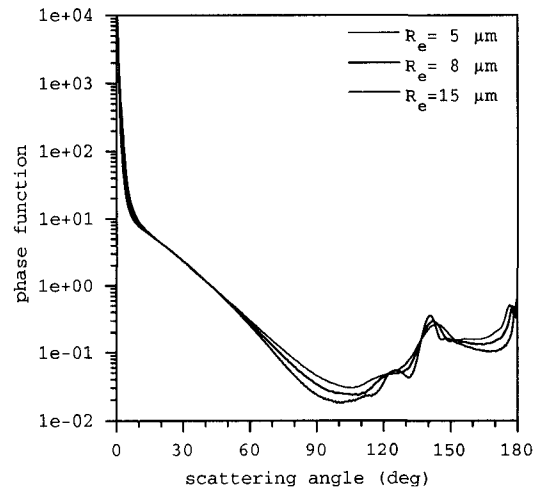


Figure 3.5 Single scattering phase functions at $\lambda = 672 \text{ nm}$ for a gamma drop size distribution with $\alpha = 7$ and for effective radii $R_e = 5 \mu\text{m}$, $R_e = 8 \mu\text{m}$, and $R_e = 15 \mu\text{m}$.

of streams. Version 2.1 represents a significant improvement because it is capable of handling all of the several hundred Legendre terms irrespective of the number of streams used. The accuracy of reflectance calculations increases with the number of streams. However, the computational time also increases as the cube of $NSTR$, which makes the calculations unpractical for a large number of streams. In this study the LUTs were generated with $NSTR = 48$, which struck a reasonable balance between accuracy and computational time.

The choice of the three different effective radii considered in this study was somewhat arbitrary. Retrievals using non-absorbing channels in the visible wavelength region cannot determine the effective radius because cloud reflectance in these channels is primarily a function of cloud optical depth and depends only weakly on effective radius. Therefore, such retrievals usually assume the same fixed value of effective radius for every cloud. For instance, the International Satellite Cloud Climatology Project (ISCCP) (Rossow and Schiffer, 1991) uses a constant value of $R_e = 10 \mu\text{m}$. The retrieval of effective radius from space requires additional information, such as the measurement of reflectance in a water-absorbing channel in the NIR (Nakajima and King, 1990), or of polarization (Breon and Goloub, 1998), or of liquid water path (Masunaga et al., 2002). There is a general scarcity of well established global climatologies of cloud droplet effective radius. Han et al. (1994) conducted a near-global survey of droplet effective radius using AVHRR (Advanced Very High Resolution Radiometer) data, and Breon and Colzy (2000) published a global effective radius data set based on polarization measurements obtained by the POLDER (Polarization and Directionality of the Earth's

Reflectances) instrument. Both studies found a pronounced land-ocean contrast with cloud droplets being 2-3 μm smaller over land than over ocean. Han et al. (1994) also found that droplet radii are about 1 μm smaller in marine clouds of the Northern Hemisphere than in the Southern Hemisphere. Breon and Colzy (2000), on the other hand, documented a large zonal gradient in the southern oceans, with very small droplets close to the Antarctic continent. There was also a clear bias between the two studies. Han et al. (1994) estimated a global mean droplet effective radius of 12 μm for marine clouds and 8-9 μm for continental clouds, whereas Breon and Colzy (2000) obtained values roughly 2 μm smaller than these. The satellite retrievals can be contrasted with in-situ measurements (Miles et al., 2000). In-situ observations are usually assumed to be more accurate than satellite retrievals. However, they suffer from limited geographical coverage. In-situ data also confirm the land-ocean contrast in effective radius. However, they indicate systematically lower values of R_e than satellite measurements. The global average droplet effective radius in the comprehensive database compiled by Miles et al. (2000) is $\sim 9 \mu\text{m}$ over oceans and $\sim 5 \mu\text{m}$ over land, at least for stratiform clouds.

The typical values of cloud droplet effective radius can also be constrained by microphysical theory. Rossow (1978) estimated that typical cloud droplet radii should be in the range 5-15 μm in nonprecipitating clouds and in the range 10-30 μm in precipitating clouds. Larger precipitation-sized drops are assumed to be quickly removed from the cloud by collision-coalescence. It has been suggested that the occurrence of precipitation is controlled by a critical effective radius (Gerber, 1996), which marks the value at which 50% of the liquid water is associated with drizzle/precipitation-sized

drops. This idea has been supported by measurements obtained by Boers et al. (1998), Rosenfeld and Gutman (1994), and Rosenfeld (1999), who found the rapid onset of precipitation as the effective radius increased beyond $\sim 14 \mu\text{m}$. Not only do large drops fall out of the cloud but they also become radiatively inactive in the visible optics regime, and thus do not contribute to the cloud optical thickness. Based on the above, Boers and Rotstajn (2001) concluded that it is improbable to observe clouds with an effective droplet radius exceeding $16\text{--}17 \mu\text{m}$ near cloud top, because beyond those values clouds will disappear through precipitation.

The situation is even more complicated in reality due to the variation of droplet effective radius with height. Measurements indicate that the effective radius tends to increase with height within the cloud, which is in qualitative agreement with the current state-of-the-art in parcel theory. This makes the comparison of effective radius observations difficult because different methods may sample different levels within the cloud. It is known, for example, that retrievals based on bi-spectral (visible and NIR) reflectance measurements are biased towards the cloud top (Nakajima et al., 1991). This complexity is difficult to account for in cloud optical thickness retrievals. The best one can hope for is to arrive at some vertical average effective radius value that is more or less representative of the cloud as a whole.

Based on the above discussion, it was concluded that the cloud droplet effective radius range $5\text{--}15 \mu\text{m}$ considered in this study covered most of the variation in my data set, and that the reference value of $R_e = 8 \mu\text{m}$ was generally reasonable for liquid oceanic clouds. The retrieved plane-parallel cloud optical thickness was slightly sensitive to the

value of the drop effective radius. This sensitivity could be estimated from the similarity principle (van de Hulst, 1980), which states that

$$\tau_c (1 - \omega_0 g) = \tau'_c (1 - \omega'_0 g'), \quad (3.3)$$

where τ_c , ω_0 , and g are the cloud optical thickness, the single scattering albedo, and the asymmetry factor, respectively. In equation (3.3) the left-hand side and the right-hand side refer to two different phase functions (and thus effective radii). Considering conservative scattering (i.e., $\omega_0 = \omega'_0 = 1$) the relative change in the cloud optical thickness can be expressed from equation (3.3) as

$$(\tau'_c - \tau_c) / \tau_c = \frac{g' - g}{1 - g'}. \quad (3.4)$$

Table 3.3 lists the asymmetry factors and relative changes calculated from equation (3.4) for the three different phase functions used in this study. The values in Table 3.3 indicate what the relative changes in the plane-parallel optical thickness obtained assuming $R_e = 8 \mu\text{m}$ would be if in fact the actual effective radius were $R_e = 5 \mu\text{m}$ or $R_e = 15 \mu\text{m}$. As shown, the uncertainty in the effective radius introduces an approximately $\pm 8\%$ uncertainty in the retrieved plane-parallel cloud optical thickness. Assuming an effective radius that is larger (smaller) than the actual one results in an overestimation (underestimation) of the plane-parallel optical thickness. ISCCP obtained similar

Table 3.3 Droplet effective radius, asymmetry factor, and relative change in retrieved cloud optical thickness.

R_e	g	$(\tau'_c - \tau_{c,8}) / \tau_{c,8}$
5 μm	0.8441	-8%
8 μm	0.8565	0%
15 μm	0.8677	+8%

uncertainty estimates. The assumption of a fixed effective particle radius of 10 μm produced a random error of about 7%, a low bias of about 1% over oceans, and a high bias of about 1-2% over land in their cloud optical thicknesses (Rossow and Schiffer, 1999). These error estimates, however, are meaningful only if clouds are truly plane-parallel. In real clouds other factors, such as 3-D effects, are likely to dominate the error budget of optical thickness retrievals.

3.3 Atmospheric Correction

3.3.1 Ozone Correction

The correction formula

The measured visible radiances had to be corrected for ozone absorption due to the Chappuis band. The Chappuis band is a broad ozone absorption band in the visible wavelength region centered at ~600 nm and extending from 400 nm to 800 nm. This absorption band is much weaker than, for example, the strong UV absorption feature centered at ~250 nm. Nevertheless, its effect on the measured radiances could not be neglected. Figure 3.6 shows the ozone absorption cross-section, σ_{O_3} , in the Chappuis band and the relative spectral response functions of the four MISR bands. Ozone absorption is strong in the green band, moderate in the red band, and practically negligible in the blue and NIR bands.

Absorption due to ozone occurs predominantly above the cloud and Rayleigh scattering layers, hence it can be treated separately from scattering processes. The ozone-corrected reflectance, $R_{O_3}^{corr}$, was calculated from the measured top-of-the-atmosphere reflectance, R , by

$$R_{O_3}^{corr} = R / \exp \left[-\tau_{O_3} (1/\cos \theta_0 + 1/\cos \theta) \right], \quad (3.5)$$

where τ_{O_3} is the total column ozone optical depth and θ_0 , and θ are the solar and view zenith angles, respectively. In equation (3.5) it was assumed that the double attenuation

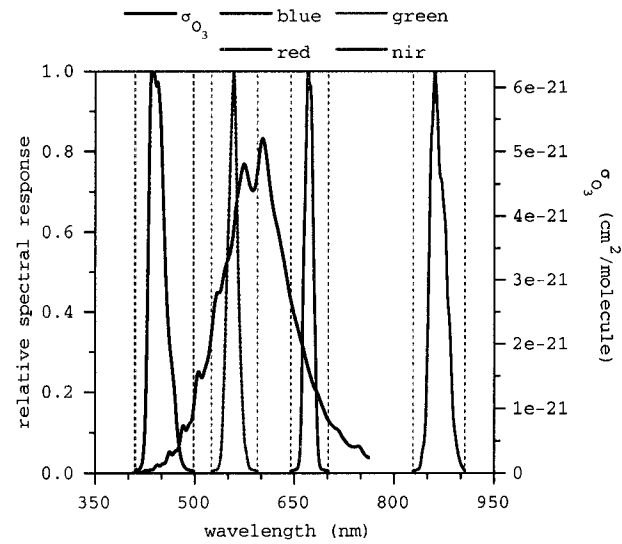


Figure 3.6 Chappuis band ozone absorption cross-section σ_{O_3} at a temperature of 220 K according to Burkholder and Talukdar (1994). The colored solid lines represent the MISR spectral response functions S . The colored dotted lines correspond to the wavelength regions over which the response functions are $\geq 0.5\%$.

through the solar path and the view path could be calculated from Beer's law. Strictly speaking, Beer's law, i.e. exponential transmission, does not apply over finite spectral intervals. This is especially true in the near-infrared part of the solar spectrum (longwards of 700 nm) and throughout the terrestrial spectrum (longwards of 4000 nm), where the absorption cross-section for most absorbing atmospheric gases (e.g. water vapor, carbon dioxide, and ozone) varies rapidly and also very erratically with wavelength. Special methods such as the exponential-sum-fitting-of-transmission functions (ESFT) technique (Sun and Rikus, 1999) or its close relative the k -distribution method (Lacis and Oinas, 1991) are usually employed to cope with this erratic behavior of the absorption cross section across a finite spectral interval. Both of these techniques approximate the transmission function for the given spectral interval with a sum of exponential functions. However, the absorption cross-section for ozone in the visible spectral range varies smoothly with wavelength (see Figure 3.6). Therefore, by using this continuum feature of the cross-section it was possible to define proper averages over wide spectral intervals such that Beer's law held approximately. Stamnes and Tsay (1990) showed that a single-band integration over the entire Chappuis band yields an accuracy in transmission calculations better than 0.2%. Hence, Beer's law in equation (3.5) could be applied safely over the much narrower spectral intervals represented by the MISR channels. Comparisons made between transmission calculations obtained by equation (3.5) and by the k -distribution method showed excellent agreement (see end of next section). Details of calculating the total column ozone optical depth, τ_{O_3} , in equation (3.5) are discussed in Appendix C.

Effect of O_3 correction on reflectances

The relative increase in the MISR red band reflectances due to ozone correction, $(R_{O_3}^{corr} - R) / R_{O_3}^{corr}$ (hereafter ozone ‘absorption’), is plotted in Figure 3.7 as a function of solar zenith angle. The black curves correspond to the nadir (An) camera while the red curves refer to the most oblique (Df/Da) cameras. These curves were computed with MODTRAN. Solid lines are for the tropical atmosphere with the lowest total column ozone (277 DU) among the MODTRAN models and dashed lines are for the midlatitude winter atmosphere with the largest total column ozone (377 DU) among the MODTRAN models. My absorption calculations obtained using equation (3.5) with the Burkholder data set are plotted as blue circles. There is excellent agreement between the MODTRAN transmission calculations and the simple correction method based on equation (3.5). Ozone absorption steadily increases with solar zenith angle. This increase is slow up to a solar zenith angle of $\approx 60^\circ$, above which it is much more rapid. Typical values of the ozone absorption are 2% to 6% for the nadir camera and 5% to 9% for the most oblique Df/Da cameras, depending on the solar zenith angle and ozone abundance. Ozone absorption for the rest of the oblique cameras is in between these two extremes.

The above results obtained with MODTRAN represent simple clear sky transmittance calculations with no cloud or surface scattering included. MODTRAN uses k -distributions (or ESFT) to compute ozone absorption. The excellent agreement between MODTRAN and equation (3.5) shows that the k -distribution method is overkill for the Chappuis band ozone absorption especially when such narrow bandpasses are considered as the MISR channels. In these cases simple band average ozone absorption coefficients

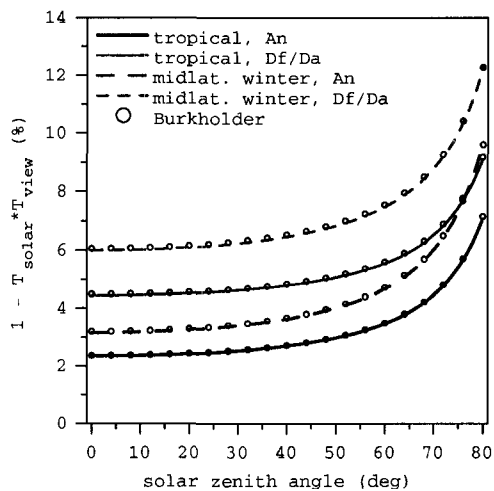


Figure 3.7 Ozone absorption as a function of solar zenith angle for the An nadir camera (black) and the most oblique Df/Da cameras (red). Solid/dashed lines correspond to MODTRAN calculations using the tropical/midlatitude winter atmosphere. Blue circles refer to results obtained with equation (3.5) using the Burkholder and Talukdar (1994) data set. Here T_{solar} and T_{view} are the solar and view path transmittances, respectively.

can be safely used with equation (3.5). The particular MODTRAN version (v.3.7) that was available to me did not handle (cloud) scattering processes particularly well. As a final test of my ozone correction method calculations were made including cloud and surface scattering using the Santa Barbara DISORT Atmospheric Radiative Transfer (SBDART) program. SBDART (Ricchiazzi et al., 1998) is a plane-parallel radiative transfer code that represents a marriage between a discrete ordinate radiative transfer module (DISORT) and a low-resolution atmospheric transmission model (LOWTRAN 7). SBDART relies on the k -distribution method (using a three-term exponential fit to the transmission) to handle atmospheric absorption and can easily incorporate cloud scattering as well. Top-of-the-atmosphere spectral radiances were generated with SBDART for the MISR red band with and without the ozone layer. Ozone absorption was then calculated from these radiances. A comparison of ozone absorption as calculated by SBDART and by equation (3.5) is shown in Table 3.4 for a tropical clear sky atmosphere above a seawater surface. There was very good agreement between the two sets of results. Finally, Table 3.5 gives the ozone absorption when a cloud layer of optical thickness $\tau = 50$ with a C1 phase function and effective radius of $10 \mu\text{m}$ was included at different altitudes. This case was for the nadir camera and overhead sun (i.e. corresponded to row 1 in Table 3.4). The inclusion of the cloud layer did not change the results significantly. The effect of ozone absorption on the TOA radiances decreased with cloud altitude. This decrease was small, however, for low and mid level clouds because the troposphere below 10 km altitude contains $\leq 10\%$ of the total column ozone (i.e. most of the ozone is above clouds). Therefore, it was not necessary to consider cloud

Table 3.4 Ozone absorption for a clear tropical atmosphere above a sea surface as calculated by SBDART and equation. (3.5).

Solar/View Geometry	SBDART	Eq. (3.5)
$\theta_0 = 0^\circ, \theta = 0^\circ, \Delta\phi = 0^\circ$	2.3%	2.4%
$\theta_0 = 80^\circ, \theta = 0^\circ, \Delta\phi = 0^\circ$	7.2%	7.1%
$\theta_0 = 0^\circ, \theta = 70^\circ, \Delta\phi = 0^\circ$	4.4%	4.5%
$\theta_0 = 80^\circ, \theta = 70^\circ, \Delta\phi = 0^\circ$	9.0%	9.2%

Table 3.5 Ozone absorption as a function of cloud height as calculated by SBDART for a tropical atmosphere, a cloud with $\tau_c = 50$, $R_e = 10 \mu\text{m}$, C1 phase function, and $\theta_0 = 0^\circ, \theta = 0^\circ, \Delta\phi = 0^\circ$.

Cloud Altitude	Ozone Absorption
1 km	2.3%
5 km	2.2%
10 km	2.1%
15 km	2.0%
20 km	1.8%

height in the ozone correction for the low and mid level clouds dominating the data set used in this study (high, i.e. ice, clouds were filtered out by the phase mask).

3.3.2 Water Vapor Correction

The only other atmospheric constituent that might affect the MISR red band radiances is water vapor. To estimate the magnitude of water vapor absorption model calculations were performed using SBDART and MODTRAN. Table 3.6 gives the results for a number of solar and view geometries. The calculations were made for the tropical atmosphere that was the wettest among the built-in SBDART/MODTRAN models with a total column water vapor amount of 4.12 g/cm^2 . The results are for clear sky with no aerosols and no clouds included and with water vapor as the only absorbing constituent. From Table 3.6 I concluded that the absorption due to water vapor was $<1\%$ for the MISR red band even for large solar and view zenith angles. Therefore, the effect of water vapor on the measured red band radiances was neglected in this study.

Table 3.6 Water vapor (WV) absorption in the MISR red band for a clear tropical atmosphere above a sea surface as calculated by SBDART and MODTRAN.

Solar/View Geometry	WV Absorption
$\theta_0 = 0^\circ, \theta = 0^\circ, \Delta\phi = 0^\circ$	0.4%
$\theta_0 = 80^\circ, \theta = 0^\circ, \Delta\phi = 0^\circ$	0.6%
$\theta_0 = 0^\circ, \theta = 70^\circ, \Delta\phi = 0^\circ$	0.6%
$\theta_0 = 80^\circ, \theta = 70^\circ, \Delta\phi = 0^\circ$	0.6%

3.3.3 Rayleigh Correction

General considerations

The sensor-measured TOA reflectances had to be corrected for Rayleigh scattering contributions. Since the Rayleigh optical thickness in the visible wavelength region is small, Rayleigh scattering is usually neglected in cloud optical thickness retrievals. Wang and King (1997), however, showed that the Rayleigh contribution to the reflected signal could significantly affect the retrieved optical thickness for thin clouds and for large solar/view zenith angles and all clouds. Considering that MISR has several oblique cameras with large view zenith angles (particularly the C and D cameras), Rayleigh correction seemed important. The algorithm used in this study was essentially that of Wang and King (1997). For a detailed derivation see Appendix D.

I emphasize here the approximate nature of this technique. First, only the above-cloud molecular scattering was considered. This simplification seemed reasonable because most of the high clouds were likely to be filtered out by the MODIS phase mask. Thus most of the Rayleigh scattering occurred above the clouds in my data set. Second, polarization was neglected throughout this study. As Hansen (1971) shown, neglecting polarization in calculating the intensity of sunlight reflected by water clouds (in the absence of the atmosphere) introduces an error $\leq 1\%$. For pure Rayleigh scattering, however, this error in the intensity can be as high as $\sim 10\%$ for certain scattering geometries and parameters (Adams and Kattawar, 1970; Mishchenko et al., 1994). For the combined cloud-atmosphere system the measured signal is dominated by cloud reflectance, therefore the potentially large errors in the relatively small Rayleigh

contribution introduce much smaller errors in the total signal. Third, the Rayleigh correction algorithm was based on the single scattering approximation with using only an empirical correction factor, C_m , to account for multiple scattering (see Appendix D). Despite the above limitations the algorithm still improved the general accuracy of cloud optical thickness retrievals.

Effect of Rayleigh correction on optical thickness retrievals

The performance of the Rayleigh correction algorithm was tested for all cameras and for a wide range of solar geometries and cloud optical thicknesses. In all of these tests, the algorithm significantly reduced the error in the retrieved cloud optical thickness due to Rayleigh scattering. An example is shown in Figure 3.8 for the most oblique D camera. Here top-of-the-atmosphere reflectances were generated by DISORT for an ocean-cloud-atmosphere model consisting of a Lambertian ocean surface with an albedo of $\alpha_{sfc} = 0.05$, a cloud layer, and an atmospheric layer with an optical thickness of 0.045. These reflectances were then inverted for cloud optical thickness with and without Rayleigh correction. The relative error in the retrieved optical thickness was calculated as a function of solar zenith angle and optical thickness. Panel (a) depicts the relative errors without Rayleigh correction, while panel (b) gives the residual errors after Rayleigh correction. The very significant reduction in the retrieval error due to Rayleigh correction is obvious. Without the correction extreme retrieval errors ($>> 100\%$) can occur for $\theta_0 > 65^\circ$, especially for thinner clouds. The Rayleigh correction reduces the retrieval

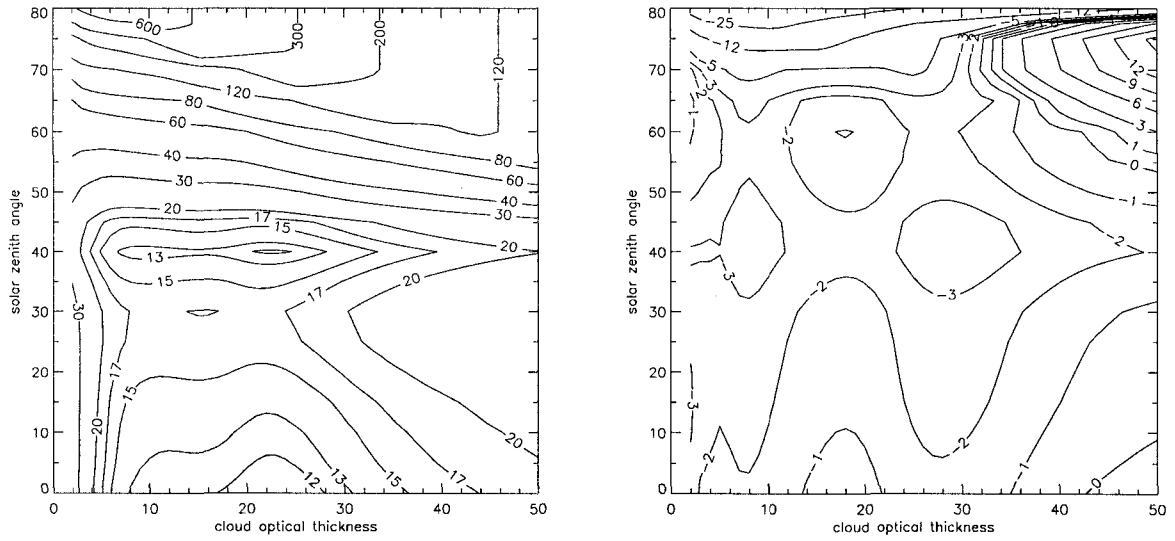


Figure 3.8 Relative error (in percent) in retrieved cloud optical thickness: (a) without Rayleigh correction, and (b) with Rayleigh correction. The following parameters were used in both cases: $\theta = 71^\circ$, $\Delta\phi = 150^\circ$, $\alpha_{sfc} = 0.05$, $\tau_r = 0.045$, $C_m = 0.78$, and $i = 1$ (see Appendix D).

errors generally below 5% for $\theta_0 < 65^\circ$. For larger solar zenith angles, however, residual errors up to 10-20% can still occur. This demonstrates the limitations of accounting for multiple scattering effects through a single constant factor (C_m). A slightly different value of C_m would give better results for larger solar zenith angles but it would increase the errors for smaller solar zenith angles. This multiple scattering correction factor is in fact a function of many variables (solar and view geometries, cloud optical thickness, etc.). Therefore a given value that works for certain conditions might not work for others. In this study I used the value $C_m = 0.78$ that gave the best overall result. Also note that Figure 3.8 represents the worst-case scenario with the most oblique D camera and the largest possible Rayleigh optical thickness ($\tau_r = 0.045$ in the red band). For less oblique cameras (i.e. smaller view zenith angles) and higher cloud tops (i.e. thinner above-cloud air layer) Rayleigh scattering effects are less important.

Effect of Rayleigh correction on angular optical thickness distributions

Let us now examine the effect of Rayleigh correction on the retrieved cloud optical thickness distributions. Figure 3.9 shows optical thickness distributions obtained with and without Rayleigh correction for all nine MISR cameras over a particular marine stratocumulus cloud field. Note that Rayleigh effects are most important for the D and C cameras, and maybe for the B cameras, but they are basically insignificant for the nadir (An) and near-nadir (A) cameras. Also note the different signs of the correction for the forward (f) and aftward (a) cameras. For all the forward cameras (and for the nadir

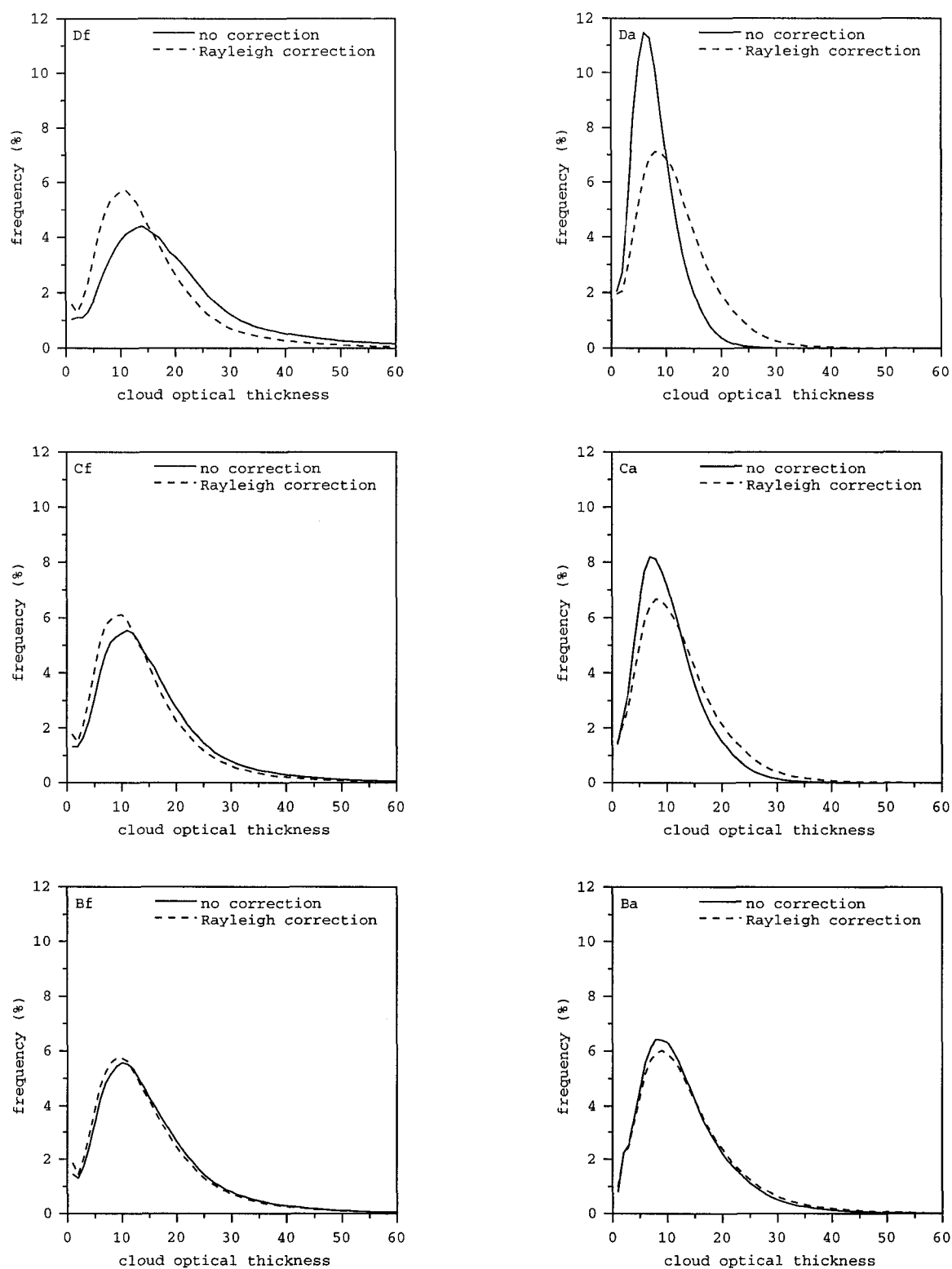


Figure 3.9 Effect of Rayleigh correction on optical thickness distributions for the Df/Da, Cf/Ca, and Bf/Ba cameras. Marine Sc field in block 124 of orbit 6956.

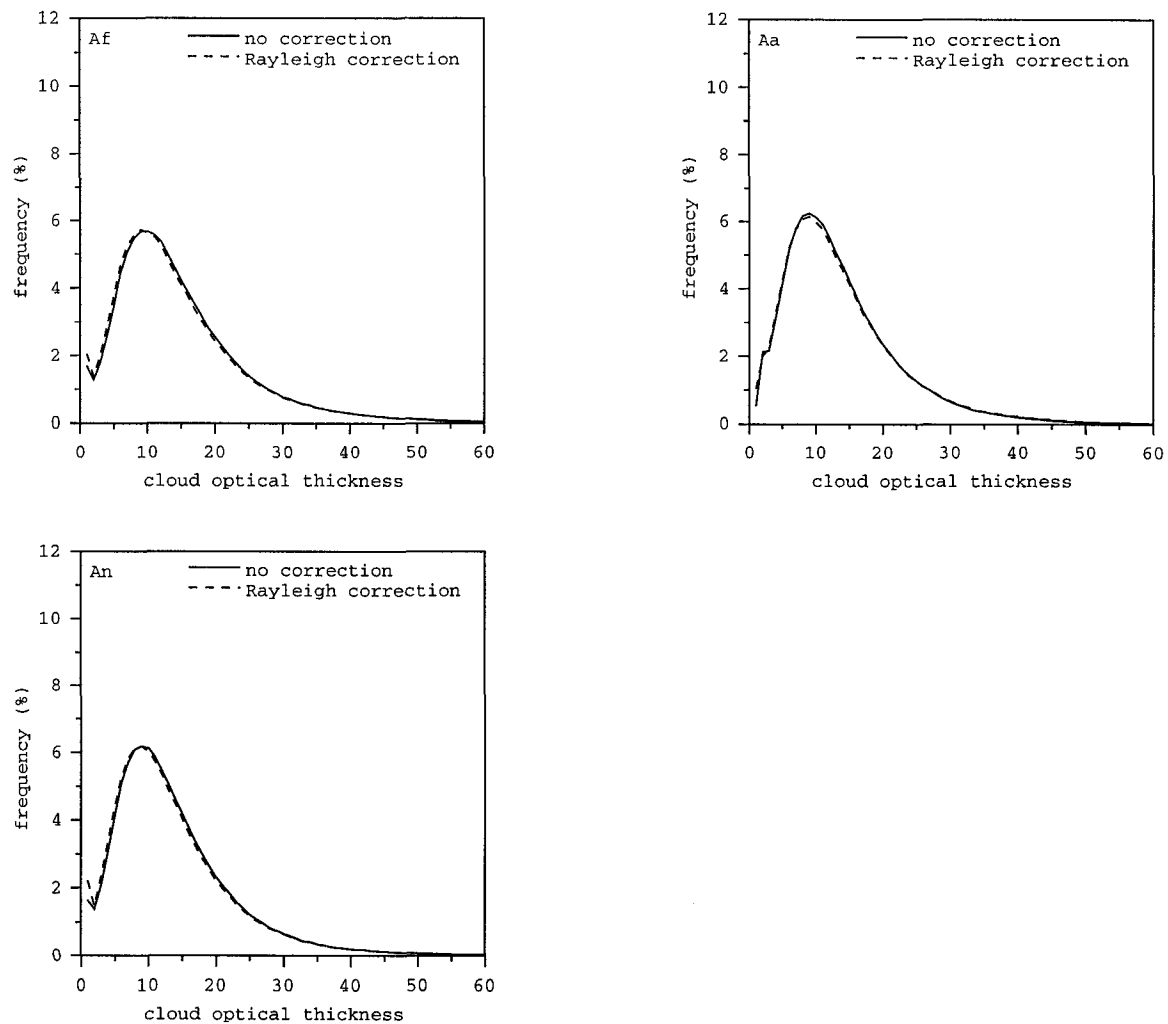


Figure 3.9–*Continued* Effect of Rayleigh correction on optical thickness distributions for the Af/Aa, and An cameras. Marine Sc field in block 124 of orbit 6956.

camera as well) the Rayleigh correction shifts the optical thicknesses towards smaller values. For all the aftward cameras, on the other hand, the optical thicknesses are shifted towards larger values due to the correction. This asymmetry between the forward and aft cameras is due to the fact that these two sets of cameras sample different portions of the scattered radiation. In this example from the southern hemisphere the forward cameras actually sampled the backscattered signal, while the aft cameras sampled forward scattering. Rayleigh scattering enhanced the weaker backscattered signal and reduced the stronger forward scattered signal.

Finally, Figure 3.10 shows all the angular optical thickness distributions from Figure 3.9 together, but separately for the uncorrected (panel (a)) and the corrected (panel (b)) cases. Since this example was a marine stratocumulus field, which is arguably the closest to the plane-parallel cloud model, relatively good agreement was expected among the retrieved angular optical thicknesses. Without Rayleigh correction the Df/Da and Ca cameras were clearly outliers. After the correction the angular optical thickness distributions were fairly consistent with each other (at least their modal values were in a much better agreement).

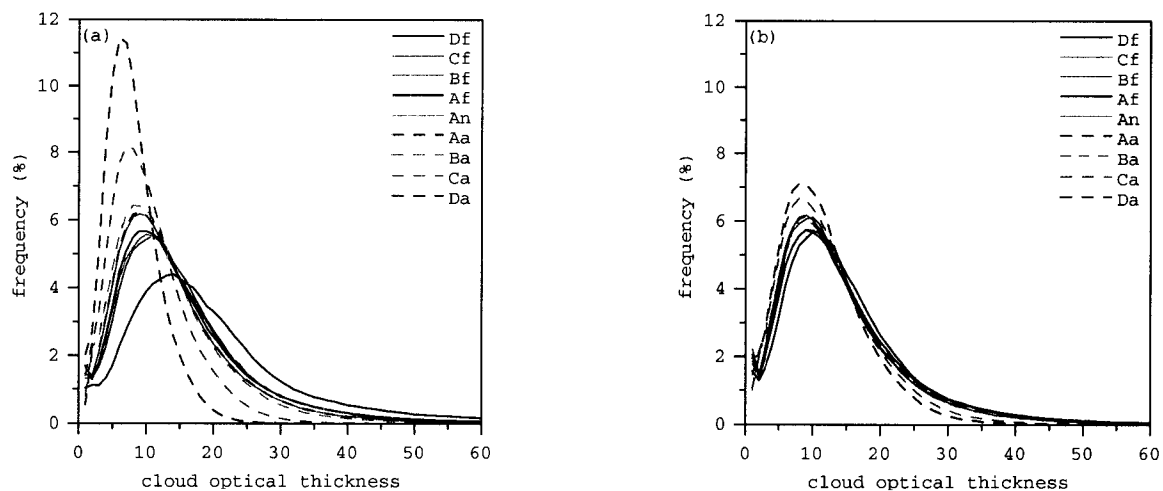


Figure 3.10 Angular cloud optical thickness distributions: (a) without Rayleigh correction, and (b) with Rayleigh correction. Marine Sc field in block 124 of orbit 6956.

CHAPTER 4 RESULTS

In this chapter I first evaluate the theoretical estimate of the global mean atmospheric liquid water path given by Pruppacher and Jaenicke (1995) (hereafter PJ95). The sensitivity of their global mean estimate to uncertainties in the input parameters is investigated. Then follows a study on the validity of the plane-parallel optical thickness retrieval method. Next, a comparison between the optical and microwave techniques to obtain cloud liquid water path is given. Finally, the construction of global liquid water path distributions closes the chapter.

4.1 Improving the Theoretical Estimate

PJ95 estimated the global mean liquid water amount in clouds based on microphysical arguments. They only considered the lower 6 km of the atmosphere. From global radiosonde observations for the 1987-1990 period Wentz and Spencer (1998) determined that the typical value of the freezing level is about 1 km at very high latitudes, it ranges from 2 to 4 km in midlatitudes, and it reaches a value of 5 km in the Tropics. Therefore, it seems reasonable to assume that most of the cloud liquid water resides in the first 6 km of the atmosphere. Out of the 10 major cloud types the cirriform clouds (cirrus, cirrostratus, and cirrocumulus) were excluded from their study, because by definition they only include ice. The remaining 7 cloud types were divided into 5 groups with altostratus and altocumulus, and stratus and stratocumulus grouped together, probably due to their similar microphysical properties. Characteristic values of cloud amount c_c , cloud thickness h_c , and cloud liquid water content w_c were selected from Lelieveld

(1989), Churchill and Houze (1984), Matveev (1984), Atkinson (1981), Pruppacher and Klett (1978), Mason (1971), and Borovikov (1963). Table 4.1 summarizes these parameters. It is noted here that there were no error bars on these published observational values. The liquid water path for each individual cloud category was determined from the above three parameters as

$$LWP = c_c h_c w_c, \quad (4.1)$$

which is given in column 5 of Table 4.1. If c_c is in percent, h_c is in meter, and w_c is in g/m^3 then LWP will be in g/m^2 . The global mean liquid water amount in all clouds was determined by adding up the 5 individual values, which resulted in 382 g/m^2 . Cumulonimbus contained by far the most liquid water with half of the global mean stored in this cloud type alone. Nimbostratus and cumulus contained about the same amount of liquid water, their combined contribution to the mean was around one third. Finally, the total contribution of the last two categories was little less than one fifth, with stratus/stratocumulus being the driest cloud type.

Sensitivity to c_c

Let us examine the sensitivity of the above liquid water path estimates to the assumed cloud amounts. There is a scarcity of well-established cloud amount climatologies. The two most comprehensive and most frequently used datasets are the

Table 4.4 Global average cloud amount, cloud thickness, cloud liquid water content, and cloud liquid water path from PJ95.

Cloud Type	c_c (%)	h_c (km)	w_c (g/m ³)	LWP (g/m ²)
Cb	5	3.8	1.0	190
Ns	6	2.7	0.4	64
Cu	7	1.7	0.5	59
As/Ac	23	1.0	0.2	46
St/Sc	23	1.0	0.1	23
Total	N/A	N/A	N/A	382

cloud atlases compiled by Warren et al. (1985, 1986), and the cloud climatology obtained by the ISCCP (Rossow and Schiffer, 1999). The Warren atlas summarizes surface observations and thus represents a bottom-up view of clouds, while the ISCCP cloud amounts were computed from satellite observations using automated threshold techniques and hence correspond to a top-down view of clouds. It is noted here that surface observers determine “sky cover” while satellites determine “earth cover”. The average difference between these two quantities, however, was found to be relatively small compared to other sources of uncertainty (Henderson-Sellers and McGuffie, 1990). This is due to the fact that satellite cloud cover is estimated from a variety of viewing zenith angles. Detailed comparisons between the ISCCP and other surface and satellite based cloud amounts can be found in Rossow et al. (1993) and Hahn et al. (2001). The largest differences generally occur between surface observations and satellite measurements. Therefore, the Warren atlas and ISCCP seem to represent the two extremes in cloud amount, and it is believed that they give a good measure of uncertainty in this quantity.

The cloud amounts referring to the 5 individual groups as determined by the Warren atlas and the ISCCP are given in Table 4.2. Here the amounts assumed by PJ95 were also included (column 2 from Table 4.1). The ISCCP cloud type amounts were determined from daytime observations only. This is because the ISCCP cloud types are defined in terms of their cloud top pressures and optical thicknesses, and the optical thickness can be determined only during daytime from the visible reflectance channels. In addition to the “all cloud” (liquid plus ice) amounts (column 4 in Table 4.2), ISCCP also archives the liquid only amounts (column 5 in Table 4.2). Liquid clouds were identified

Table 4.2 Cloud type amounts (%) according to PJ95, Warren's surface climatology, and ISCCP-D2 satellite dataset.

Cloud Type	PJ95	Warren Atlas	ISCCP All Clouds	ISCCP Liquid Clouds Only
Cb	5	5.2	2.6	-
Ns	6	5.9	2.1	1.1
Cu	7	9.6	12.5	11.3
As/Ac	23	22.0	17.1	8.2
St/Sc	23	29.1	14.0	12.9
Total	64 ^a /50.8 ^b	71.8 ^a /55.4 ^b	48.3 ^{a/-} ^b	33.5 ^{a/-} ^b

^aarithmetic sum

^bassuming random overlap

as having a cloud top temperature above 260 K. The total (arithmetic sum) cloud amounts for PJ95, Warren atlas, and ISCCP are 64%, 72%, and 48%, respectively. The large scatter in the total is due to the fact that the former two data sets do not account for cloud overlap, while the ISCCP satellite data set, by its nature, does. If the total cloud cover is calculated assuming random cloud overlap, that is $c_{rand}^{total} = 1 - \prod_{i=1}^5 (1 - c_i)$ where c_i are the individual cloud type amounts, the PJ95 and Warren atlas totals are reduced to 51%, and 55%, respectively. These values are in much better agreement with the ISCCP total, and indicate that about half the planet is covered by clouds containing some liquid.

As shown, the values used by PJ95 are in fairly good agreement with the ones reported in the Warren atlas. This is no surprise, because their cloud amounts were also based on a set of surface observations, though probably not on such a comprehensive one as the Warren atlas. The differences are largest for cumulus and stratus/stratocumulus, both of which have about 30% larger cloud coverages according to the Warren atlas. The discrepancies between ISCCP and the assumptions in PJ95 are, however, more substantial. ISCCP generally underestimates the cloud amounts. Most importantly, ISCCP indicates much smaller amounts both for cumulonimbus and nimbostratus; about one half and one third, respectively, of the values in PJ95. The reduction in the amount of altostratus/altocumulus and stratus/stratocumulus is around 25% and 40%, respectively. Cumulus, on the other hand, occurs about 80% more frequently according to ISCCP. Comparing the ISCCP total and liquid only cloud amounts reveals the following. All cumulonimbus clouds were identified as “ice”. This is not surprising, since these clouds

are the most vigorous convective clouds with the highest cloud tops, that is, lowest top temperatures. The midlevel nimbostratus and altostratus/altocumulus clouds are equally likely to fall into the ice and liquid categories. Finally, cumulus and stratus/stratocumulus clouds are almost always liquid clouds, according to ISCCP. This seems reasonable considering that these are the lowest, and hence the warmest, clouds. This also means that the clouds categorized by ISCCP as cumulus are of the shallower (fair weather) cumulus humilis and cumulus mediocris types rather than the thicker cumulus congestus ones, which are more likely to contain some ice as well. This latter type of cumulus is likely to be misclassified as one of the ISCCP midlevel clouds.

The effect on the computed liquid water path of changing the cloud amounts while keeping PJ95's assumptions on cloud thicknesses and liquid water contents is summarized in Table 4.3. For completeness, the original *LWP* estimates of PJ95 were also included in column 2. Using cloud amounts from the Warren atlas resulted in a slight (~8%) increase in the total cloud liquid water path. The increase in *LWP* was largest for cumulus due to a 30% increase in the cloud amount. A small increase also occurred for cumulonimbus and stratus/stratocumulus. Using the ISCCP cloud amounts, on the other hand, caused a large (~25%) drop in the total mean *LWP*, its value decreased by close to 100 g/m². This was largely due to a significant decrease in the global mean liquid water amount of the wettest cumulonimbus and nimbostratus clouds. ISCCP severely underestimates the frequency of these cloud types compared to surface observations. The *LWP* of As/Ac and St/Sc also decreased although to a much smaller extent. The above were partially compensated by a significant increase in the *LWP* of cumulus thanks to a

Table 4.3 Cloud liquid water path (g/m^2) as calculated from equation (4.1) using cloud amounts from PJ95, Warren's surface climatology, and ISCCP-D2 satellite dataset (see Table 4.2). All other parameters are unchanged and are as indicated in Table 4.1.

Cloud Type	LWP_{PJ95}	LWP_{Warren}	LWP_{ISCCP}
Cb	190	197	99
Ns	64	63	23
Cu	59	81	106
As/Ac	46	44	34
St/Sc	23	29	14
Total	382	414	276

much more frequent occurrence of these clouds in the ISCCP-D2 dataset. As noted earlier, ISCCP cumulus clouds are very thin by definition (maximum optical thickness is 3.6) and thus are likely to be of the cumulus humilis and cumulus mediocris subtypes. For these fair weather cumuli a liquid water content of 0.5 g/m^3 assumed by PJ95 might be an overestimation, and a value of 0.3 g/m^3 may be a better choice. With this latter value the global mean *LWP* of these clouds would be close to the one obtained by PJ95 even with their increased frequency as determined by ISCCP.

Sensitivity to w_c

Let us now have a look at the liquid water content values used by PJ95. A literature survey of cloud liquid water content is given in Table 4.4. It is emphasized here that these values meant to represent typical conditions only. The following general characteristics can be established. Cumulonimbus clouds are the wettest with a typical liquid water content of a few g/m^3 . The largest values of w_c can reach up to $5\text{-}8 \text{ g/m}^3$ in the updraft cores of the most severe convective systems, the volume average value, however, is likely to be more modest. Observations indicate that a liquid water content of at least 0.5 g/m^3 is required for precipitation (Cotton and Anthes, 1989). This puts a lower limit on w_c in Cb and Ns clouds. The liquid water content changes with the evolution of the convective system. Growing Cb clouds have a larger w_c value than do dissipating ones. Among Cu clouds the fair weather humilis and mediocris subtypes have lower liquid water contents than does the more vertically extent congestus subtype. Finally, the As/Ac and St/Sc categories seem to be the driest, especially the thinnest Sc clouds, which

Table 4.4 Typical values of cloud liquid water content (g/m^3) published in the literature. Minimum values are highlighted (bold, underlined).

Cloud Type	$w_{c,1}$	$w_{c,2}$	$w_{c,3}$	$w_{c,4}$	$w_{c,5}$	$w_{c,6}$	$w_{c,7}$
Cb	<u>1</u>	1.5-4.5	2.5	2.5	-	1-3	-
Ns	<u>0.4</u>	-	-	0.5	-	-	-
Cu	0.5	0.3-2.5	0.3-2	1	0.26-0.44	0.26-0.44	0.3-1
As/Ac	0.2	-	0.6	0.28	0.28-0.3	-	<u>0.15</u>
St/Sc	0.1	<u>0.05</u> -0.25	0.1-0.5	0.05-0.47	0.28-0.3	0.28-0.44	0.25

¹Pruppacher and Jaenicke (1995)

²Cotton and Anthes (1989); Cu Humilis, Mediocris: $0.3\text{--}1\text{ g/m}^3$, Cu Congestus: $0.5\text{--}2.5\text{ g/m}^3$

³Stephens (1994); fair weather Cu: 0.3 g/m^3 , Cu Congestus: 2 g/m^3 , maritime Cu: 0.5 g/m^3

⁴Lenoble (1993)

⁵Hess et al. (1998)

⁶Rosenfeld and Lensky (1998); dissipating Cb: $1\text{--}1.5\text{ g/m}^3$, growing Cb: $1\text{--}3\text{ g/m}^3$

⁷Pandey et al. (1983) after Gaut and Reifstein (1971)

Table 4.4 - *Continued*

Cloud Type	$w_{c,8}$	$w_{c,9}$	$w_{c,10}$	$w_{c,11}$	$w_{c,12}$	$w_{c,13}$
Cb	-	3.93	1.21	-	-	-
Ns	-	0.65	0.65	0.5	-	-
Cu	<u>0.2</u> -0.4	1	1	1	0.4-0.6	-
As/Ac	-	0.41	0.4	0.28	-	-
St/Sc	-	-	0.15-0.29	0.05-0.47	0.2-0.5	0.0005-1

⁸Karstens et al. (1994); Deirmandjian's drop size distributions, Cu Hum: C_1 , Cu Con: C_5

⁹Thomas and Stamnes (1999); cloud models from LOWTRAN, FASCODE

¹⁰LOWTRAN cloud models, cited in Savijärvi et al. (1997)

¹¹Slingo and Schrecker (1982) after Stephens (1979)

¹²Hegg (1986)

¹³Miles et al. (2000); mean= 0.18 g/m^3 ; median= 0.13 g/m^3 ; minimum value discarded as unrealistically low

can have liquid water contents as low as 0.05 g/m^3 . The literature survey revealed that the values used by PJ95 were generally on the lower end of the spectrum, especially for Cb and Ns. For the remaining three groups the liquid water content might be reduced by 25-60% if the smallest fair weather Cu and the thinnest stratiform clouds are taken as representative ones.

Let us now apply the published minimum liquid water contents in the liquid water path calculations. The results are given in Table 4.5, where the original cloud thicknesses were taken from Table 4.1, and the cloud amounts were taken from Table 4.2. There is no change for Cb and Ns, whereas for the remaining categories the *LWP* decreased according to the reduced w_c values. The global mean liquid water path was reduced to 323 g/m^2 , 340 g/m^2 , and 196 g/m^2 when using cloud amounts in PJ95, the Warren atlas, and the ISCCP, respectively.

Sensitivity to h_c

Finally, let us investigate the plausibility of the cloud thickness values PJ95 assigned to the individual cloud types. The vertical distribution and thickness of clouds can be determined by various techniques. De Bary and Möller (1963) presented a statistical analysis of the vertical distribution of clouds up to an altitude of 5 km based on German weather flights during the years 1936-1940. Matveev (1984) also reported a fairly extensive set of aircraft soundings of clouds, including total cloud depth, collected over the Soviet Union from 1957 to 1964. Pandey et al. (1983) explored the potential of using microwave radiometry with simultaneous IR measurements for retrieving cloud

Table 4.5 Cloud liquid water path (g/m^2) as calculated from equation (4.1) using cloud thicknesses from Table 4.1, cloud amounts from Table 4.2, and the minimum cloud liquid water values from Table 4.4.

Cloud Type	LWP_{PJ95}	LWP_{Warren}	LWP_{ISCCP}
Cb	190	197	99
Ns	64	63	23
Cu	24	33	42
As/Ac	34	33	25
St/Sc	11	14	7
Total	323	340	196

thickness over the ocean. Similar studies combining microwave and IR data to determine the vertical structure of cloudiness were conducted by Sheu et al. (1997) who used SSM/I and ISCCP observations, and by Ho et al. (2003) who used TMI and VIRS data. Finally, rawinsonde measurements of the vertical profiles of temperature and humidity can also provide information about the vertical distribution of clouds by identifying saturated levels in the atmosphere. Poore et al. (1995) created a cloud thickness climatology for the Northern Hemisphere using 14 years (1975-1988) of rawinsonde and surface observations. Their analysis was extended to a 20-year period (1976-1995) by Wang et al. (2000). Here I focused on these latter two studies because they represented the longest time series and they were the most globally representative ones.

Wang et al. (2000) classified clouds only according to the number and height (lowest, middle, highest) of the layers, but not according to their type. Their global statistics yielded a mean cloud-base height of 2.4 km, a mean cloud-top height of 4 km, and hence a mean cloud-layer thickness of 1.6 km. These values were higher than the ones determined by Poore et al. (1995), who obtained 1.6 km for cloud-base height, 2.8 km for cloud-top height, and 1.2 km for cloud thickness. If the cloud thicknesses in PJ95 (column 3 in Table 4.1) are weighted by the corresponding cloud amounts (column 2 in Table 4.1) one gets a global average cloud thickness of 1.4 km, which is right in between the previous two estimates. It is noted that while PJ95 considered the thickness of the liquid layer only, the radiosonde data also included the ice-phase. When only warm clouds (with top temperatures more than 0°C) were considered the rawinsonde-determined mean single-layer thickness reduced to about 800 m (Wang et al., 2000).

This, however, is likely to be an underestimate due to the presence of supercooled liquid at higher altitudes. In summary, the global average cloud thickness according to PJ95 did not seem to be unreasonably high or low.

Both Poore et al. (1995) and Wang et al. (2000) found that clouds are 300-500 m thicker over land than over ocean. Wang et al. (2000) pointed out that more than half of their clouds were thinner than 1 km. These were probably the St/Sc, As/Ac, and fair weather Cu types. They also noted, however, the occurrence of some very thick clouds, especially over the midlatitude continents of the Northern Hemisphere. The layer thickness was larger than 5.5 km for 5-6% of the clouds. These were most likely cumulonimbi.

The Poore et al. (1995) study was the only one that actually provided cloud thickness estimates for all the individual cloud types considered by PJ95. Their results are summarized in Table 4.6. The given values are area-weighted averages of the separate land and ocean estimates. Of the morphological types, Ns had the largest layer thickness and Cu the smallest. For the As/Ac and St/Sc categories Poore et al. (1995) estimated larger thicknesses than PJ95. This is most likely due to the probable overrepresentation of the stratiform (As, St) clouds compared to the cumuliform (Ac, Sc) clouds in these groups. Poore et al. (1995) noted the lack of coverage over the central parts of the oceans, particularly in the Tropics, which might have resulted in the undersampling of marine Sc. If it is assumed that marine Sc is the dominant cloud in the St/Sc category then both PJ95 and Poore et al. (1995) overestimated its cloud thickness. For these clouds a characteristic value of 300-400 m can be conservatively used (Blaskovic et al., 1991).

Table 4.6 Cloud layer thickness according to PJ95, and Poore et al. (1995).

Cloud Type	h_c (km)	h_c (km)	h_c (km)
	PJ95	Poore et al. (1995)	Lesser of Two
Cb	3.8	1.5	1.5
Ns	2.7	2.2	2.2
Cu	1.7	0.9	0.9
As/Ac	1.0	1.2	1.0
St/Sc	1.0	1.3	0.3 ^a

^aassuming 300 m for marine Sc

For Cu Poore et al. (1995) gave a 50% smaller thickness than PJ95. For Ns the value given by Poore et al. (1995) was only 20% smaller. For Cb, however, their value was only 40% of that of PJ95. The surprisingly small layer thickness for Cb clouds, however, is probably an artifact produced by mixing nonprecipitating but vertically developed Cu with precipitating storm clouds in the surface classification, and by the altitude limits of the RAOBS as pointed out by the authors. Due to the unreliable temperature measurements below -40°C the RAOB profiles are usually cut off at an altitude of 10.6 km. In addition, the relatively small size of and the generally violent motions in Cb also contribute to the unreliability of the rawinsonde thickness estimates for these clouds. Poore et al. (1995) reported an average Cb cloud top height of 3 km over land and 2 km over ocean. These apparently erroneous values can be contrasted with the mean cloud top temperature and mean cloud top pressure determined for deep convective clouds by the ISCCP. Rossow and Schiffer (1999) obtained respective averages of 234.8 K and 326 mb, which correspond to an altitude of ~ 8.4 km assuming a standard atmospheric profile. A better estimate of Cb thickness might be calculated using only the cloud-base height from Poore et al. (1995) with an estimate on the height of the freezing level or the -10°C isobar if one is to account for supercooled droplets. Poore et al. (1995) computed a global mean Cb cloud-base height of about 800 m. The height of the freezing level is about 3-4 km at midlatitudes and 5-6 km in the Tropics (Wentz and Spencer, 1998), where most of these severe storms occur. A standard atmosphere gives a characteristic height of ~ 4 km for the -10°C isobar. Therefore, the thickness of a typical Cb can easily reach 3-4 km. In summary, PJ95's estimate of Cb thickness seemed reasonable considering published

global averages of cloud-base height, cloud-top temperature, and freezing-level height for deep convective systems. Nevertheless, *LWP* calculations were made both for the values of Poore et al. (1995) and for the most conservative case when the lesser of PJ95 and Poore et al. (1995) along with a value of 300 m for Sc was used (column 4 in Table 4.6).

The resulting *LWP* is given in Table 4.7. Here, the cloud amounts were taken from Table 4.2, and the minimum liquid water contents were taken from Table 4.4. These *LWP* values constitute the most conservative estimates. The *LWP* for St/Sc was calculated to be a few g/m^2 , which seems unreasonably small. This is most likely because the lowest published water content of $0.05 g/m^3$, which was used here, is not globally representative of these clouds. For these low, warm, nonprecipitating clouds the microwave retrievals are generally reliable and yield a typical liquid water path of about $90\text{--}100 g/m^2$ (Greenwald et al., 1993). This translates to a typical water content of $\sim 0.3 g/m^3$ if a characteristic thickness of ~ 300 m is assumed. Table 4.2 indicates a global St/Sc amount of 15% to 30%. Therefore, the contribution of these clouds to the global mean atmospheric liquid water path is more likely to be around $15\text{--}30 g/m^2$ that is an order of magnitude larger than the minimum estimate given in Table 4.7. Nevertheless, Table 4.7 can be interpreted as the worst-case scenario. Thus, the absolute minimum global average atmospheric liquid water path was found to be $176 g/m^2$, $183 g/m^2$, and $106 g/m^2$ when using cloud amounts in PJ95, the Warren atlas, and the ISCCP, respectively.

Table 4.7 Cloud liquid water path (g/m^2) as calculated from equation (4.1) using cloud amounts from Table 4.2, the minimum cloud liquid water values from Table 4.4, and the minimum cloud thicknesses (column 4) from Table 4.6.

Cloud Type	LWP_{PJ95}	LWP_{Warren}	LWP_{ISCCP}
Cb	75	78	39
Ns	52	51	18
Cu	12	17	22
As/Ac	$34^a/41^b$	$33^a/39^b$	$25^a/30^b$
St/Sc	$3^a/14^b$	$4^a/18^b$	$2^a/9^b$
Total	$176^a/194^b$	$183^a/203^b$	$106^a/118^b$

^ausing “minimum” thickness

^busing Poore et al. (1995)

Best guess LWP estimate

Finally, having considered the uncertainties in the input parameters in equation (4.1) I try to give a best guess estimate of the global mean atmospheric *LWP*. For cloud amount I used the values given by PJ95 since they were in between the values given by the Warren atlas and the ISCCP. For cloud liquid water content the PJ95 values also seemed to be very reasonable estimates. Specifically, for Cb and Ns the PJ95 values were at the lower end of published data. For Cu, As/Ac, and St/Sc they were very close to the median values of all the published data listed in Table 4.4. For St/Sc Miles et al. (2000) compiled a very comprehensive data set containing all available in-situ measurements of liquid water content. The median of this data set was 0.13 g/m^3 and the mean was 0.18 g/m^3 . Unfortunately, there were no such published compilations for the other cloud types, therefore I had to rely in my own literature search summarized in Table 4.4. In the end, I used PJ95's water contents for all clouds with the exception of St/Sc for which I used the median value of the Miles et al. (2000) data set. For cloud thickness I used the arithmetic mean of the values given by PJ95 and Poore et al. (1995) for all clouds but St/Sc. For this last group I used the canonical value of 300 m frequently cited in the literature. The best guess parameter values and the resulting *LWP* are given in Table 4.8. My best guess global mean atmospheric *LWP* was 296 g/m^2 that was somewhat lower than PJ95's original value.

Table 4.8 Best guess values for cloud amount, cloud thickness, and cloud liquid water content and the resulting cloud liquid water paths.

Cloud Type	c_c (%)	h_c (km)	w_c (g/m ³)	LWP (g/m ²)
Cb	5	2.65	1.0	132
Ns	6	2.45	0.4	59
Cu	7	1.3	0.5	45
As/Ac	23	1.1	0.2	51
St/Sc	23	0.3	0.13	9
Total	N/A	N/A	N/A	296

Summary

In this chapter I tried to put an uncertainty range on the original estimates of PJ95 that did not include error bars. The uncertainties in cloud-type amount, cloud thickness, and cloud liquid water content, which constituted the input parameters in equation (4.1), were estimated from published data on these quantities. Taking into account the possible range of cloud amounts, as determined from the Warren atlas and the ISCCP, gave a range of 276-414 g/m^2 for the global average atmospheric *LWP*. This range was reduced to 196-340 g/m^2 when the lowest published liquid water contents were also used. Finally, the lowest values of 106-183 g/m^2 were obtained when the smallest cloud thicknesses were used from Poore et al. (1995) and PJ95.

In general, the ISCCP cloud amounts resulted in the lowest *LWP* estimates and the values from the Warren atlas yielded the highest ones, with those obtained with PJ95 being in between. This was primarily determined by the varying amounts of the wettest Cb, Ns, and Cu clouds. St/Sc clouds tended to be the driest and thus contributed little to the global mean. Their average *LWP*, though, was likely to be underestimated by an order of magnitude in my worst-case calculations. The most conservative calculation, that is when the smallest cloud amounts, thinnest clouds, and lowest water densities were used, yielded an absolute minimum value of 106 g/m^2 for the global mean atmospheric *LWP*. Because the total cloud cover of the liquid cloud types considered here was around 50% this corresponded to a global mean cloud *LWP* of about 220 g/m^2 . It is emphasized here that this lower limit is still a factor of two larger than the global average value of 113 g/m^2 determined from microwave measurements (Greenwald et al., 1995) and it is 3-4

times larger than the value of 65 g/m^2 obtained from visible reflectance data (Rossow and Schiffer, 1999). Considering the lowest possible values of all input parameters, however, was unlikely to produce the most reasonable global estimate. Using more realistic, intermediate values of the input parameters yielded a best guess of about 300 g/m^2 for the global mean atmospheric *LWP*.

4.2 Angular Consistency Study

With the help of the multiangle dataset the validity of the plane-parallel radiative transfer theory could be evaluated. For every pixel, a set of 9 angular optical thicknesses was retrieved. The consistency or inconsistency of these angular values was indicative of the success or failure of the plane-parallel method. This study has already been published in Horváth and Davies (2004). Here only the main findings are summarized, the actual paper can be found in Appendix E.

The vast majority of maritime liquid water clouds failed a simple 1D angular test at the $\pm 5\%$ level in radiance. Only maybe 20% of global cloudiness passed the angular test and could be amenable to analysis by 1D theory with higher confidence. It was also found that clouds appeared apparently more plane-parallel at larger scales. This, however, does not imply that cloud optical thickness retrieved at coarser resolutions is unbiased.

4.3 Comparison of the Optical and Microwave Techniques

In this section the optical and microwave *LWP* retrieval techniques are compared. The optical technique used cloud optical thickness as determined by MISR (see Chapter 3) and converted it to *LWP* using the parameterization based on the large drop limit (equation (2.6)). The microwave observations were made by SSM/I and TMI. The SSM/I instruments are carried on board the DMSP platforms that are in a near-polar, sun-synchronous orbit. The particular satellites used in this study were F-13, F-14, and F-15 with respective descending node equator crossing times of approximately 6:15 AM, 8:21 AM, and 9:31 AM. The TMI is on board the TRMM satellite. TRMM is in a semi-

equatorial orbit that produces data collected at changing local times for any given earth location between 40°S and 40°N. For both microwave instruments the same algorithms were used to derive geophysical parameters, such as cloud liquid water path, and precipitation rate (Wentz, 1997; Wentz and Spencer, 1998). The daily data were given on a 0.25-degree (25 km) grid and were obtained from Remote Sensing Systems (<http://www.remss.com>).

The comparison was made for MISR orbits 6956-6969, which were collected on April 9, 2001. Two types of comparisons were made. First, two case studies were conducted, one for a non-precipitating and one for a precipitating cloud scene. TRMM data were used for this purpose in order to get time synchronization better than 30 minutes between the optical and microwave observations. The TRMM cloud liquid water paths and rain rates were remapped to the corresponding MISR blocks using the algorithm outlined in Appendix F. The coincident measurements were from the MISR block range 80-90, which corresponded to the latitude range 13°N-0°N. Second, the global mean cloud liquid water paths as determined by MISR and SSM/I were compared. The time difference between MISR and SSM/I was 1-4 hours, depending on the particular DMSP satellite.

Non-precipitating case

Figure 4.1 shows the comparison between TMI *LWP* and MISR *LWP* for block 82 of orbit 6965 (11°N, 76°W). The time difference between the two instruments was only ~4 minutes. Because TMI data were given at a scale of ~25 km, whereas MISR retrievals

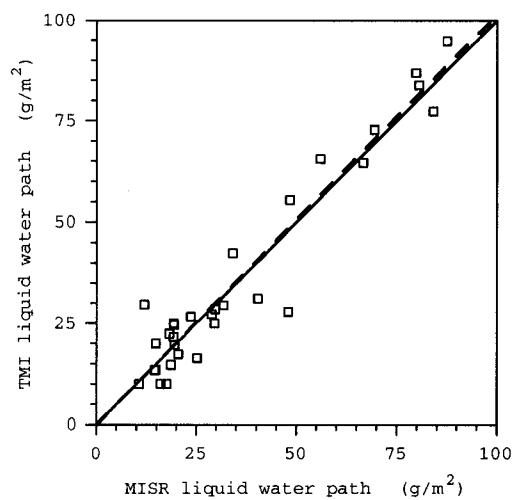


Figure 4.1 Comparison of MISR *LWP* and TMI *LWP* for a non-precipitating marine Sc field. Data were from block 82 of orbit 6965 (11°N, 76°W). The red solid line corresponds to a one-to-one relationship, and the blue dashed line is a linear fit to the data.

were obtained at a resolution of 275 m, both data sets were first resampled and averaged at a scale of 35.2 km (i.e. 128 MISR pixels). In order to minimize the effect of sun glint, areas with optical thickness less than 3 were excluded. The MISR results were obtained by converting the nadir optical thickness to *LWP* using equation (2.6). The optical thicknesses were retrieved using a phase function corresponding to an effective radius of 8 μm . Visible reflectance (optical thickness) is sensitive to the ratio of *LWP* to effective radius, which means that the effective radius basically acts as a degree of freedom when converting visible optical thickness to *LWP*. An effective radius of 7 μm was used in the optical thickness-*LWP* conversion because this yielded the best agreement between TMI and MISR. This particular block contained a marine Sc field, for which TMI data indicated no rain or drizzle. The *LWP* values were below 100 g/m^2 corresponding to an optical thickness range of 2 to about 20. In general, the agreement between TMI and MISR was fairly good, the data points scattered around the one-to-one line (solid). A linear fit to the data (dashed line) also indicated a strong correspondence between the two techniques. The block average liquid water path was 54 g/m^2 for TMI and 53 g/m^2 for MISR.

Precipitating case

Figure 4.2 shows the MISR nadir optical thickness (panel a), the TMI *LWP* (panel b), and the TMI rain rate (panel c) for block 84 of orbit 6967 (8°N, 126°W). The time difference between MISR and TMI was ~15 minutes. This block contained two large convective systems in the top left and bottom right corners. The visible optical thickness

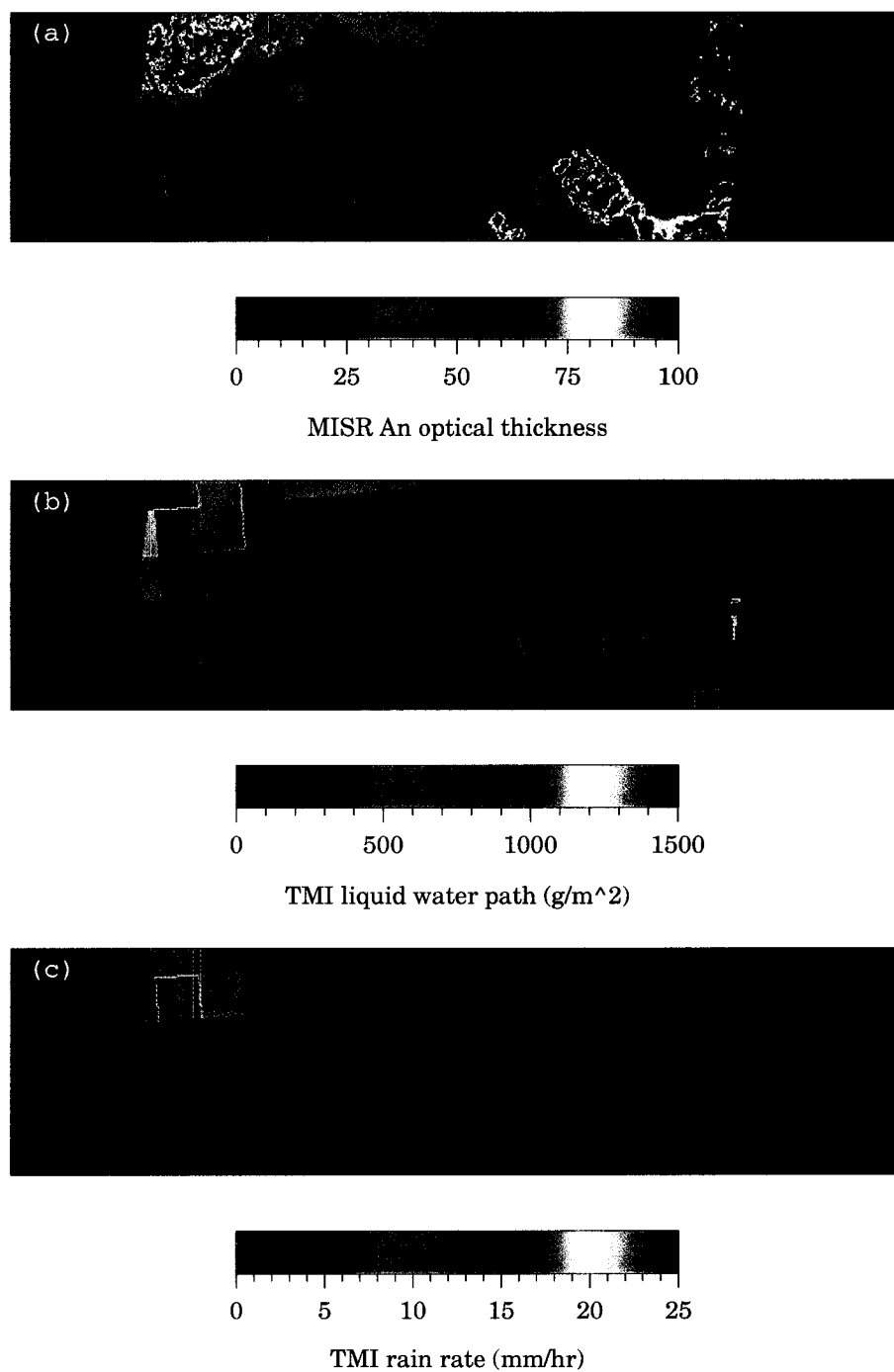


Figure 4.2 (a) MISR nadir optical thickness, (b) TMI liquid water path, and (c) TMI rain rate for a precipitating Cb field. Data were from block 84 of orbit 6967 (8°N , 126°W).

saturated for both of them. The TMI data revealed that the top left cloud was generally wetter than the bottom right cloud with a maximum LWP of 1650 g/m^2 as opposed to 1350 g/m^2 . It is noted here that the optical thickness was retrieved using a liquid phase function even though the MODIS phase mask indicated ice at cloud top for most of the block. This might have resulted in slightly overestimated optical thickness values, especially for the thinner cloud areas. TMI indicated the presence of rain for both systems. The cloud in the top left corner had moderate to heavy precipitation rates with a maximum of 23 mm/hr . The one in the bottom right corner had less intensive, light to moderate rain with a maximum rate of 14 mm/hr .

The comparison between the microwave and optical LWP values is shown in Figure 4.3. As before, the thinnest regions with optical thickness below 3 were excluded to minimize the effect of sun glint. Panel a shows the results obtained using a fixed effective radius of $8 \mu\text{m}$ in the conversion of MISR optical thickness to LWP . The optical LWP values clearly underestimated the microwave ones by a factor of 2 to 3. The block average LWP was 313 g/m^2 for TMI and only 134 g/m^2 for MISR. The likely reason for this large discrepancy is that the assumed drop size distribution was inadequate for this cloud field. The visible optical thicknesses were retrieved using a phase function corresponding to a gamma drop size distribution with an effective radius of $8 \mu\text{m}$. This value may be representative of stratus, and stratocumulus clouds, however, it most likely underestimates the drop effective radius in cumulus, and cumulonimbus clouds.

Not only is the effective radius much larger in extensive convective clouds, it is also likely to depend on the precipitation rate. Savijärvi et al. (1997) derived a first

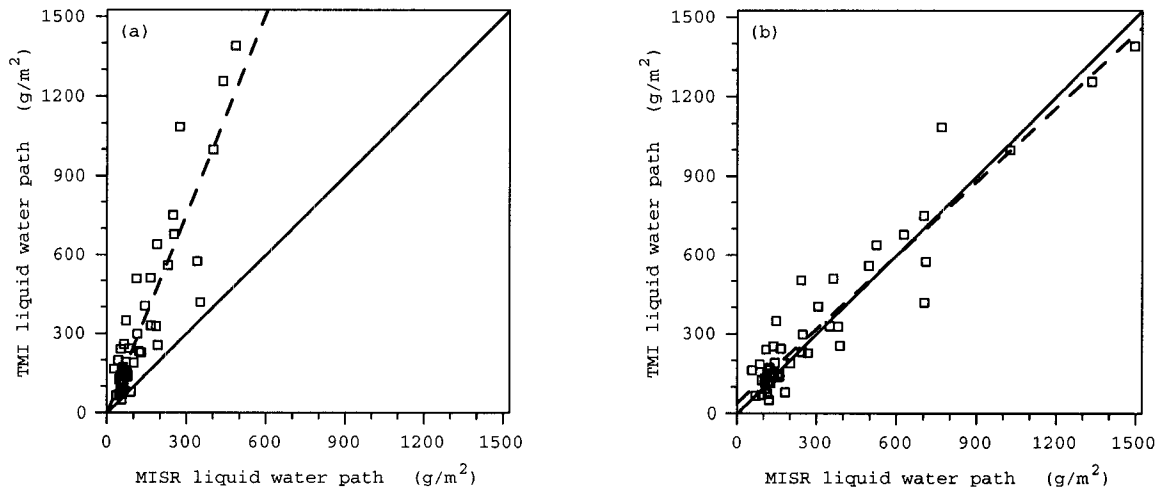


Figure 4.3 Comparison of MISR *LWP* and TMI *LWP* for the precipitating Cb field shown in Figure 4.2. (a) Using a fixed effective radius of $R_e = 8 \mu\text{m}$, and (b) using the parameterization in equation (4.2).

approximation of effective radius in precipitating water clouds by adding typical raindrop size distributions to stratus- and cumulonimbus-type cloud-drop distributions. For Cb clouds they obtained the following simple parameterization:

$$R_e = R_{Cb} + 0.6R, \quad (4.2)$$

where R_{Cb} is the effective radius of the Cb drop size distribution, and R is the rain rate in mm/hr. Here equation (4.2) was used with $R_{Cb} \approx 15 \mu\text{m}$, which was the approximate value for the LOWTRAN Cb drop size distribution, and with a rain rate factor of 0.5 instead of 0.6, because this gave slightly better results. With the rain rates shown in Figure 4.2c this parameterization resulted in effective radius values between $15 \mu\text{m}$ and $26 \mu\text{m}$. Figure 4.3b shows the comparison between TMI *LWP* and MISR *LWP* using the modified effective radii. The agreement between the optical and microwave techniques was much better compared to the previous case with a fixed effective radius of $8 \mu\text{m}$. The linear fit to the data (dashed line) was close to the one-to-one line. The block average liquid water path values were also in agreement with 313 g/m^2 for TMI and 307 g/m^2 for MISR.

Global comparison

In addition to the case studies the global mean cloud liquid water path values as determined by SSM/I, TMI, and MISR were also compared. The global averages are

given in Table 4.9. Note that the SSM/I values corresponded to a particular local time while the TMI value was obtained by averaging data collected at various local times due to the semi-equatorial orbit of TRMM. The time difference between SSM/I and MISR was approximately 4 hours for F-13, 2 hours for F-14, and 1 hour for F-15, therefore this latter was closest in time to MISR's 10:30 AM orbit. For SSM/I and TMI only the morning node data were used. It is also noted here that SSM/I and TMI had better spatial coverage than MISR for which there were large data gaps between consecutive orbits. However, there was only a slight change in the results when only those areas were considered where SSM/I, TMI and MISR overlapped. For MISR, optical thickness was retrieved not only over liquid clouds but over ice clouds as well. Ice optical thicknesses were reduced by ~30% to account for the use of a liquid phase function (Rossow and Schiffer, 1999). The thinnest clouds below an optical thickness of 3 were excluded. To approximate this cloud filtering in the microwave data pixels with a *LWP* value less than 20 g/m^2 were eliminated.

The microwave results varied from 100 g/m^2 to 111 g/m^2 . The higher value obtained by the F-13 SSM/I might have been due to diurnal cycle effects since the satellite had an early morning orbit. The higher value determined by TMI might have been due to the instrument's limited sampling between 40°S - 40°N , which preferred the more convectively active and wetter equatorial regions. The global mean cloud optical thickness was about 15 for the MISR nadir camera. Using this value with an uncertainty range of $8\text{-}12 \text{ }\mu\text{m}$ for the effective radius of the mostly boundary layer clouds of the dataset yielded an *LWP* range of $80\text{-}120 \text{ g/m}^2$. The global mean *LWP* of 100 g/m^2 that

Table 4.9 Global average cloud liquid water path (g/m^2) as determined by various instruments for April 9, 2001.

F-13 SSM/I	F-14 SSM/I	F-15 SSM/I	TMI	MISR
111	102	100	108	80-120

was determined by the SSM/I closest in time to MISR (F-15) was right in the middle of this range. Therefore, it was concluded that the optical and microwave techniques were in fair agreement for the global mean value at around 10:30 AM.

Summary

In this section the microwave and optical techniques to retrieve *LWP* were compared. It was found that for relatively thin clouds, such as fair weather cumulus, and marine stratocumulus, the two methods gave comparable results. For thicker clouds, especially for extensive convective clouds, however, the optical technique very clearly underestimated the *LWP* compared to the microwave technique. When only the global mean *LWP* of clouds was considered the two methods gave consistent results within the estimated uncertainties. This highlighted the fact that only a small portion of MISR's early morning (10:30 AM) orbit contained the thickest convective type clouds.

The optical technique as most commonly applied has serious limitations. In the large drop limit the *LWP* is determined as the product of the visible optical thickness and the effective radius of the drop size distribution. If visible channel measurements are available only (e.g. ISCCP) then there is no information on the effective radius, which requires the assumption of a fixed drop size distribution for all clouds. Common practice is to use an effective radius of 8-10 μm . This value might be appropriate for the thinner stratus and stratocumulus clouds but is definitely an underestimate for the thicker nimbostratus and convective clouds, especially if rain is present. Not only is the base value of the effective radius much larger in these thicker clouds but also its actual value is

likely to increase somewhat proportionally to the precipitation rate, as pointed out by Savijärvi et al. (1997). For moderate to heavy rain (10-25 mm/hr) the effective radius can easily reach values of 20-40 μm . For the heaviest rainstorms even larger values can be found. Wiscombe et al. (1984) obtained values as high as 55 μm using a rising-parcel model of cloud microphysics. Hegg (1986) noted that he and other investigators frequently measured effective radii of several hundred microns even in non-precipitating clouds. Therefore, the assumption of a fixed effective radius of 8-10 μm can easily result in an underestimation of a factor 2-10 in *LWP* for these clouds.

Absorption channel measurements can yield information on drop effective radius. These methods, however, preferentially sample the upper portions of clouds and not the regions where the large liquid drops are most frequent. They are further plagued by the presence of ice crystals at cloud top. In this case the resulting effective radius can be quite large, however, the cloud is most likely to be classified as ice. Clouds with icy tops are in practice assumed to contain only ice and no liquid. Therefore, for these clouds the quantity determined from the visible optical thickness and effective radius is ice water path rather than liquid water path. The saturation of the visible optical thickness poses an additional problem. Cloud optical thickness retrievals are usually truncated at a value of ~ 100 . With the assumption of a fixed effective radius of 8-10 μm this puts an upper limit of $\sim 600 \text{ g/m}^2$ on the maximum *LWP* that can be retrieved with the optical technique.

In summary, the saturation of the visible optical thickness and the difficulty in retrieving the effective radii corresponding to liquid drop size distributions with a large drop mode severely limit the maximum *LWP* that can be determined by the optical

method. In addition, part of the liquid water might be misclassified as ice water. Consequently, global *LWP* estimates based on the optical technique are likely to be biased low. It seems unlikely to get around the saturation problem with visible reflectance measurements. A better parameterization of the effective radius that depends on cloud type and rain rate, however, may go a long way to reduce the low bias caused by the assumption of a small constant effective radius.

4.4 Global Optical Thickness Distributions

The histogram and cumulative histogram of the nadir (A_n) optical thickness for the 28 processed orbits are shown in Figure 4.4a and Figure 4.4b, respectively. Here it is noted again that optical thickness retrievals were performed over the range 1 to 100 using a liquid only phase function. The optical thickness for pixels with $\tau < 1$ was set to zero, while retrievals above the upper cut-off value of 100 were set to $\tau = 101$. A cloud mask was not employed, and thus retrievals were performed for all (clear and cloudy) pixels. The black curves show the results for pixels for which the MODIS phase mask did not indicate the presence of ice or mixed-phase clouds. Therefore, these pixels were either clear or had water clouds. They constituted 75% of all retrievals. About 49% of these retrievals were below 1, and around 0.7% of them were saturated (i.e. >100). The average optical thickness for these pixels was 5.8. The blue curves show results for pixels for which the MODIS phase mask indicated ice or mixed-phase clouds. They represented 25% of the data. The interpretation of optical thickness for these pixels is rather ambiguous. The main problem is that some of these cases represent atmospheric columns that contain only ice, while others contain both ice and liquid. Therefore, using either a liquid or an ice phase function inevitably results in errors. It is well known that over the scattering angle range encountered by satellites the use of a water-drop phase function for pure ice clouds overestimates the optical thickness because liquid phase functions produce significantly smaller reflectances than ice-crystal phase functions for a given optical thickness. For instance, Minnis et al. (1993a, 1993b) found that the overestimation can be as high as 70% for thin ($\tau < 6$) cirrus. Rossow and Schiffer (1999) concluded

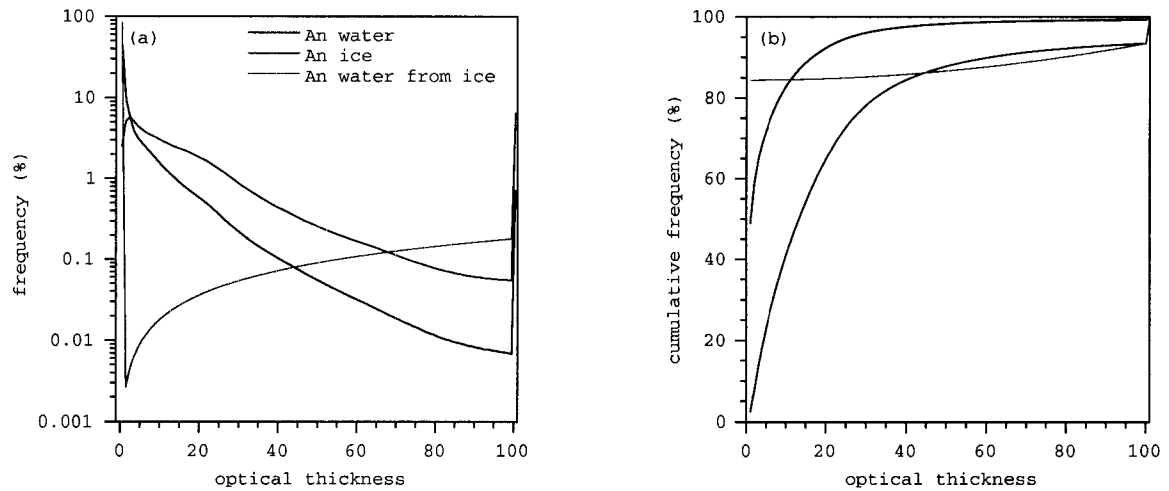


Figure 4.4 (a) Histograms, and (b) cumulative histograms of nadir (An) optical thicknesses for the 28 MISR orbits. Black curves correspond to water clouds, blue curves correspond to ice/mixed-phase clouds, and red curves correspond to the estimated liquid water component of ice/mixed-phase clouds.

from ISCCP data that globally, cirrus and cirrostratus optical thicknesses were overestimated by about 50% due to an inadequate liquid phase function. For these pure ice clouds the bias in the optical thickness may be adequately removed by using a fractal polycrystal microphysical model (e.g. Macke et al., 1996). However, it is not quite clear how to treat mixed phase clouds properly. Since they contain both liquid and ice, use of an ice only phase function seems just as inadequate as that of a liquid only phase function. This problem seems to be similar to the difficulty of separating the rain component from the cloud component in the microwave retrievals. The scattered visible signal (reflectance) comes from both liquid drops and ice crystals. It seems unlikely that the optical thicknesses corresponding to the liquid and ice components of such a cloud can be separated out from this combined signal, especially with only a single reflectance measurement. Therefore, it is necessary to make some assumptions regarding this issue. In the ISCCP cloud classification scheme cirrus and cirrostratus clouds can have a maximum optical thickness of 23. Minnis et al. (1993b) reported cirrus optical thicknesses as large as 30. Therefore, it was assumed that optical thicknesses below 40 that were retrieved for clouds labeled as ice/mixed phase correspond to cirrus and cirrostratus and thus do not contain a liquid component. The threshold 40 was used to allow for a 50% overestimation due to the liquid phase function used in this study. Ice clouds with $\tau > 40$ were assumed to contain increasing amounts of liquid water as the optical thickness increased. Most importantly, it was assumed that those ice pixels that were saturated contained a liquid component that was also saturated. Ice optical thicknesses between 40 and 100 were redistributed with linearly increasing probability

over the range 1-100. The liquid component of ice/mixed phase optical thicknesses estimated this way is shown in red in Figure 4.4. Almost 85% of ice pixels fell into the relatively thin category and thus had no liquid component. About 6.6% of them, however, contained a saturated liquid component. Finally, a weighted combination of the water cloud retrievals (black) and the (crudely) estimated liquid part of the ice cloud retrievals (red) was computed to obtain global liquid optical thickness distributions. These combination distributions are shown in Figure 4.5 (green curve). The probability of an optical thickness less than 1 in the combined data increased to 58% from the previous 49%, but the percentage of saturated pixels also increased from 0.7% to 2.2%. The mean optical thickness corresponding to the combined truncated data increased from 5.8 to 7.5.

Uncertainty in 1D optical thickness retrievals

The angular consistency analysis described in section 4.2 and Appendix E revealed that the plane-parallel model was consistent with observations to 5% (relative BRF error) maybe 20% of the time. So, for the majority of clouds the 1D optical thickness retrievals contained potentially large errors. For each pixel a set of 9 optical thicknesses was determined. In order to estimate the uncertainty in the single angle (nadir) retrievals the minimum and the maximum values of these 9 values were used as lower and upper error bounds. Thus, it was assumed that the true cloud optical thickness was somewhere in between the minimum and the maximum of the 9 angular values. The uncertainties in the 1D retrievals determined this way were likely to be underestimates. Conceptually, the main problem with this approach is that plane-parallel theory was used

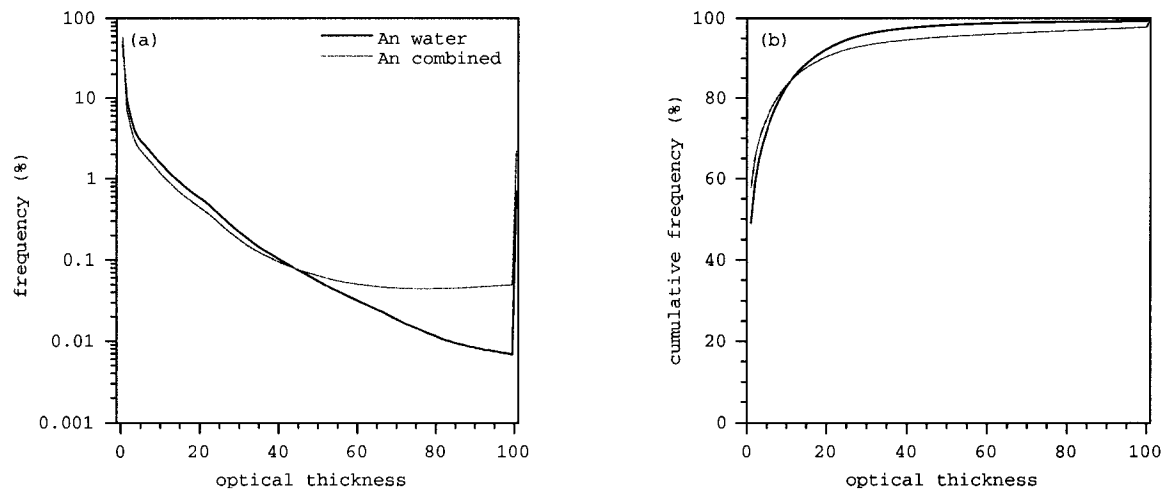


Figure 4.5 (a) Histograms, and (b) cumulative histograms of nadir (A_n) optical thicknesses for water clouds (black), and for the combination of water clouds and the water component of ice/mixed-phase clouds (green). The green curves represent the sum of the black and red curves in Figure 4.4.

to estimate its own uncertainty. Currently, there exist no standard methods to estimate the retrieval errors introduced by the 3D nature of clouds. Pending the availability of such methods the above error estimates will be used in what follows. The cumulative distributions corresponding to the minimum and maximum optical thickness values are shown in Figure 4.6 along with the nadir value. All of these distributions were corrected to include the ice retrievals as described previously.

Estimates of maximum possible visible optical thickness

In order to extrapolate the truncated optical thickness distributions above the cut-off threshold of $\tau = 100$ one needs to estimate the maximum possible cloud optical thickness. Lin and Rossow (1997) found extreme values of total (rain plus cloud) *LWP* about $10,000 \text{ g/m}^2$ in SSM/I data. Such high values of total *LWP* were also observed for the heaviest precipitating clouds by Liu and Curry (1993); they too used SSM/I measurements. Both of these studies assumed that the vast majority of the total *LWP* was due to rain and used only a small fixed cloud component of $250\text{-}500 \text{ g/m}^2$. This small cloud component was the result of using the Kessler and Atlas (1959) model with the modification that it contains only ice above 0° , which seems to be a poor hypothesis for Cb. Models used in the Russian literature, on the other hand, assumed that the cloud *LWP* was always greater than the rain *LWP* below it. Lovejoy and Austin (1980) reported cloud *LWP* values obtained from the models of Stepanenko (1968) and Kalashnikov and Frolov (1971) (see their Table 1). The cloud *LWP* generally increased with rain rate and reached maximum values of $7000\text{-}10,000 \text{ g/m}^2$. These Russian models were verified

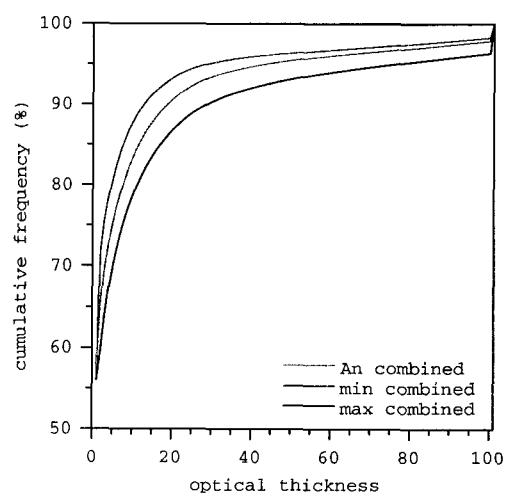


Figure 4.6 Cumulative histograms of the nadir (green), and the minimum (red) and maximum (blue) optical thicknesses for the 28 MISR orbits.

experimentally, at least for rain rates <7 mm/h, by Gorelik and Kalashnikov (1971), who used a complete suit of distrometers, cloud radars, radiosondes, and a two-channel radiometer to obtain instantaneous measurements of cloud *LWP*, rain *LWP*, and rain-layer height. In the cumulus model simulation of Mugnai and Smith (1988) the cloud *LWP* reached a maximum value of 3700 g/m^2 . Panegrossi et al. (1998) used explicit cloud microphysical simulations to improve the accuracy of SSM/I retrievals over an intensive Caribbean hurricane. They obtained a maximum cloud *LWP* of 2300 g/m^2 at a rain rate of 23.7 mm/h .

As shown above, estimates of the maximum cloud *LWP* scatter over a wide range from maybe 2500 g/m^2 to $10,000 \text{ g/m}^2$. This latter value is most likely to be unrealistic. The more sophisticated cloud models with explicit microphysics can produce *LWP* as high as 3700 g/m^2 for the small drop ($r < 100 \text{ }\mu\text{m}$) mode. Therefore, it was concluded that a maximum cloud *LWP* value of 5000 g/m^2 is not unreasonably high. This value was used as our best guess, nevertheless calculations were also made for the lower and higher limits of the published maximum cloud *LWP* range. It was also assumed that these wettest clouds had a broader drop size distribution with an effective radius of $r_e = 16 \text{ }\mu\text{m}$ (LOWTRAN Cb model), rather than the commonly used drop distributions with characteristic effective radii of $8\text{-}10 \text{ }\mu\text{m}$. This assumption was partly based on the comparison between the optical and microwave techniques (see section 4.3), which indicated that for Cb clouds the drop effective radius had to be increased by at least a factor of two in order to get agreement between the two methods. With this the maximum

cloud optical thickness was determined to be about 235, 470, and 940 corresponding to a maximum cloud *LWP* of 2500 g/m², 5000 g/m², and 10,000 g/m² respectively.

Estimates of global mean atmospheric LWP

The truncated minimum, maximum, and single angle (A_n) optical thickness cumulative distributions were extended above the cut-off value of 100 up to the maximum assumed cloud optical thickness. The obtained optical thickness distributions then were converted back to *LWP* using the geometric optics parameterization (equation (2.6)) with the assumption that the effective radius was 10 μm below the cut-off optical thickness and 16 μm above it. This assumption did not have a significant effect on the results to follow. Calculations made using a fixed effective drop radius of 10 μm for all clouds produced the same results. The reason for this was that this smaller effective radius resulted in a larger maximum optical thickness. Since *LWP* is proportional to the product of effective radius and optical thickness, a decrease in the former was practically compensated by an increase in the latter.

A large number of fitting functions was tested to interpolate between the cut-off optical thickness and the assumed maximum optical thickness. In general, spline and sigmoidal models provided the best fits. Spline fits worked well regardless of whether the independent variable was given on a linear or a logarithmic scale. However, the results depended on the amount of tension applied to the fitting curve. Large tension resulted in an effectively linear interpolation between the cut-off and the maximum optical thickness, and represented an upper limiting value on the global mean *LWP*. The best

overall fits were obtained with sigmoidal models when the optical thickness was given on a logarithmic scale. In this case the cumulative distribution function assumed an S-shaped growth curve. The following sigmoidal functions were considered: Gompertz, logistic, Richards, MMF, and Weibull. The fitting errors were smallest for the Morgan-Mercer-Flodin (MMF) function (Morgan et al., 1975):

$$CDF = \frac{ab + cx^d}{b + x^d}, \quad (4.3)$$

where CDF is the cumulative distribution function, a , b , c , d are parameters, and $x = \log_{10} \tau$ is the logarithm of the optical thickness. The parameter a is the intercept when $x = 0$, c is the value to which the curve asymptotes as $x \rightarrow \infty$, d is a shape coefficient, and $b = (x_{50})^d$ where x_{50} is the value of x for which $CDF = 50\%$.

The resulting global mean atmospheric LWP values are listed in Table 4.10. For the linear spline fits the maximum optical thickness could be fixed at the specified τ_{\max} value. For the sigmoidal (MMF) models, however, the maximum optical thickness, that is the point where $CDF = 100\%$, varied. For the maximum curve this point was close to the best guess value of $\tau_{\max} = 470$, the minimum and nadir curves, however, reached $CDF = 100\%$ at significantly smaller optical thicknesses. The sigmoidal fits to the cumulative distributions are plotted in Figure 4.7. The results in Table 4.10 had a slight dependence on the value of the cut-off optical thickness. For example, if the maximum distribution was truncated at an optical thickness of 70 instead of 100, the global mean

Table 4.10 Global mean atmospheric liquid water path (g/m^2) estimates based on extrapolating the truncated optical thickness distributions.

τ_{max}	Fitting Model	Min	An	Max
940	linear spline	125	158	249
470	linear spline	82	104	157
235	linear spline	61	76	111
varying	sigmoidal	67 ^a	77 ^b	131 ^c

^a $\tau_{\text{max}} = 384$

^b $\tau_{\text{max}} = 278$

^c $\tau_{\text{max}} = 462$

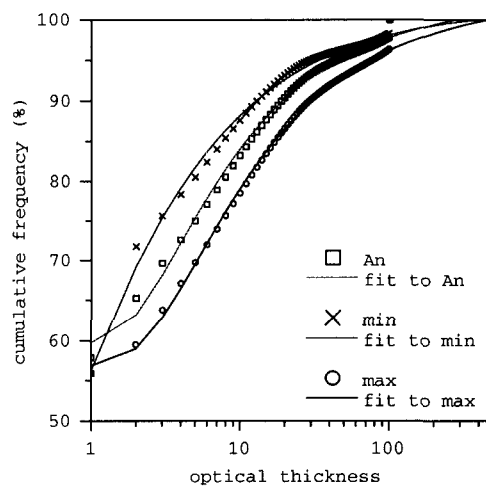


Figure 4.7 Extrapolated cumulative histograms of the nadir, the minimum, and the maximum optical thicknesses. The squares, crosses, and circles correspond to the truncated MISR retrievals, while the green, red, and blue lines indicate the respective sigmoidal fits.

LWP obtained with the sigmoidal model decreased to 126 g/m^2 from 131 g/m^2 . In summary, the results indicated that the best guess value of the global mean *LWP* obtained from satellite measurements over the ocean could be as high as $\sim 150 \text{ g/m}^2$. This was still a factor of ~ 2 smaller than the theoretical estimate.

CHAPTER 5 SUMMARY AND CONCLUSIONS

This dissertation investigated the differences between satellite measurements and theoretical estimates of global cloud liquid water amounts. The study was prompted by the large variation in published estimates of global mean cloud liquid water path indicating a significant uncertainty in this quantity. The largest differences occur between theoretical estimates based on cloud microphysics and satellite observations, although results from various satellite techniques also show significant variation. At the low end of the estimate range is the ISCCP's result of 25 g/m^2 obtained from cloud optical thickness measurements, while at the high end is the theoretical value of 382 g/m^2 calculated by Pruppacher and Jaenicke (1995) from cloud microphysical considerations. Space-borne microwave measurements usually give intermediate values ($60\text{-}80 \text{ g/m}^2$) that are somewhat higher than ISCCP but still much lower than the theoretical estimates.

It was found that the scatter among the satellite measurements could be partly attributed to the inconsistent use of the term *liquid water path*. Some authors included contributions from ice particles and/or raindrops in their definition of this quantity whereas others considered only liquid cloud droplets. An additional source of ambiguity was the varying definitions of a "cloud" in satellite data. Cloudy pixels were usually identified by putting a certain threshold on the measured quantity (e.g. visible reflectance, microwave brightness temperature, etc.). This made the value of cloud liquid water path dependent on this threshold. To avoid this difficulty it is suggested here that all retrievals, that is both clear and cloudy pixels, should be included in the calculations. This results in a quantity that is normalized to the entire surface area of the earth as opposed to the

fraction covered by liquid clouds. This so-called *atmospheric liquid water path (ALWP)* is better suited for comparisons.

The definition of a cloud is rather ambiguous and arbitrary in terms of the drop size distribution as well. Traditionally, the limiting radius of cloud droplets is assumed to be 100 μm . This is often the range of validity of microwave techniques that use Rayleigh theory to derive extinction coefficients. In-situ observations and optical retrieval techniques, however, usually consider a narrower range of drop sizes. In-situ measurements of cloud liquid water density employ hot-wire probes or the FSSP instrument whose detection range is mostly below 30 μm but usually no more than 50 μm in radius. The retrieval of cloud optical thickness from visible reflectances also assumes drop size distributions that usually do not extend above a radius of 30 μm . Therefore, there is a drop radius range from 30 μm or 50 μm to 100 μm that is traditionally considered as cloud but that is not sampled or measured by certain techniques. Drops within this radius range may contain significant amounts of liquid water especially in precipitating clouds that are often characterized by broad and bimodal drop size distributions.

In summary, it is important to use the same definition of liquid water path in terms of hydrometeor type, drop size, and normalization factor when comparing different techniques. The inconsistent use of this quantity contributed to the observed variation in satellite measurements. However, it did not explain the large differences between satellite measurements and theoretical estimates.

As a first step the theoretical estimate of PJ95 was critically analyzed. I tried to determine the uncertainties in the input parameters of their calculation, namely cloud liquid water density, fractional cloud amount, and cloud thickness for five different cloud groups. I found that their cloud liquid water densities were generally at the low end of published values. Considering the truncated size range of in-situ measurements and their limited ability to sample supercooled cloud droplets, typical liquid water densities may be even higher than the ones used by PJ95. The uncertainties in cloud amounts were estimated by a comparison with the Warren atlas and the ISCCP cloud climatology. The cloud amounts of PJ95 were close to but somewhat lower than those of the Warren atlas and usually significantly larger than those of the ISCCP, especially for the wettest Cb and Ns clouds. For cloud thickness, a comparison was made with results obtained from a comprehensive radiosonde dataset (Poore et al., 1995). With the exception of St/Sc clouds for which PJ95 likely overestimated cloud thickness by a factor of 2-3, thicknesses for the other four cloud types turned out to be very reasonable. The largest differences in thickness between PJ95 and the radiosonde data occurred for Cb and Cu clouds, for which the rawinsonde observations indicated significantly thinner clouds. Poore et al. (1995), however, pointed out that for these clouds the radiosonde data were very likely underestimates due to undersampling and generally unreliable measurements at lower temperatures. Overall, the input parameters used by PJ95 seemed very reasonable with the exception of St/Sc; these clouds, however, were very dry and thus contributed little to the global mean value. Nevertheless, a conservative calculation was made when the smallest cloud amounts, thinnest clouds, and lowest water densities were used. This

yielded an absolute minimum value of 110-120 g/m^2 for the global mean atmospheric *LWP*. This lower limit was still a factor of two larger than the global average value determined from microwave measurements. This lower limit, however, was most likely unrealistically low since it used the erroneously small radiosonde cloud thickness for Cb. It was found that the likely uncertainty in the global mean value of PJ95 is about $\pm 80 \text{ g/m}^2$, which results in a global average atmospheric *LWP* no less than about 300 g/m^2 , and no greater than 460 g/m^2 .

Second, the satellite measurement techniques were analyzed. Their limitations are summarized in Figure 5.1. A review of microwave retrieval methods revealed the following shortcomings. Microwave retrievals are only obtained over oceans and thus they completely miss the most severe and wettest continental storms (e.g. mesoscale convective complexes with $LWP > 2500 \text{ g/m}^2$). The separation of the cloud and rain components is still an unresolved issue. In precipitating systems, that is where $LWP > 500 \text{ g/m}^2$, cloud liquid water is not really retrieved as an independent parameter but it is either fixed at a relatively modest value or parameterized based on rain rate. Finally, the beamfilling problem may result in retrievals that are severely biased low (Masunaga et al., 2002).

The optical technique was determined to have the following shortcomings. Retrievals are almost exclusively based on 1D plane-parallel radiative transfer theory, which neglects the 3D effects occurring in real clouds. The importance of this effect depends on cloud type. Optical thickness retrievals of cumuliform clouds are more likely to be affected by 3D effects than ones over extended stratiform clouds. An angular

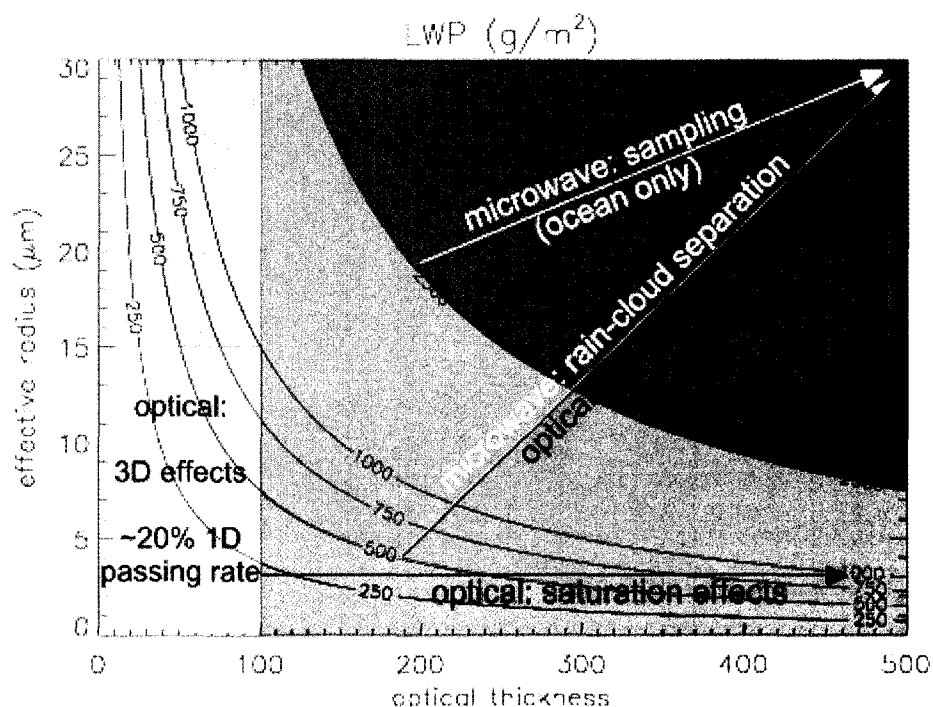


Figure 5.1 Summary of the main limitations of satellite retrieval techniques. The curves represent the isolines of LWP . For precipitating systems ($LWP > 500 \text{ g}/\text{m}^2$) the separation of the rain and cloud components (microwave technique) and the inadequate knowledge of the drop effective radius (optical technique) pose problems. The ocean-only microwave retrievals do not sample the wettest continental clouds (with $LWP > 2500 \text{ g}/\text{m}^2$). Plane-parallel optical retrievals suffer from 3D effects for thinner clouds and from saturation effects for the thickest clouds.

consistency test that compared the measured cloud anisotropy with plane-parallel model predictions revealed that at the $\pm 5\%$ relative tolerance level about 20% of global cloudiness matched the 1D theory. For the vast majority of maritime liquid clouds 1D retrievals had potentially large errors that cannot necessarily be expected to cancel. It was also found that the apparent agreement between the 1D model and measurements increased with decreasing spatial resolution. This would suggest that optical thickness retrievals should be made at coarser resolutions. The fact that clouds are apparently more plane-parallel at larger scales, however, may be misleading. The suitability of the plane-parallel model does not imply that the retrieved cloud optical thickness is unbiased. In fact, it is likely to be biased significantly low at coarser resolutions due to non-linear averaging. Regardless of 3D effects, optical thickness retrievals are inherently limited by the saturation of visible reflectances (brightness) at larger optical thicknesses. In practice, this results in an upper limit of ~ 100 in retrieved optical thickness. Above this cut-off value no information can be gained from conventional optical measurements. Finally, accurate knowledge of the drop effective radius is crucial to determine the cloud liquid water path from optical measurements. Larger drops are much less active optically than smaller ones and contribute little to the extinction coefficient, but they may contribute significantly to drop effective radius. Since liquid water path is proportional to the product of optical thickness and drop effective radius this means that information about the water amount contained in larger drops is buried in the effective radius rather than in the optical thickness. This effect is especially important in precipitating clouds (i.e. where $LWP > 500 \text{ g/m}^2$) that can be characterized by broad, bimodal drop distributions.

A comparison of the optical and microwave techniques using MISR and TMI measurements revealed the following. Relatively good agreement was found between the two techniques for low-level boundary layer clouds characterized by small *LWP* values. For these clouds one might have higher confidence in the retrievals. Unfortunately, these are among the driest clouds that, therefore, contribute little to the global mean cloud liquid water amount. For thick Cb clouds significant differences were found between the two techniques. The optical method severely underestimated the *LWP* when a commonly assumed value of 8-10 μm was used for the drop effective radius. Much better agreement was achieved when the baseline value of the effective radius was increased to 16 μm and a dependency on rain rate was also introduced. This further emphasized that these wettest clouds are likely to have broad, bimodal distributions. It also showed that using a fixed value of drop effective radius that corresponds to nonprecipitating clouds is inadequate globally and results in global averages that biased low. These thick mixed-phase clouds pose a general challenge because both the ice and liquid phases contribute to the scattered signal. Unscrambling the ice and liquid components from this signal is an unsolved problem that is somewhat analogous to separating the rain and cloud components in microwave measurements.

Finally, global liquid water path distributions were constructed by extrapolating the optical thickness retrievals above the cut-off value and using uncertainty estimates on the retrievals from the analysis of the angular (plane-parallel) optical thicknesses. This approach had two major limitations. First, the obtained uncertainty of the 1D theory was likely to be underestimated because 1D retrievals themselves were used in the

calculations. A better approach would have been to use 3D models (e.g. Monte Carlo simulations) to determine the errors of plane-parallel retrievals. True 3D and 1D comparisons are feasible in case studies, however, they are currently impractical when routinely analyzing large amounts of data. The true magnitude of uncertainties introduced by 3D effects is an area of ongoing research. Second, assumptions had to be made about the distribution of optical thicknesses above the cut-off value. The choice of the fitting model (linear, spline, sigmoidal, etc.) also introduced potential uncertainties in the final results. With the above limitations it was found that the maximum value of global mean atmospheric liquid water path could be as high as 150 g/m^2 as determined from early morning data over the oceans. This is still a factor of two smaller than the theoretical estimate of PJ95.

In summary, the difference between satellite measurements and theoretical estimates of global liquid water path, which was originally at least a factor of 4-5, was reduced to a factor of 2 by extrapolating above the cut-off optical thickness and putting uncertainties on the retrievals. However, I could not close the gap between satellite measurements and theoretical estimates. Anomalous absorption was ruled out as a possible cause for the remaining differences. The following possible explanations were explored. First, there were serious sampling issues, both spatial and temporal, that affected satellite retrievals used in this study. Both microwave retrievals and MISR optical thickness measurements were obtained only over ocean. Furthermore, the sampling of the diurnal cycle was inadequate with sun-synchronous satellites. This was especially true for the morning orbit of MISR with an equator crossing time of 10:30

AM. There is ample evidence now that points to the very different magnitude and diurnal cycle of rainfall and convective intensity over land and over ocean (e.g. Nesbitt and Zipser, 2003). Over the oceans, the diurnal cycle of rainfall and convective intensity has small amplitude with maybe a slight maximum in the early morning (6 AM). Over land areas, however, the diurnal cycle of rainfall is much larger than over the ocean, with a marked minimum in the midmorning hours (9 AM) and a maximum in the afternoon (3 PM). Also, there is a notable mid- to late afternoon (3-5 PM) maximum in convective intensity over land. This suggest that microwave measurements and my MISR optical thickness retrievals probably missed the most intensive convective events with the largest liquid water paths. Another possible source of underestimation was the inadequate knowledge of drop effective radius in precipitating clouds. The effective radius is likely to increase with rain rate as the drop size distribution broadens and becomes bimodal. Some in-situ measurements suggest that there might be significantly larger drop effective radii in clouds, even in non-precipitating clouds, than the ones assumed in this study.

The following suggestions can be made in order to close the remaining gap between satellite measurements and theoretical estimates. A technique is needed that is sensitive to the full range of cloud droplets (0-100 μm), and not just to parts of it. Better knowledge of the drop size distribution (effective radius) is required when converting optical thickness to liquid water path. This is particularly important in precipitating clouds, such as Cb and Ns, which seem to contribute most to the global mean cloud liquid water amount. The sampling of the most intensive continental precipitation features is crucial. This is difficult to achieve with satellite microwave measurements, but may be

feasible with the help of a network of ground-based upward looking microwave radiometers. Such radiometers would not be plagued by the problem posed by the varying emissivity of the land background. Finally, the better separation of rain and cloud water is also important in microwave retrievals. Utilizing the information contained in the polarization signal of rain clouds may offer a hope in this area.

APPENDIX A: GLOSSARY

ALWP	atmospheric liquid water path
AMS	American Meteorological Society
ARM	Atmospheric Radiation Measurement (program)
ATBD	algorithm theoretical basis document
AU	astronomical unit
AVHRR	Advanced Very High Resolution Radiometer
BRF	bi-directional reflectance factor
CERES	Clouds and the Earth's Radiant Energy System
CLWP	cloud liquid water path
CSIRO	Commonwealth Scientific & Industrial Research Organization
CWP	cloud water path
DAAC	Distributed Active Archive Center
DISORT	Discrete Ordinates Radiative Transfer
DMSP	Defense Meteorological Satellite Program
DN	digital number
DU	Dobson unit
EOS	Earth Observing System
ERBE	Earth Radiation Budget Experiment
ESFT	exponential-sum-fitting-of-transmission functions
ESIP	Earth Science Information Partnerships
ESMR	Electrically Scanning Microwave Radiometer

FSSP	Forward Scattering Spectrometer Probe
GCM	Global Climate Model
GIFOV	ground-projected instantaneous field of view
GOES	Geostationary Operational Environmental Satellite
ICE'89	International Cirrus Experiment 1989
IDL	Interactive Data Language
IPCC	Intergovernmental Panel on Climate Change
IR	infrared
ISCCP	International Satellite Cloud Climatology Project
ITCZ	intertropical convergence zone
IWP	ice water path
JPL	Jet Propulsion Laboratory
LOWTRAN	LOW resolution TRANsmittance
LUT	look-up table
LWP	liquid water path
MISR	Multiangle Imaging SpectroRadiometer
MODIS	Moderate-Resolution Imaging Spectroradiometer
MODTRAN	MODerate resolution TRANsmittance
NASA	National Aeronautical and Space Agency
NCDC	National Climatic Data Center
NESDIS	National Environmental Satellite, Data, and Information Service
NIMA	National Imagery and Mapping Agency

NIR	near infrared
NOAA	National Oceanic and Atmospheric Administration
NTSR	number of streams in DISORT
PJ95	Pruppacher and Jaenicke (1995)
PMS	Particle Measuring Systems
POLDER	Polarization and Directionality of the Earth's Reflectances
RAOB	radiosonde observation
REMSS	Remote Sensing Systems
RLWP	rain liquid water path
RWP	rain water path
SBDART	Santa Barbara DISORT Atmospheric Radiative Transfer
SHDOM	Spherical Harmonics Discrete Ordinate Method
SMMR	Scanning Multichannel Microwave Radiometer
SOM	Space-Oblique Mercator
SSM/I	Special Sensor Microwave/Imager
TIROS	Television InfraRed Observation Satellite
TLWP	total liquid water path
TMI	TRMM Microwave Imager
TOA	top of the atmosphere
TOMS	Total Ozone Mapping Spectrometer
TOVS	TIROS Operational Vertical Sounder
TRMM	Tropical Rainfall Measuring Mission

TWP	total water path
UCLA	University of California Los Angeles
UV	ultraviolet
WCRP	World Climate Research Programme
WGS84	World Geodetic System 1984
WK97	Wang and King (1997)
WOUDC	World Ozone and Ultraviolet Radiation Data Center
WV	water vapor

APPENDIX B: IMAGE COREGISTRATION

The multiangle MISR reflectances are referenced to the surface ellipsoid. Due to parallax effects the position of a given cloud element in this ellipsoid-referenced imagery changes from camera to camera. Conversely, a given pixel location corresponds to different cloud elements for different cameras. When the multiangle reflectances or cloud optical thicknesses are analyzed separately camera by camera this effect does not need to be considered. However, when the analysis requires the simultaneous use of the angular measurements, such as the angular consistency test described in Chapter 4, these parallax effects have to be accounted for. Parallax is largest at the highest 275-m resolution and it becomes less and less important as the data is averaged to coarser resolutions.

Parallax is caused by the height of clouds above the surface ellipsoid (stereo effect) and by their motion (“wind”) during the 7-min observation period. These two effects can be unscrambled from three appropriate images (or two parallax measurements) as done by the operational MISR wind retrieval algorithm (Horváth and Davies, 2001). This algorithm determines the average cloud top height and cloud-motion wind for every 70.4 km^2 mesoscale domain. Parallax measurements obtained during the wind retrievals were used in this study to coregister the multiangle data. First, the domain average along-track and cross-track parallaxes were calculated between the nadir camera and a particular oblique camera for every 70.4 km^2 domain and for every oblique camera. In practice only the An-Bf, An-Df, An-Ba, and An-Da parallaxes were computed using stereo matching, while the intermediate An-Af, An-Cf, An-Aa, and An-Ca parallaxes were interpolated. This was necessary to speed up calculations because stereo matching

for every nadir-oblique camera pair would have been very compute-intensive. Tests showed that the interpolated parallaxes, at least when domain averages were considered, were very close to the ones that were obtained with actual stereo matching. Then, the oblique images were shifted according to the computed nadir-oblique parallaxes. This resulted in imagery that was approximately coregistered with respect to the nadir (A_n) camera.

The main limitation of this method was that parallax was not calculated on a pixel by pixel basis but rather it was accounted for using domain mean heights and winds. This caused potential errors if there were variations (especially true of height) about the domain mean at higher resolutions. The magnitude of these errors primarily depends on the magnitude of height variations within the domain. The technique works well for stratiform clouds where cloud top height does not change much, while significant coregistration errors might occur for cumuliform and multi-layer clouds. An example is shown in Figures B1 and B2. The mesoscale winds and heights are plotted in Figure B1 for a marine Sc field. The result of coregistration is demonstrated in Figure B2 for domain 5 in row 2 within this block. Panel (a) shows the nadir camera image. Panel (b) is the average of the original nine ellipsoid-referenced images. This image resembles the photo of a moving target obtained with a long aperture time. The significant blurring in this image clearly demonstrates the parallax effects. The plus signs mark the movement of a particular cloud element from camera to camera. Finally, panel (c) plots the average of the nine images with the domain mean parallax removed. The clarity of the average image indicates that the individual camera views were properly registered at cloud top.

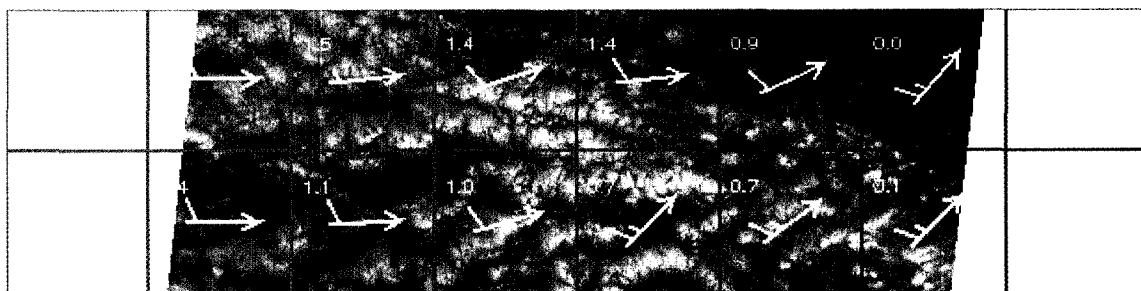


Figure B1 MISR wind retrieval for block 116 of orbit 15331. Each square region represents a 70.4 km^2 mesoscale domain. Numbers in the top left corners give the domain average cloud top heights in km.

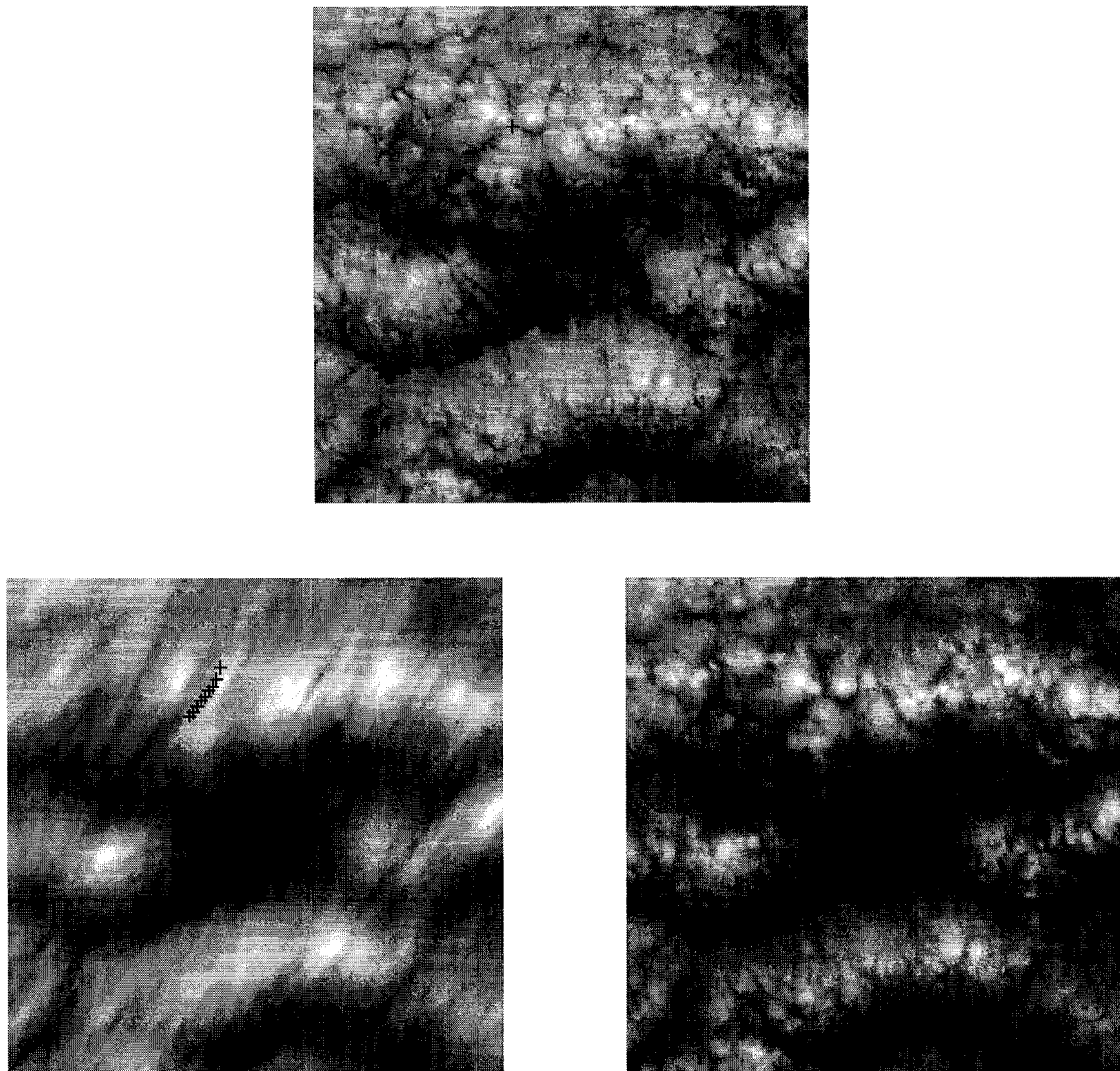


Figure B2 Coregistration example for a mesoscale domain from block 116 of orbit 15331. The domain is the fifth from the left in the second row (see Figure B1). (a) Nadir image, (b) average of nine images, and (c) average of nine images with parallax removed. In panel (b) the plus signs mark the positions of a particular cloud element in the nine images, with the lower left one referring to the Df camera and the upper right one corresponding to the Da camera.

APPENDIX C: CALCULATION OF COLUMNAR OZONE

The total column ozone optical thickness in equation (3.1) is calculated as

$$\tau_{O_3} = c_\lambda D_{O_3}, \quad (C1)$$

where c_λ is the band average ozone absorption cross-section and D_{O_3} is the column abundance of ozone given in Dobson units (DU). The proper value of c_λ for a given MISR band is calculated by weighting the cross-sections with the solar spectral irradiance, $I_{0,\lambda}$, and integrating over the spectral response function S of the band (Chandrasekhar, 1960):

$$c_\lambda = 10^{-3} \cdot L \cdot \frac{\int_{\lambda_1}^{\lambda_2} \sigma_{O_3}(\lambda) I_{0,\lambda} S(\lambda) d\lambda}{\int_{\lambda_1}^{\lambda_2} I_{0,\lambda} S(\lambda) d\lambda}, \quad (C2)$$

where $L = 2.68719 \times 10^{-19} \text{ cm}^{-3}$ is the Loschmidt number and the band considered lies between wavelengths λ_1 and λ_2 . The constant factor of 10^{-3} is needed if the column ozone abundance, D_{O_3} , is given in DU in equation (C1). The exo-atmospheric solar spectral irradiance is given by the WCRP model (WCRP, 1986) and is plotted in Figure C1. It does not change much over the MISR red band, therefore its inclusion in equation (C2) is not crucial to obtain an accurate c_λ , at least for this band.

The ozone absorption cross-sections used in this work were those of Burkholder and Talukdar (1994). Previous studies were in disagreement over the temperature dependence of the ozone absorption cross-sections (see e.g. Amoruso et al., 1990 and references therein). Burkholder and Talukdar (1994) showed that earlier cross-section measurements were limited by the accuracy in measuring the absolute ozone concentration, which could lead to erroneously large temperature dependence of the reported ozone absorption cross-sections. The more accurate measurements of Burkholder and Talukdar (1994) indicated a much weaker general dependence on temperature. The measured cross-sections vary very slightly, $<1\%$, with decreasing temperature near the peak of the Chappuis band. In the wings of the spectrum, however, the absorption cross-sections decrease significantly with decreasing temperature. Nevertheless, the integrated area of the entire absorption spectrum decreases only slightly, 1.2% , in going from 298 K to 220 K.

The Burkholder and Talukdar (1994) data set consists of ozone absorption cross-sections between 410 nm and 760 nm measured at 220 K, 240 K, 260 K, 280 K, and 298 K. Table C1 lists the band average cross-sections for the four MISR bands and for channel 1 of the NOAA-7 AVHRR. With the exception of the MISR NIR band the value of c_λ was calculated by substituting the Burkholder data into equation (C2). The Burkholder ozone cross-sections did not cover the wavelength range of the MISR NIR band (see Figure 3.6), therefore for this channel c_λ was calculated by fitting transmission calculations obtained from the moderate resolution transmittance code MODTRAN (Berk et al., 1983). As a comparison, the last column in Table C1 also gives the band average

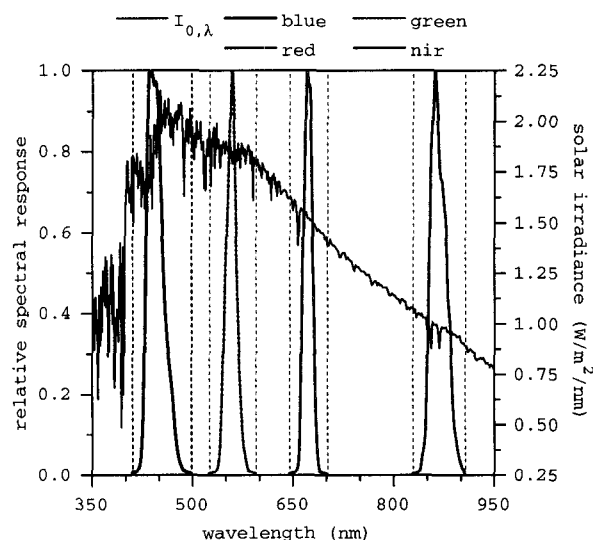


Figure C1 The WCRP solar spectral irradiance $I_{0,\lambda}$ vs. wavelength. The colored solid lines represent the MISR spectral response functions S . The colored dotted lines correspond to the wavelength regions over which the response functions are $\geq 0.5\%$.

Table C1 Values of c_λ for MISR and AVHRR channels at various temperatures as calculated from equation (C2).

Channel	T_{O_3}					ATBD
	298 K	280 K	260 K	240 K	220 K	
MISR - blue	5.06e-6	4.97e-6	4.81e-6	4.66e-6	4.40e-6	^a 4.26e-6
MISR - green	1.01e-4	1.01e-4	1.01e-4	1.01e-4	1.01e-4	^a 1.05e-4
MISR - red	4.42e-5	4.37e-5	4.35e-5	4.33e-5	4.30e-5	^a 5.09e-5
MISR - NIR	^c 2.64e-6	^c 2.64e-6	^c 2.64e-6	^c 2.64e-6	^c 2.64e-6	^a 3.94e-6
AVHRR - Ch.1	8.60e-2	8.60e-2	8.60e-2	8.60e-2	8.60e-2	^b 8.50e-2

^aMISR ATBD

^bISCCP ATBD

^cfrom fitting MODTRAN data

cross-sections reported in the MISR aerosol ATBD (Diner and Coauthors, 1999) and the ISCCP ATBD (Rossow et al., 1996). The value of c_λ is largest in the green and red bands and smallest in the blue and NIR bands. Its value generally decreases with decreasing temperature. My calculations for c_λ yielded a larger value in the blue band and smaller values in the green, red, and NIR bands as compared to the ones in the MISR aerosol ATBD. The most likely explanation for this discrepancy is that two different sets of ozone absorption cross-sections were used in this study and in the ATBD.

As a test of my calculations of c_λ , I also made computations for channel 1 of the NOAA-7 AVHRR, for which an independent empirical formula was given by Rossow et al. (1996):

$$\begin{aligned}\tau_{\text{O}_3} &= U \cdot [0.085 - 0.00052U] \\ &\approx 0.085U\end{aligned}\tag{C3}$$

where U is the column ozone amount in cm-STP. This formula was obtained from a fit to line-by-line calculations weighted by the spectral response of the AVHRR instrument. Neglecting the very small quadratic term in equation (C3) yields $c_\lambda = 0.085$. This was in excellent agreement with my calculations that determined a value of 0.086.

Even though the temperature dependence of the band average ozone absorption cross-section is relatively weak, I calculated the ozone weighted average temperature \bar{T}_{O_3} from

$$\bar{T}_{O_3} = \frac{\int U(z)T(z)dz}{\int_z U(z)dz}, \quad (C4)$$

where $U(z)$ and $T(z)$ are the vertical ozone and temperature profiles, respectively, and the integral is taken over the entire atmospheric column. The values of \bar{T}_{O_3} for six model atmospheres are given in Table C2 along with the column ozone abundances. These temperatures are in the 220 K to 240 K range. Based on this I decided to use the band average ozone absorption cross-sections calculated at a temperature of 220 K (column six in Table C1) throughout this study.

To calculate the column ozone optical thickness from equation (C1) the column ozone abundance, D_{O_3} , is also needed. Column ozone abundance is highly variable both in space and time. Therefore, rather than relying on climatological values actual total ozone measurements obtained by the TOMS instrument were used in this study. These measurements had a nominal uncertainty of 3% to 5%, which seemed more than adequate for my purposes. TOMS total ozone maps for April 9, 2001 and November 5, 2002 are given in Figure C2 and Figure C3, respectively. This data set was available on a regular latitude/longitude grid with a grid spacing of 1° in latitude and 1.25° in longitude, and was then remapped to the MISR swaths (see Appendix F for the remapping algorithm). The original data are shown in Figure C2a and Figure C3a. There were no observations at the highest latitudes on the winter hemisphere (poleward of 75°S on April 9, 2001 and poleward of 70°N on November 5, 2002). Beside that there were data void areas between

Table C2 Ozone-weighted average temperature and total column ozone abundance for various atmospheric models.

Model Atmosphere	\bar{T}_{O_3}	Total Column Ozone
tropical	233.1 K	277 DU
midlatitude summer	235.8 K	332 DU
midlatitude winter	221.9 K	377 DU
subarctic summer	237.7 K	345 DU
subarctic winter	218.1 K	376 DU
1976 US standard	228.9 K	344 DU

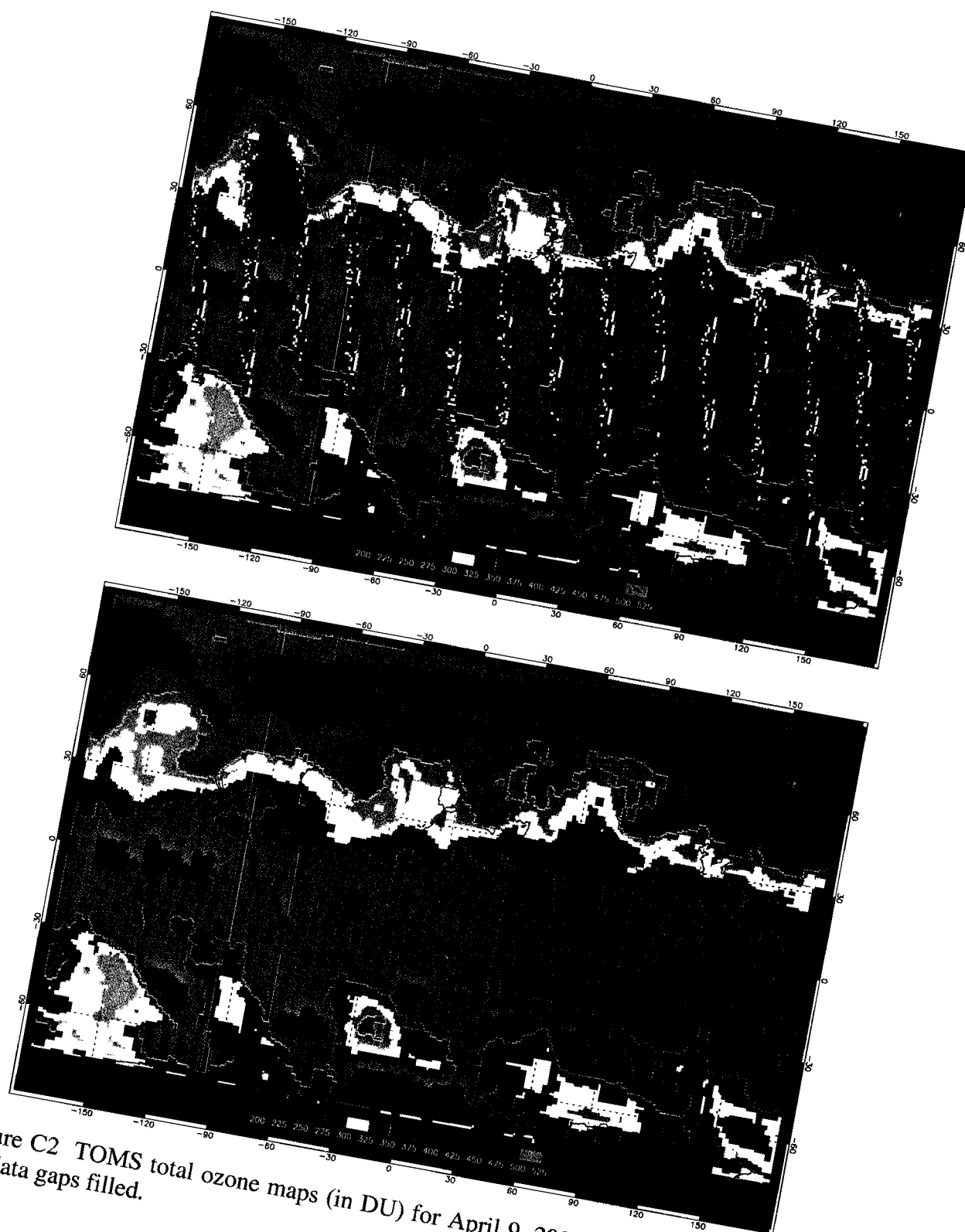


Figure C2 TOMS total ozone maps (in DU) for April 9, 2001. (a) Original data, and (b) data gaps filled.

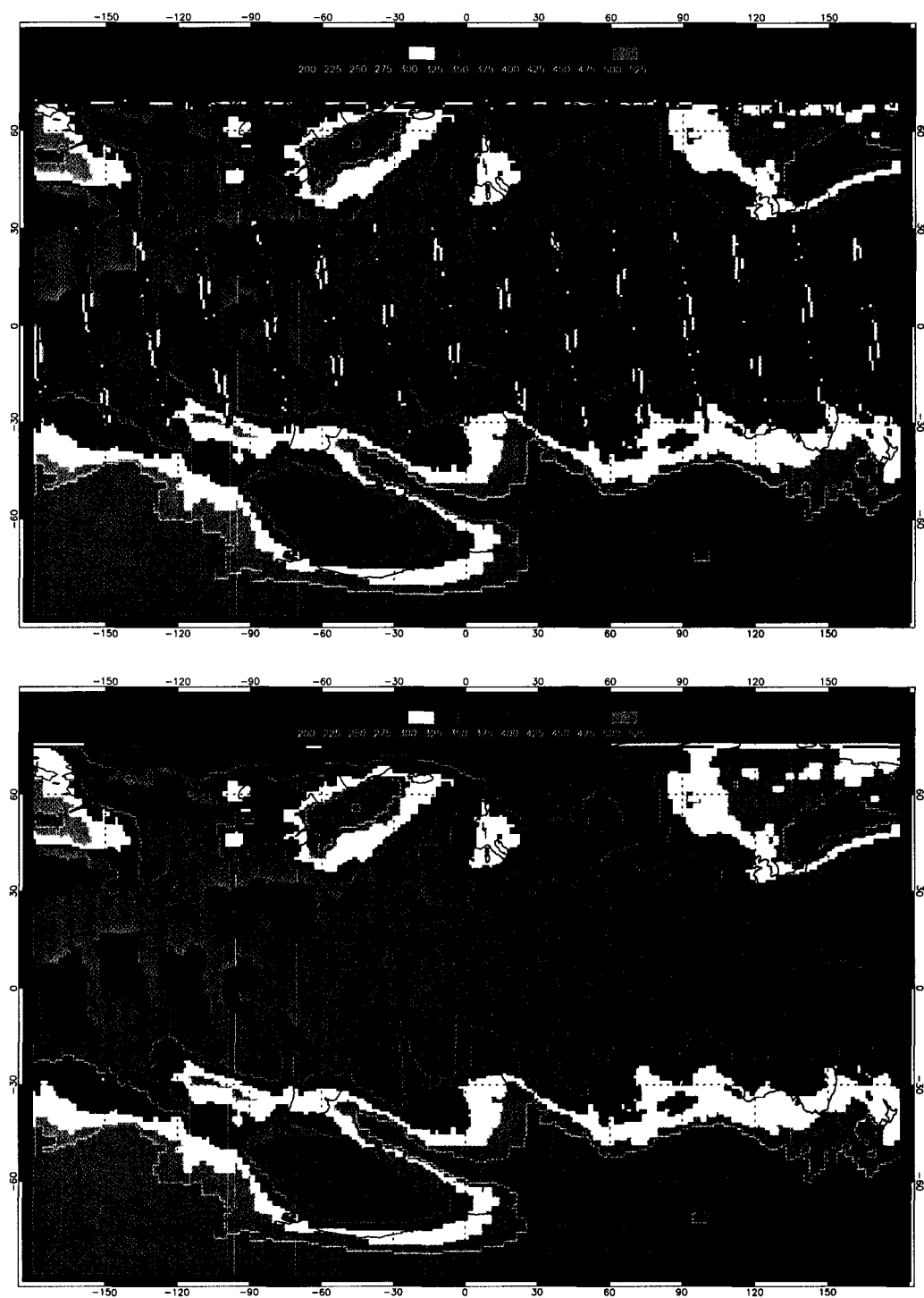


Figure C3 TOMS total ozone maps (in DU) for November 5, 2002. (a) Original data, and (b) data gaps filled.

30°S and 30°N due to the lack of overlap between consecutive orbits and a large data dropout in the eastern Pacific on April 9, 2001. With the exception of the Arctic and Antarctic areas these data gaps were filled in using thin-plate-spline interpolation (IDL's MIN_CURVE_SURF routine). These filled-in maps are plotted in Figure C2b and Figure C3b. Total ozone values are lower and spatially quite homogeneous around the equator. At higher latitudes (poleward of 30°) total ozone values are generally larger and have much more geographical variation. As a confirmation of the TOMS measurements a comparison was made with independent total ozone maps from the TOVS (TIROS Operational Vertical Sounder) instrument and the World Ozone and Ultraviolet Radiation Data Center (WOUDC). All three data sets were in quite good agreement in the spatial distribution and actual values of total ozone.

APPENDIX D: THE RAYLEIGH CORRECTION ALGORITHM

The algorithm used in this study was that of Wang and King (1997) (hereafter WK97). In the following a brief summary of the method is given. Let us consider a simplified ocean-cloud-atmosphere system, which consists of a Lambertian ocean surface with an albedo of α_{sc} , a single cloud layer with an optical thickness of τ_c , and a single air molecule layer with an optical thickness of τ_r above the cloud. In the single scattering approximation the upward visible reflectance (R) of this system at the top of the atmosphere, for view and solar zenith angles θ and θ_0 and relative solar azimuth angle $\Delta\phi$, can be written as the sum of the following four components.

Direct Rayleigh single scattering without reflection from the cloud

$$R^{(1)}(\tau_r; \theta, \theta_0, \Delta\phi) = \frac{\tau_r P_-(\theta, \theta_0, \Delta\phi)}{4 \cos \theta \cos \theta_0}, \quad (D1)$$

single scattering in the air toward the cloud followed by reflection from the cloud

$$R^{(2)}(\tau_r, \tau_c; \theta, \theta_0) = \frac{\tau_r T(\tau_r; \theta)}{4\pi \cos \theta_0} \cdot \int_{\Omega/2} P_+(\theta', \theta_0, \Delta\phi') R_c(\tau_c; \theta, \theta', \Delta\phi') d\Omega', \quad (D2)$$

reflection of the direct solar beam from the cloud followed by single scattering in the air

$$R^{(3)}(\tau_r, \tau_c; \theta, \theta_0) = \frac{\tau_r T(\tau_r; \theta_0)}{4\pi \cos \theta} \cdot \int_{\Omega/2} P_+(\theta, \theta', \Delta\phi') R_c(\tau_c; \theta', \theta_0, \Delta\phi') d\Omega', \quad (D3)$$

and reflection of the direct solar beam from the cloud

$$R^{(4)}(\tau_r, \tau_c; \theta, \theta_0, \Delta\phi) = T(\tau_r; \theta) R_c(\tau_c; \theta, \theta_0, \Delta\phi) T(\tau_r; \theta_0). \quad (D4)$$

Here R_c is the reflectance resulting from multiple scattering by the cloud in the absence of the air, P_{\pm} is the Rayleigh scattering phase function in the forward (positive) and backward (negative) directions, and $T(\tau_r; \theta) = \exp(-\tau_r / \cos \theta)$ and $T(\tau_r; \theta_0) = \exp(-\tau_r / \cos \theta_0)$ are the view path and solar path direct transmittances of the air, respectively. The Rayleigh phase function is given by

$$P(\theta_{scat}) = \frac{3}{4} (1 + \cos^2 \theta_{scat}), \quad (D5)$$

where θ_{scat} is the scattering angle, which is calculated from the solar and view zenith angles and the relative solar azimuth angle as

$$\cos \theta_{scat} = \cos \theta_0 \cos \theta + \sin \theta_0 \sin \theta \cos \Delta\phi. \quad (D6)$$

The phase function is normalized to 4π so that

$$\int_0^{2\pi} \int_0^\pi P(\theta_{scat}) \sin \theta_{scat} d\theta_{scat} d\phi = 4\pi. \quad (D7)$$

The Rayleigh phase function is plotted in Figure D1 along with the cloud phase function used in this study. Note that for scattering angles larger than $\sim 40^\circ$ the value of the Rayleigh scattering phase function is larger than that of the cloud phase function. Over the scattering angle range that is generally available for satellite remote sensing (100° - 160°) the difference between these phase functions can be as high as 1-2 orders of magnitude.

The integrals in $R^{(2)}$ and $R^{(3)}$ are difficult to evaluate since the exact cloud reflection function R_c is generally unknown. These integrals can be approximated by assuming that clouds are Lambertian reflectors with a plane albedo of A_c . Then the integrals can be written as the product of the cloud plane albedo A_c and the integral of the Rayleigh phase function over the upward hemisphere (2π), i.e.

$$R^{(2)}(\tau_r, \tau_c; \theta, \theta_0) \approx \frac{\tau_r T(\tau_r; \theta) A_c(\tau_c; \theta)}{2 \cos \theta_0}, \quad (D8)$$

and

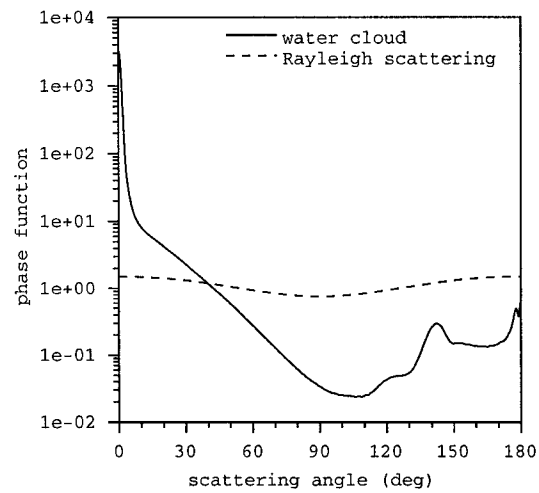


Figure D1 Rayleigh phase function and water cloud phase function at a wavelength of $\lambda = 0.672 \mu\text{m}$ (MISR red band) vs. scattering angle. The water cloud is assumed to have a gamma drop size distribution with an effective radius of $R_e = 8 \mu\text{m}$.

$$R^{(3)}(\tau_r, \tau_c; \theta, \theta_0) \approx \frac{\tau_r T(\tau_r; \theta_0) A_c(\tau_c; \theta_0)}{2 \cos \theta}. \quad (\text{D9})$$

Thus, using the single scattering approximation the total reflectance R_t at the top of the atmosphere can be written as

$$\begin{aligned} R_t(\tau_r, \tau_c; \theta, \theta_0, \Delta\phi) &= R^{(1)} + R^{(2)} + R^{(3)} + R^{(4)} \\ &= \frac{\tau_r P_-(\theta, \theta_0, \Delta\phi)}{4 \cos \theta \cos \theta_0} \\ &\quad + \frac{\tau_r A_c(\tau_c; \theta) \exp(-\tau_r / \cos \theta)}{2 \cos \theta_0} \\ &\quad + \frac{\tau_r A_c(\tau_c; \theta_0) \exp(-\tau_r / \cos \theta_0)}{2 \cos \theta} \\ &\quad + R_c(\tau_c; \theta, \theta_0, \Delta\phi) \exp[-\tau_r (1/\cos \theta + 1/\cos \theta_0)] \end{aligned} \quad (\text{D10})$$

In the case of multiple scattering it is impossible to derive an analytical formula for the total reflectance R_t . WK97, however, have shown that equation (D10) can be modified to approximate multiple scattering effects by rewriting the last term as

$$R^{(4)}(\tau_r, \tau_c; \theta, \theta_0, \Delta\phi) = R_c(\tau_c; \theta, \theta_0, \Delta\phi) \exp[-C_m \tau_r (1/\cos \theta + 1/\cos \theta_0)]. \quad (\text{D11})$$

Here $0 < C_m < 1$ is a constant factor accounting for multiple scattering. A value of $C_m = 1$ would refer to the single scattering case, while a smaller and smaller value of C_m corresponds to a stronger and stronger multiple scattering contribution. In general, the

exact value of C_m depends on the solar and view geometries, the cloud optical and microphysical properties, and cloud top pressure. However, WK97 have shown that these dependencies are relatively weak and there exists a rather constant empirical value of C_m that best fits the above equation. WK97 used a value of $C_m = 0.84$ in their simulations, in my tests, however, the Rayleigh correction algorithm worked best with a slightly smaller value of $C_m = 0.78$. This might have been due to the fact that only a single iteration was allowed in my correction algorithm as opposed to two in WK97. Reducing the number of iterations was necessary to speed up the calculations (see discussion later).

Finally, by replacing the last term in equation (D10) with equation (D11) the true cloud top reflectance $R_c^{(calc)}$ can be expressed as

$$\begin{aligned}
 R_c^{(calc)}(\tau_c; \theta, \theta_0, \Delta\phi) = & \left(R_t^{(meas)}(\tau_r, \tau_c; \theta, \theta_0, \Delta\phi) \right. \\
 & - \left[\frac{\tau_r P_-(\theta, \theta_0, \Delta\phi)}{4 \cos \theta \cos \theta_0} + \frac{\tau_r A_c(\tau_c; \theta) \exp(-\tau_r / \cos \theta)}{2 \cos \theta_0} \right. \\
 & \left. \left. + \frac{\tau_r A_c(\tau_c; \theta_0) \exp(-\tau_r / \cos \theta_0)}{2 \cos \theta} \right] \right) \\
 & \cdot \exp \left[C_m \tau_r (1 / \cos \theta + 1 / \cos \theta_0) \right]
 \end{aligned} \quad (D12)$$

Here the superscript “*meas*” refers to the MISR top-of-the-atmosphere reflectance measurements, which are the input to the correction algorithm, while the superscript “*calc*” corresponds to the calculated cloud top reflectance, which is the output of the

algorithm. To solve equation (D12) the Rayleigh optical thickness of the atmosphere above the cloud, τ_r , is needed. It is proportional to the cloud top pressure, p_c :

$$\tau_r = \frac{p_c}{p_0} \tau_{r0}. \quad (\text{D13})$$

Here, $p_0 = 1013$ hPa is the standard atmospheric pressure, and τ_{r0} is the Rayleigh optical thickness corresponding to p_0 . The value of τ_{r0} is obtained by integrating, at standard pressure, the spectral Rayleigh optical thickness $\tau_{r\lambda}$ over the spectral response function of the MISR channels. For $\tau_{r\lambda}$ the fitting formula from Hansen and Travis (1974) was used:

$$\tau_{r\lambda} = 0.008569\lambda^{-4} (1 + 0.0113\lambda^{-2} + 0.00013\lambda^{-4}), \quad (\text{D14})$$

where the wavelength λ is in μm . This fitting equation was found by Teillet (1990) to be the best match with exact calculations. The value of τ_{r0} for the four MISR bands is given in Table D1. The cloud top pressure was obtained by remapping MODIS cloud top pressures to the MISR swath (see Appendix F for the remapping algorithm). An alternative is to convert the MISR stereo-derived geometric cloud top heights to cloud top pressures using a standard atmospheric pressure profile. My tests indicated that the Rayleigh correction algorithm performed equally well with both the MODIS and the

Table D1 Rayleigh optical thickness for the MISR channels.

Channel	Rayleigh Optical Thickness
blue	0.231
green	0.093
red	0.045
NIR	0.017

MISR pressures. I opted for the MODIS pressure data set because the MISR stereo heights showed some blockiness due to problems with the wind correction. Besides, the MODIS data set did not require an additional conversion to pressure, which was an extra computational burden and required ancillary data (atmospheric profiles).

Solving equation (D12) also requires the cloud plane albedo A_c . This quantity is primarily a function of the cloud optical thickness and the solar zenith angle and has only a weak dependence on cloud drop effective radius R_e . Figure D2 depicts the cloud plane albedo as a function of the cosine of the solar zenith angle for various cloud optical thicknesses and for the three different droplet effective radii considered in this study. The A_c values in Figure D2 were computed by running DISORT for a single cloud layer over a Lambertian ocean surface with an albedo of $\alpha_{sfc} = 0.05$ (i.e. no atmospheric layer was included above the cloud). Note that A_c is only a relatively weak function of the droplet effective radius, especially for thicker clouds and larger solar zenith angles. It increases slightly with decreasing droplet effective radius. Also note that, except for the thinnest clouds, the plane albedo is approximately linearly related to the cosine of the solar zenith angle. In fact, for thicker clouds ($\tau_c \geq 6$) the plane albedo can be accurately computed from asymptotic formulas (van de Hulst, 1980; King, 1987). In practice, a lookup table of A_c was generated for a set of cloud optical thicknesses and solar zenith angles using DISORT. The particular value of A_c needed in equation (D12) was then obtained from this lookup table by interpolation.

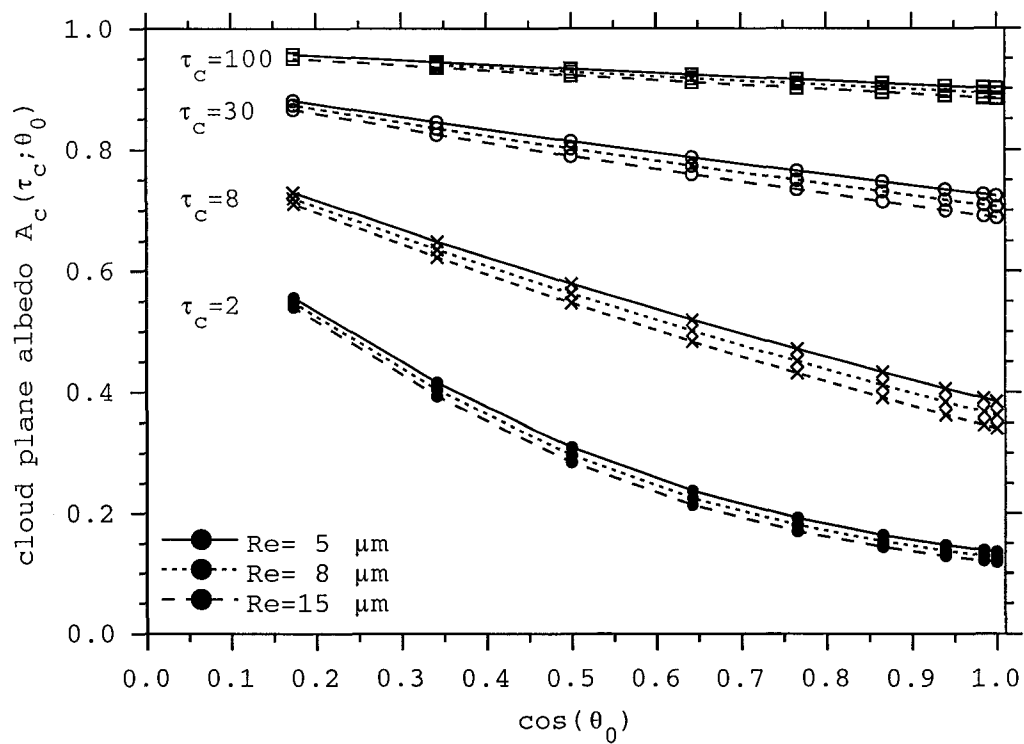


Figure D2 Cloud plane albedo as a function of the cosine of the solar zenith angle for various cloud optical thicknesses and droplet effective radii.

The correction algorithm then proceeds in the following manner. To estimate the Rayleigh scattering contributions by equation (D12) the cloud albedo A_c is required for the solar and view zenith angles. Because A_c depends on the optical thickness which is unknown a priori, the corrected top-of-the-cloud reflectance, $R_c^{(calc)}$, is computed by iteration:

$$R_t^{(meas)} \rightarrow [\tau_c^i \rightarrow A_c^i \rightarrow R_c^{(calc,i)}], \quad (D15)$$

where the brackets indicate iteration with equation (D12) and $i = 0, 1, 2, \dots$ refers to the iteration step. The case $i = 0$ corresponds to no Rayleigh correction. Fortunately, equation (D15) converges very rapidly, usually within two iterations ($i = 2$).

It is noted here that the Rayleigh scattering contribution to the total signal measured at the top of the atmosphere can be both negative and positive. The error analysis in WK97 has shown that when the view and/or the solar zenith angle are large and the cloud is bright, the Rayleigh contribution could become negative. Both enhancement and reduction of the cloud-top reflectance is possible because the Rayleigh phase function is very bland and symmetric (with respect to a scattering angle of 90°), whereas the cloud phase function is very strongly forward peaked. Therefore, Rayleigh scattering tends to add reflectance where the cloud is reflecting weakly but tends to reduce reflectance in the directions of strong cloud scatter. This phenomenon and the rapid convergence of the iteration in equation (D15) are illustrated in Figure D3. This

example shows the procession of the correction algorithm for the most oblique D camera, for which Rayleigh scattering effects are the most important. In panel (a), Rayleigh scattering adds to the cloud-top radiance of a relatively weakly scattering thin cloud ($\tau_c \approx 7$), hence the correction is negative. As a result of a 2.3% relative decrease in radiance, the retrieved optical thickness decreases by 5.1%. In panel (b), Rayleigh scattering removes from the cloud-top radiance of a bright thick cloud ($\tau_c \approx 68$), hence the correction is positive. Here a mere 0.8% relative increase in radiance results in a 7.6% increase in the retrieved optical thickness due to the enhanced sensitivity of optical thickness to radiance for thicker clouds. Note that in both cases the largest correction by far occurred during the first iteration and that the algorithm basically converged in two steps. Because Rayleigh correction has to be applied to every single pixel, it is computationally very costly. To reduce the computational burden only the first iteration, which is by far the most significant, was calculated in this study. To partly compensate for this reduction in the number of iterations the value of the multiple-scattering factor was reduced to $C_m = 0.78$, which seemed to work best in my tests. These modifications did not change the results in any significant manner.

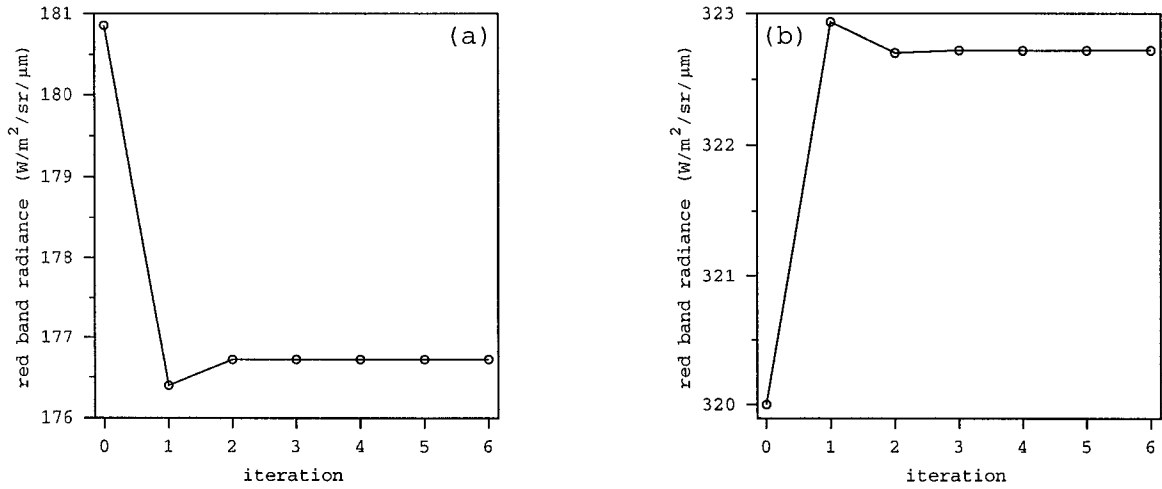


Figure D3 Convergence of the Rayleigh correction algorithm. (a) Thin faint cloud: $\tau_c^{(i)} = 7.237$ (uncorrected), 6.841, 6.871, 6.869, 6.869, 6.869, 6.869 (corrected). (b) Thick bright cloud: $\tau_c^{(i)} = 62.734$ (uncorrected), 67.919, 67.472, 67.508, 67.505, 67.506, 67.506 (corrected). Here $\tau_c^{(i)}$ is the cloud optical thickness in the i th iteration step and $i = 0, 1, 2, 3, 4, 5, 6$. The following parameters were used: $\theta_0 = 42^\circ$, $\theta = 71^\circ$, $\Delta\phi = 148^\circ$, $\tau_r = 0.045$, and $C_m = 0.84$.

APPENDIX E: ANGULAR CONSISTENCY STUDY

Anisotropy of water cloud reflectance: A comparison of measurements and 1D theory

Ákos Horváth

Department of Atmospheric Sciences, The University of Arizona, Tucson, Arizona, USA

Roger Davies

Jet Propulsion Laboratory, California Institute of Technology, Pasadena, California, USA

Received 11 August 2003; revised 13 October 2003; accepted 20 November 2003; published 3 January 2004.

Abstract. Bi-directional reflectances of marine liquid water clouds, as measured by the Multiangle Imaging SpectroRadiometer (MISR), are compared with plane-parallel radiative transfer model calculations. We define an angular consistency test that requires measured and modeled radiances to agree within $\pm 5\%$ for all chosen view angles for the observations to be classified as plane-parallel. When all nine MISR angles are used at the full 275 m resolution, 1 in 6 pixels (17%) pass the test. There is a slight dependence on effective radius R_e , with $R_e=8\text{ }\mu\text{m}$ resulting in the highest pass rate. As the resolution is degraded, clouds appear more plane-parallel, and the passing rate increases to 38% at the coarsest 17.6 km scale. The passing rate quickly decreases as the number of angles used in the angular test increases. Requiring a match at only the nadir and two near-nadir angles immediately eliminates half of the full resolution pixels.

1 Introduction

Due to its simplicity and computational speed, the plane-parallel radiative transfer model enjoys widespread popularity in the satellite remote sensing of cloud properties. This approach assumes locally one-dimensional clouds and, for visible radiances, a prescribed cloud droplet size distribution. Since 3D effects, such as cloud top structure, side illumination, and horizontal photon transport can cause significant departures from plane-parallel theory in realistic cloud fields [Loeb *et al.*, 1997], its applicability to global cloudiness may be limited.

The performance of the plane-parallel radiative transfer model can be evaluated by comparing model generated bi-directional reflectance distributions with observations. Studies based on traditional single-view instruments, which lack the ability of capturing the instantaneous distribution of angular radiances, can offer only statistical comparisons with generic reflectance models composited from several different cloud scenes [Stuhlmann *et al.*, 1985; Baldwin and Coakley, 1991; Loeb and Davies, 1997]. Novel instruments, such as MISR and the Polarization and Directionality of the Earth's Reflectances (POLDER), on the other hand, provide near-simultaneous bi-directional reflectances, and therefore allow the evaluation of the plane-parallel assumption for individual clouds. The multiangle approach also holds the possibility of relaxing the condition of fixed cloud microphysics and directly retrieving the single scattering phase function [Spinhirne *et al.*, 1996; Doutriaux-Boucher *et al.*, 2000; Parol *et al.*, 2000].

Some important constraints on the validity of the plane-parallel assumption have already been established. For example, Doutriaux-Boucher *et al.* [2000] found that due to

the wide range of particle shapes and sizes, the modeling of ice cloud reflectance poses a much greater challenge than that of liquid clouds. Extended stratocumulus decks were found to behave, at least on average, like plane-parallel layers [Descloitres *et al.*, 1998]. Nevertheless, Loeb and Davies [1996] recommended that the application of the plane-parallel radiative transfer model should be restricted to moderate to high sun elevations and view angles in the backscatter direction. In addition, Buriez *et al.* [2001] pointed out the model's weakness in the rainbow and forward scattering directions.

Most previous studies were restricted by coarse resolution or were limited to certain cloud types. The aim of our paper is to extend the analysis to a globally more representative, relatively high resolution data set. In the following, we try to quantify how frequently the plane-parallel radiative transfer model with fixed microphysics captures cloud anisotropy as measured by MISR and examine the effect of pixel resolution, effective radius, and number of measurement angles on the results. We limit the analysis to liquid clouds over ice-free oceans and note that data sampling is restricted by the instrument's mid-morning sun-synchronous polar orbit with an equator crossing time of 10:45 am.

2 Data and Methodology

MISR on the *Terra* satellite measures reflected sunlight with nine pushbroom sensors oriented at different angles along track [Diner *et al.* 2002]. The traditional nadir view is complemented by four pairs of oblique cameras positioned at nominal view zenith angles of 26.1°, 45.6°, 60°, and 70.5°. Each oblique pair consists of one camera

looking forward and one looking backward, with respect to the direction of flight. Since the time interval between the two most oblique observations is 7 min, the instrument allows almost instantaneous sampling of the bi-directional reflectance field. The sampling, however, is limited to the nine fixed angles in a single azimuthal plane, determined by the flight direction with respect to the sun. Of the four available spectral channels, only the red band (672 nm) is used in this study since this offers the highest resolution. The cross-track resolution is 275 m, while the along-track resolution increases with view angle, from 214 m at nadir to 707 m at the most oblique angle. The along-track sample spacing, however, remains at 275 m.

We used a total of 28 orbits from two particular days – orbits 6956-6969 acquired on April 9, 2001, and orbits 15330-15343 collected on November 5, 2002. Only maritime clouds between 60°N and 60°S were considered. Areas contaminated with sea ice were carefully removed from each orbit. Moderate-Resolution Imaging Spectroradiometer (MODIS, also on *Terra*) cloud phase data were remapped to the MISR swaths and used to filter out mixed phase and ice clouds. The red band spectral radiances were then corrected for Rayleigh scattering and ozone absorption. Rayleigh correction used the method outlined in *Wang and King* [1997] with remapped MODIS cloud top pressures as input. Ozone absorption cross sections provided by *Burkholder and Talukdar* [1994] were integrated over the MISR spectral response function and used in conjunction with remapped Total Ozone Mapping Spectrometer (TOMS) columnar ozone abundances. Gaseous absorption by other constituents, such as water vapor, was negligible.

The measured anisotropy of cloud reflectance was then directly compared with plane-parallel calculations performed by the discrete ordinate code DISORT [Stamnes *et al.*, 1988]. No aerosols were included in the model and the ocean surface was assumed to be Lambertian with an albedo of 5%. To account for the inadequacy of the surface reflectance model, clouds with an optical thickness below 3 were excluded from the analysis. The single scattering phase function was obtained from Mie theory assuming a typical gamma droplet size distribution. In addition to our reference case with an effective radius of $R_e=8\text{ }\mu\text{m}$, we also made calculations for $R_e=5\text{ }\mu\text{m}$, and $R_e=15\text{ }\mu\text{m}$.

A simple angular consistency test was then applied to the data. A pixel passes our plane-parallel test if there is an optical thickness for which the measurements match plane-parallel radiative transfer model radiances at all angles within a given relative tolerance. The tolerance is arbitrarily set to $\pm 5\%$, which is sufficiently larger than the 1% accuracy of the relative radiometric calibration of the nine cameras [Bruegge *et al.*, 2002]. An example is shown in Figure E1. In panel (a) a plane-parallel model cloud of optical thickness 37 fits the measurements reasonably well, and thus passes the test. In panel (b), however, the model cannot explain the observed cloud anisotropy within the retrieved optical thickness range of 15 to 40, and hence fails the test.

We note here that coregistration of the multiangle views at cloud level poses a considerable challenge. There may be navigation errors, biasing our passing rates low at the highest resolutions ($<1.1\text{ km}$). More generally, parallax effects due to cloud height and motion have to be considered. Here we accounted for parallax by using the 70-km domain averaged winds and heights routinely obtained from stereo matching in the MISR

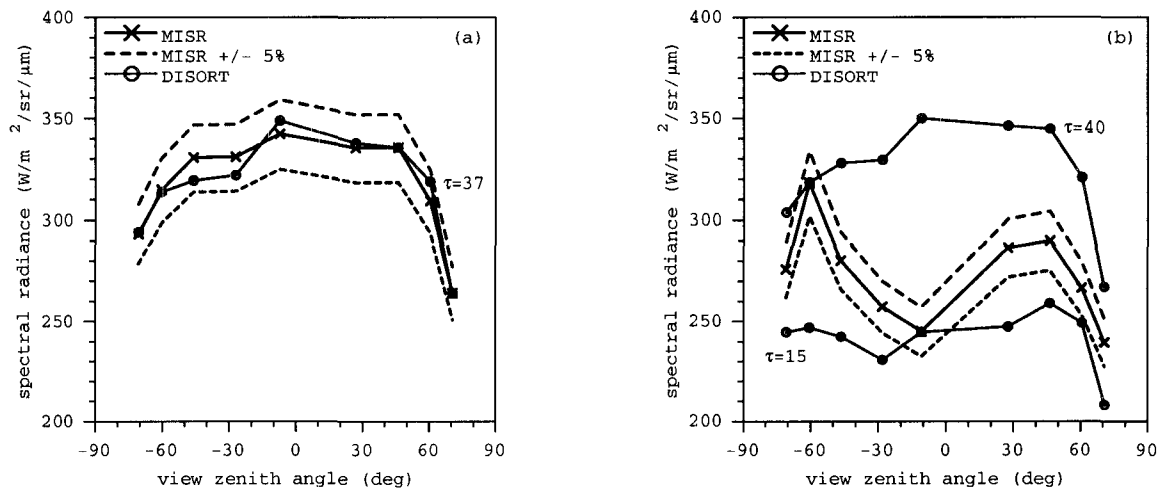


Figure E1 Comparison of measured and plane-parallel angular reflectances at a resolution of 275 m. (a) Cloud passes the angular test. (b) Cloud fails the angular test. Both examples are from block 118 (centered at 34°S, 113°E) of orbit 6156. The solar zenith angle is 33° and the measurements are approximately in the 40°/220° azimuthal plane. Data points with negative (positive) view zenith angles are in the forward (backward) scattering direction.

wind retrieval algorithm [*Horváth and Davies, 2001*], assuming constancy within each domain for computational expediency. The uncertainty due to this assumption was tested against the MISR operational reprojected radiances for cloud tops at a 2.2 km resolution and found to introduce an additional uncertainty in the passing rates of about 2% at that resolution. Combining sampling errors due to natural variability, the overall uncertainty in our passing rates is about 5% at 2.2 km resolution. The coregistration error decreases at coarser resolution, but may bias the passing rates low at the highest resolutions (< 1.1 km).

3 Results

3.1 Dependence on Cloud Droplet Effective Radius

Table E1 gives the passing rates, at 275 m resolution and averaged over the 28 orbits, for the three different effective radii we considered. In general, approximately one pixel in six passes our test. The best agreement between model and observations is obtained with an effective radius of 8 μm , while a radius of 15 μm yields the worst results. Comparison of the passing rates for individual cloud scenes (not shown) reveals that in the vast majority of cases the 15 μm effective radius model is clearly less adequate than the 8 μm model. The 5 μm effective radius model, on the other hand, compares much more favourably with the 8 μm model, with only slightly smaller passing rates most of the time.

The scarcity of well established global climatologies of cloud droplet effective radius makes it difficult to put the above results in perspective. The near-global survey of

Table E1 Average passing rate at a resolution
of 275 m vs. effective radius

Effective Radius	Passing Rate
5 μm	16%
8 μm	17%
15 μm	14%

Han et al. [1994] estimated the mean effective radius as $\sim 12 \mu\text{m}$ for marine clouds. This would imply that, on average, the angular reflectance pattern measured by MISR is more isotropic than the plane-parallel prediction corresponding to this global value. A possible explanation could be that cloud top structure makes reflected radiation more diffuse and less anisotropic compared to the plane-parallel radiative transfer model. In situ measurements [*Miles et al.*, 2000] and a global POLDER data set [*Bréon and Colzy*, 2000], however, suggest a typical cloud droplet effective radius that is a couple of microns smaller than the value of *Han et al.* [1994]. This is also more consistent with our findings. We note, however, that the effective radius that yields the highest passing rates is representative only of clouds that match the plane parallel model, and not necessarily representative of global cloudiness.

3.2 Dependence on Resolution

Figure E2 shows the passing rate as a function of pixel resolution for our reference case ($R_e = 8 \mu\text{m}$). In general, clouds appear more and more plane-parallel as the resolution is degraded. However, even at the coarsest resolution of 17.6 km, no more than 38% of the pixels pass the angular consistency test. The better agreement, at coarser resolutions, between the 1D model and measurements might be due to the partial cancellation of 3D effects. For instance, sunlit and shadowy cloud sides are averaged together, and the net horizontal photon transport is decreased at lower resolutions.

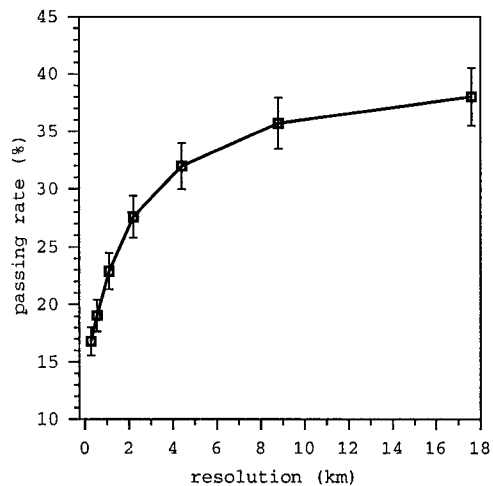


Figure E2 Angular test passing rate vs. pixel resolution for $R_e=8\text{ }\mu\text{m}$. Error bars correspond to the standard error in the mean.

3.3 Dependence on Number of Cameras

We also investigated how the results change as more and more oblique cameras are added to the angular test (see Figure E3). As expected, the passing rate decreases as the number of angles (at which matches between model and measurement are required) increases. The decrease is close to linear at the 17.6 km scale, while at the resolution of 275 m the largest change already occurs when two more cameras are used in addition to the nadir view. Adding the two near-nadir angles to the test eliminates half of the full resolution pixels.

4 Summary

Multiangle radiances acquired by MISR have been analyzed to evaluate the validity of the plane-parallel cloud assumption. We devised a simple angular test that compares the measured cloud anisotropy with model predictions. At the 5% relative tolerance level only a modest percentage, 17% or 1 pixel in 6, of the highest resolution data pass our test. The results are calculated assuming constant cloud microphysics, tuned to give a maximum passing rate with an effective radius of $R_e=8 \mu\text{m}$. Dynamic adjustment of cloud microphysics might give slightly higher passing rates.

There is a clear dependence of passing rate on pixel resolution. The passing rate first increases as the resolution is degraded, then it levels off at larger spatial scales. Even at the coarsest resolution, no more than 38% of the pixels pass the angular test. While the passing rates at the highest resolutions ($< 1.1 \text{ km}$) have slightly higher uncertainty and a likely negative bias due to possible coregistration errors, the secular rise of passing rate

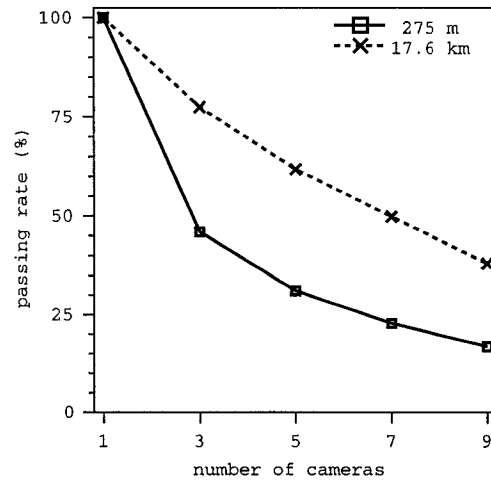


Figure E3 Angular test passing rate vs. number of cameras for $R_e=8\text{ }\mu\text{m}$.

with degraded resolution is not a coregistration issue. Rather, as the subpixel details of a scene become averaged (cf. an out of focus image) the scene appears to behave more like a plane parallel one. Analogous resolution-dependent effects were noted earlier by *Di Girolamo et al.* [1998] and by *Oreopoulos and Davies* [1998].

The fact that clouds are apparently more plane-parallel at larger scales, however, may be misleading. The suitability of the plane-parallel radiative transfer model does not imply that the retrieved cloud properties, such as optical thickness, are unbiased.

Our angular heterogeneity results can be contrasted with the spatial heterogeneity study of *Genkova and Davies* [2003]. On a similar but larger MISR data set they found that, depending on the view angle, only 1-5% of all 8.8 km² cloud scenes passed their spatial homogeneity test. This and our significantly larger angular passing rates imply that an apparent match between observed and plane-parallel angular reflectances does not necessarily require spatial homogeneity, at least on an 8.8 km scale. The same qualitative result, i.e. a much larger spatial than angular variation of cloud optical thickness, was also reported by *Parol et al.* [2000] for POLDER data.

We note in closing that the issues of coregistration, cloud microphysics, and sun-synchronous sampling may affect these passing rates by a percent or two here and there, but that the main conclusion seems inescapable. The vast majority of maritime liquid water clouds fail a simple 1D angular test at the $\pm 5\%$ level in radiance. The retrieval errors thus introduced cannot necessarily be expected to cancel, given the nonlinear dependence of reflected radiance on optical depth. Conversely, there is a significant subset (around 20%) of global cloudiness that passes the angular test and could be

amenable to analysis by 1D theory with higher confidence perhaps. Such confidence would rest on the ability to identify the correct subset of clouds, as well as an understanding of the sufficiency of the angular test (deferred to a future study).

Acknowledgments. This work was supported by the Jet Propulsion Laboratory (JPL) of the California Institute of Technology under Contract 960489. The authors thank C. M. Moroney from JPL for her considerable computational help, and D. J. Diner also of JPL for many stimulating discussions. Á. Horváth acknowledges the hospitality of the Department of Atmospheric Sciences at the University of California Los Angeles (UCLA), where he was conducting part of this research as a visiting scholar. We also thank two anonymous reviewers for constructive comments on the paper.

References

- Baldwin, D. G., and J. A. Coakley, Jr., Consistency of Earth Radiation Budget Experiment bi-directional models and the observed anisotropy of reflected sunlight, *J. Geophys. Res.*, **96**, 5195-5207, 1991.
- Bréon, F. M., and S. Colzy, Global distribution of cloud droplet effective radius from POLDER polarization measurements, *Geophys. Res. Lett.*, **27**, 4065–4068, 2000.
- Bruegge, C. J., N. L. Chrien, R. R. Ando, D. J. Diner, W. A. Abdou, M. C. Helmlinger, S. H. Pilorz, and K. J. Thome, Early validation of the Multi-angle Imaging SpectroRadiometer (MISR) radiometric scale, *IEEE Trans. Geosci. Remote Sensing*, **40**, 1477-1492, 2002.
- Buriez, J. C., M. Doutriaux-Boucher, F. Parol, and N. G. Loeb, Angular variability of the liquid water cloud optical thickness retrieved from ADEOS-POLDER, *J. Atmos. Sci.*, **58**, 3007-3018, 2001.
- Burkholder, J. B., and R. K. Talukdar, Temperature dependence of the ozone absorption spectrum over the wavelength range 410 to 760 nm, *Geophys. Res. Lett.*, **21**, 581-584, 1994.
- Descloitres, J., J. C. Buriez, F. Parol, and Y. Fouquart, POLDER observations of cloud bi-directional reflectances compared to a plane-parallel model using the ISCCP cloud phase functions, *J. Geophys. Res.*, **103**, 11,411-11,418, 1998.
- Di Girolamo, L., T. Várnai, and R. Davies, Apparent breakdown of reciprocity in reflected solar radiances, *J. Geophys. Res.*, **103**, 8795–8803, 1998.
- Diner, D. J., J. C. Beckert, G. W. Bothwell, and J. I. Rodriguez, Performance of the MISR instrument during its first 20 months in Earth orbit, *IEEE Trans. Geosci. Remote Sensing*, **40**, 1449-1466, 2002.
- Doutriaux-Boucher, M., J. C. Buriez, G. Brogniez, L. C.-Labonnote, and A. J. Baran, Sensitivity of retrieved POLDER directional cloud optical thickness to various ice particle models, *Geophys. Res. Lett.*, **27**, 109–112, 2000.

- Genkova, I., and R. Davies, Spatial heterogeneity of reflected radiance from globally distributed clouds, *Geophys. Res. Lett.*, 30(21), 2096, doi:10.1029/2003GL018194, 2003.
- Han, Q., W. B. Rossow, and A. A. Lacis, Near-global survey of effective droplet radii in liquid water clouds using ISCCP data, *J. Climate*, 7, 465-497, 1994.
- Horváth, Á., and R. Davies, Feasibility and error analysis of cloud motion wind extraction from near-simultaneous multiangle MISR measurements, *J. Atmos. Oceanic Technol.*, 18, 591-608, 2001.
- Loeb, N. G., and R. Davies, Angular dependence of observed reflectances: A comparison with plane parallel theory, *J. Geophys. Res.*, 102, 6865-6881, 1997.
- Loeb, N. G., and R. Davies, Observational evidence of plane parallel model biases: apparent dependence of cloud optical depth on solar zenith angle, *J. Geophys. Res.*, 101, 1621-1634, 1996.
- Loeb, N. G., T. Várnai, and R. Davies, Effect of cloud inhomogeneities on the solar zenith angle dependence of nadir reflectance, *J. Geophys. Res.*, 102, 9387-9395, 1997.
- Miles, N. L., J. Verlinde, and E. E. Clothiaux, Cloud droplet size distributions in low-level stratiform clouds, *J. Atmos. Sci.*, 57, 295-311, 2000.
- Oreopoulos, L., and R. Davies, Plane parallel albedo biases from satellite observations. Part I: Dependence on resolution and other factors, *J. Climate*, 11, 919-932, 1998.
- Parol, F., J. Descloitres, and Y. Fouquart, Cloud optical thickness and albedo retrievals from bi-directional reflectance measurements of POLDER instruments during ACE-2, *Tellus*, 52B, 888-908, 2000.
- Spinhirne, J. D., W. D. Hart, and D. L. Hlavka, Cirrus infrared parameters and shortwave reflectance relations from observations, *J. Atmos. Sci.*, 53, 1438-1458, 1996.

Stamnes, K., S.-C. Tsay, W. J. Wiscombe, and K. Jayaweera, Numerically stable algorithm for discrete-ordinate-method radiative transfer in scattering and emitting layered media, *Applied Optics*, 27, 2502-2509, 1988.

Stuhlmann, R., P. Minnis, and G. L. Smith, Cloud bi-directional reflectance functions: a comparison of experimental and theoretical results, *J. Appl. Opt.*, 24, 396-401, 1985.

Wang, M., and M. D. King, Correction of Rayleigh scattering effects in cloud optical thickness retrievals, *J. Geophys. Res.*, 102, 25,915-25,926, 1997.

APPENDIX F: REMAPPING ALGORITHM

In the cloud optical thickness retrieval and the subsequent analysis it was necessary to remap ancillary data sets to the MISR orbits. The algorithm outlined here was used to remap (i) MODIS cloud phase, (ii) MODIS cloud top pressure, (iii) TOMS total column ozone, and (iv) TRMM liquid water path data to the MISR swaths. The algorithm to remap data set A , which can be any of the above four data sets, to a given MISR orbit proceeds as follows.

1. Using the latitudes and longitudes (λ_A, ϕ_A) for data set A and (λ_M, ϕ_M) for MISR compute the corresponding Cartesian mapping coordinates (x_A, y_A) and (x_M, y_M) . For latitudes $\geq 70^\circ$ a polar stereographic projection, for latitudes $< 70^\circ$ a cylindrical projection was used.
2. For a given pixel in data set A with mapping coordinates (x_A, y_A) calculate the associated Voronoi (or Thiessen) polygon in the mapping plane. This polygon defines the area whose points are closest to pixel (x_A, y_A) .
3. Determine those MISR pixels (x_M, y_M) that fall within the Voronoi polygon of (x_A, y_A) . Set the value of all these MISR pixels to $A(x_A, y_A)$.
4. Repeat steps 2 and 3 for every pixel in data set A .

This algorithm essentially resamples data set A at the MISR pixel locations using nearest-neighbor interpolation. The main limitation of the method is that it relies on latitude and

longitude information, therefore it is only as accurate as the absolute georectification of the data sets used. Precision remapping would have required polynomial image transformations based on automated identification of (cloud) control points. Such a complex and compute-intensive approach was not feasible in this study given the amount of data that was processed. The algorithm outlined above is very fast and works adequately as long as the fields to be remapped vary on scales larger than the spatial remapping errors. This seems to be the case for cloud phase, cloud top pressure and total column ozone.

The various data sets used in this study were given at different resolutions. MISR latitudes and longitudes were given at a scale of 1.1 km. The pixel level (275 m resolution) values were obtained by linear interpolation. MODIS latitudes and longitudes were given at a 5-km scale. MODIS cloud phase and cloud top pressure were also given at a 5-km resolution. The TOMS total column ozone data set was available on a regular latitude/longitude grid with a grid spacing of 1° in latitude and 1.25° in longitude. Finally, the TRMM liquid water path data set was also given on a regular grid with a grid spacing of 0.25° in both latitude and longitude.

To demonstrate its performance the remapping algorithm was applied to MODIS reflectances in Figure F1. The 1-km resolution MODIS red band BRFs, which were from the MOD02 product, were remapped to a particular MISR block at a resolution of 1.1 km. Panel (a) shows the MISR red band nadir (A_n) BRFs and panel (b) gives the remapped MODIS red band BRFs. The two images look very similar. The discrepancy between the corresponding image locations of a given cloud feature is 1-2 (1.1-km resolution) pixels.

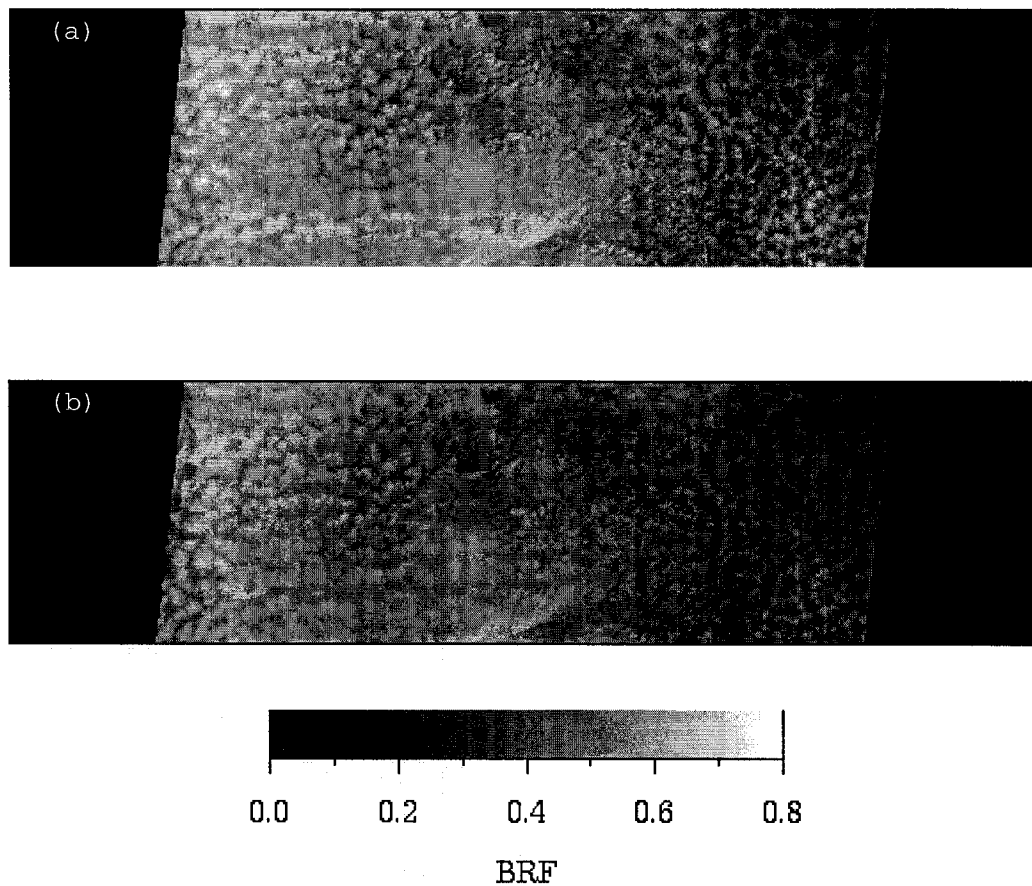


Figure F1 Remapping example for block 117 of orbit 15338. (a) MISR red band BRFs at a resolution of 1.1 km, and (b) MODIS red band BRFs remapped to the MISR grid. The imaged area is ~140 km long, and ~410 km wide.

The remapped MODIS cloud phase mask for this particular MISR block is plotted in Figure F2a. The original cloud phase data, which is the `Cloud_Phase_Infrared_Day` field in the MOD06 product, can take the following six values: 0-missing, 1-water, 2-ice, 3-mixed, 4-ice, 5-water, and 6-uncertain. Since in this study the ice and mixed-phase pixels were excluded, the original phase data were regrouped as 0-missing (magenta), 1(=1,5)-water (green), and 2(=2,3,4,6)-ice/mixed phase (red) to aid visualization. It is interesting to note that the MODIS phase mask indicates ice/mixed-phase clouds over a much larger area than does the MISR nadir image (see Figure F1a). This is due to the presence of thin cirrus above the marine Sc layer. This thin cirrus is not visible in the nadir image, however, it stands out in the most oblique Df (Figure F2b) and Da (Figure F2c) images due to the increased view path. Note how the thin cirrus aloft blurs out the cellular structure of the low-level Sc in the oblique images.

Finally, the remapped MODIS cloud top pressure (`Cloud_Top_Pressure_Day` field in the MOD06 product) and TOMS total column ozone are shown in Figure F3a and Figure F3b, respectively. The cloud top pressure field clearly indicates a lower (700-750 mb) and a higher (300-350 mb) layer and it is in fair agreement with the cloud phase mask (see Figure F2a). Total column ozone shows only ~10% variation over the entire MISR block. The large blocks of constant total ozone appear due to the coarse resolution of the TOMS data set.

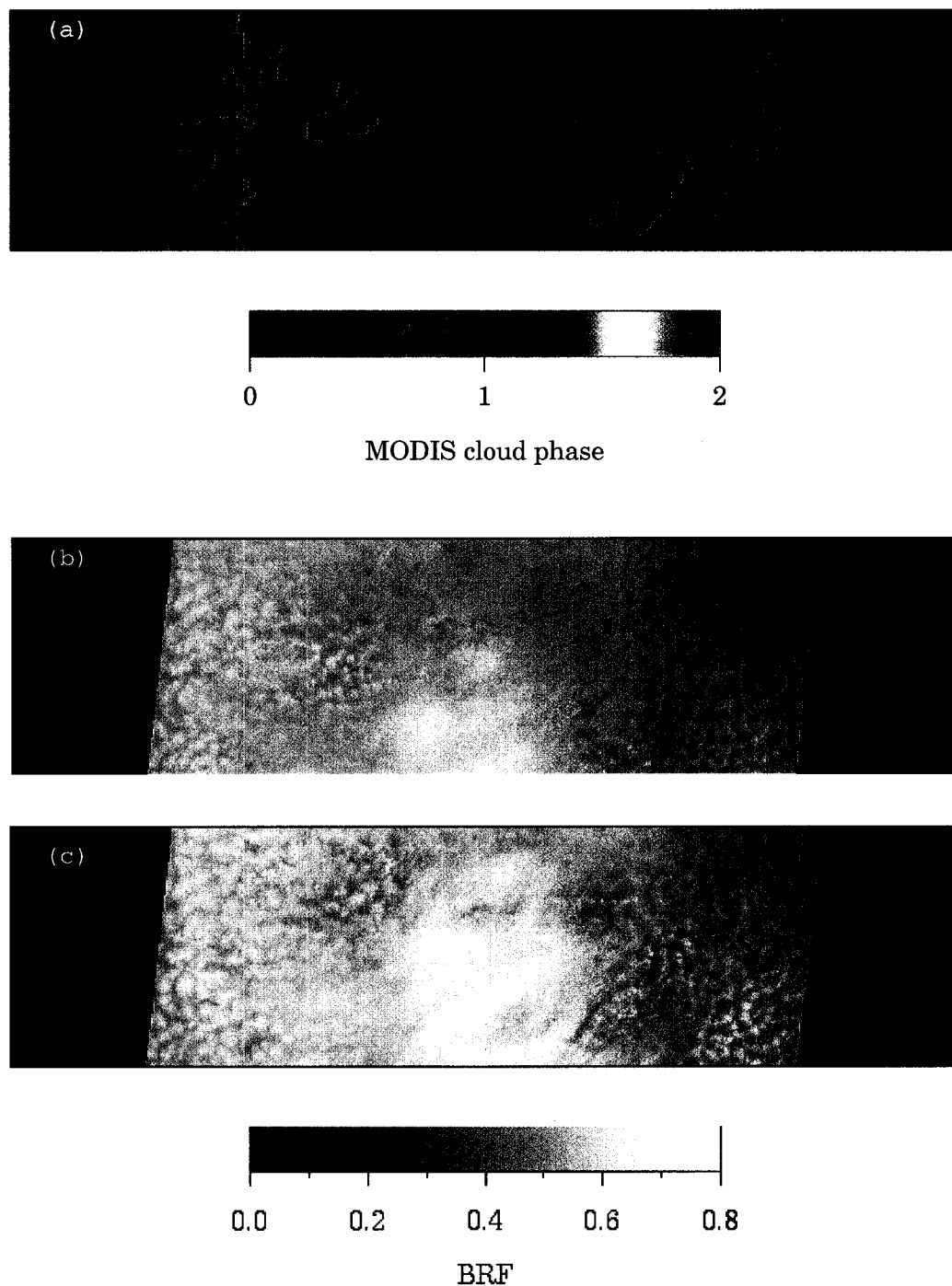


Figure F2 (a) Remapped MODIS cloud phase, (b) MISR red band Df BRFs, and (c) MISR red band Da BRFs for block 117 of orbit 15338. The phase mask can take the following values: 0 (magenta) – data void, 1 (green) – water, and 2 (red) – ice/mixed-phase.

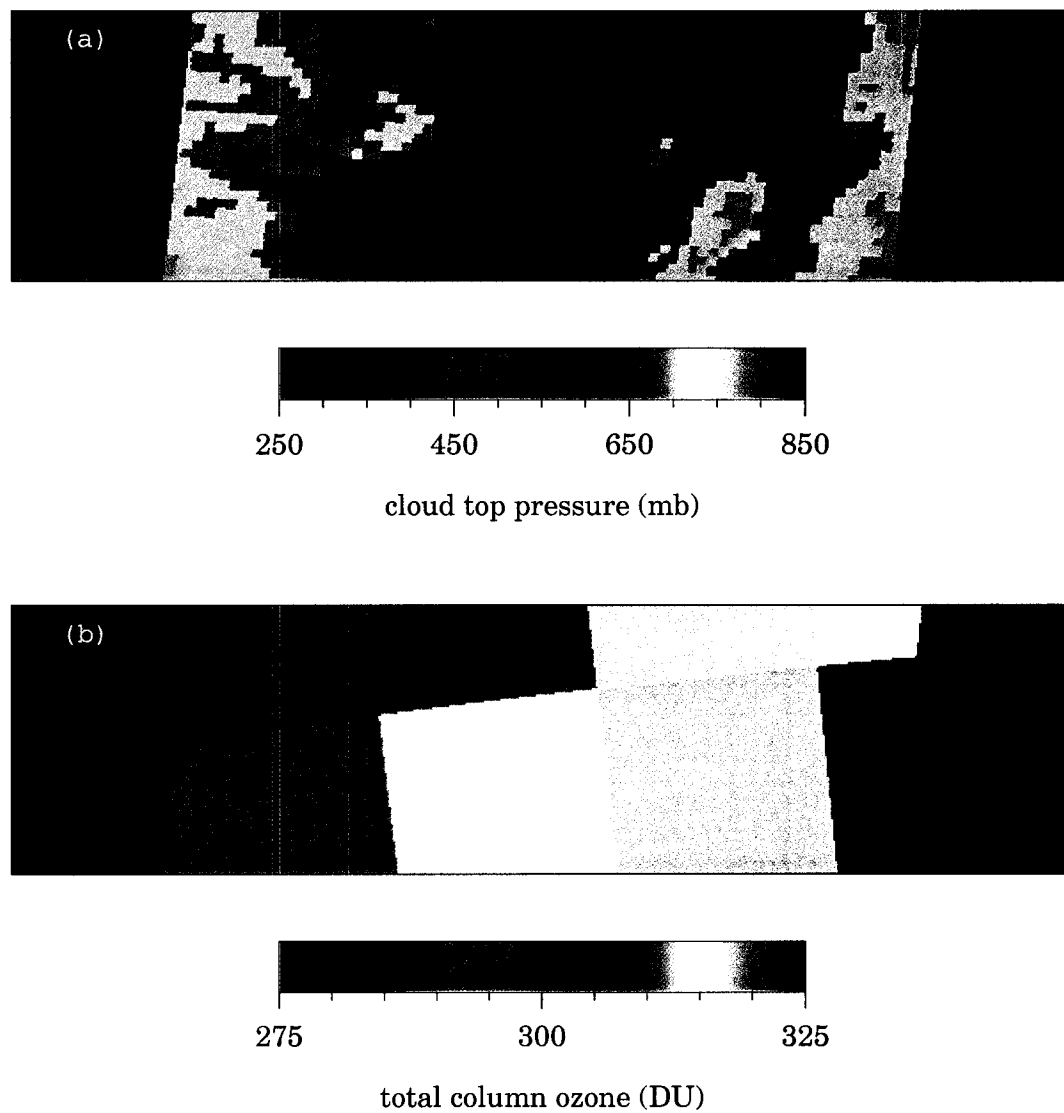


Figure F3 (a) Remapped MODIS cloud top pressure, and (b) remapped TOMS total column ozone for block 117 of orbit 15338. Magenta represents data void areas in both figures.

APPENDIX G: OFF-AXIS CORRECTION

Data produced on or prior to October 24, 2002 (orbit # ≤ 15155) contained significant calibration errors due to an error in the code used to derive the radiometric calibration coefficients. This so-called “off-axis” error resulted in a systematic change in the reflectances across the MISR swath. This error affected the nadir camera the most, which may have had absolute radiometric errors as large as 10% (too bright) at the left (western) edge of the scene, and –5% (too dim) at the right (eastern edge). Radiometry for other cameras, and at the swath center was in error to a lesser degree. The second set of 14 orbits (15330-15343) in my data set, produced on November 5, 2002 was already processed with the corrected calibration coefficients, hence it was not affected by the off-axis error. The original version of the first set of 14 orbits (6956-6969), processed on April 9, 2001, however, contained the off-axis error. These version F01_0007 data were reprocessed by the DAAC using the corrected calibration coefficients to obtain version F02_0017 data. The reprocessing, however, failed for orbit 6959, for which only the erroneous version F01_0007 data were available at the time of this study (since then the corrected F02_0018 version became available). Therefore, it was necessary to apply an approximate correction method for this orbit in this study. The following procedure was performed for each pixel in orbit 6959.

First, the original digital number (DN) was calculated from the calibration equation:

$$DN = g_{0,old} + g_{1,old}L_{old} + g_{2,old}L_{old}^2 . \quad (G1)$$

Here L_{old} is the original uncorrected radiance and $g_{0,old}$, $g_{1,old}$, and $g_{2,old}$ are the original erroneous calibration coefficients. Note that (G1) is a quadratic calibration equation, even though for orbit 6959 it reduced to a linear equation (i.e. $g_{0,old} = g_{2,old} = 0$ for this particular orbit). Then, the new off-axis corrected radiances, L_{new} , were computed from the original DN using the new strictly linear calibration equation with the corrected calibration coefficients $g_{1,new}$:

$$L_{new} = DN / g_{1,new} . \quad (G2)$$

Combining (G1) and (G2) yields the correction equation:

$$L_{new} = \frac{g_{1,old}}{g_{1,new}} L_{old} . \quad (G3)$$

Thus, the off-axis correction amounts to multiplying the original uncorrected radiances by the ratio of the old calibration coefficients to the new ones. A row (or line) of MISR data corresponds to the 1504 active elements of a MISR camera. During the MISR data processing these active sensor elements are mapped to the SOM grid to produce the imagery. In order to use (G3) the inverse transformation has to be used, that is one has to determine which particular active element, and thus calibration coefficient, a given image pixel corresponds to. In practice, it is not feasible to perform an exact back-projection

from the SOM grid to the active sensor elements. Instead, the following simple approximation was employed. First, the number and locations of non-fill image pixels in a row were determined. The number of these valid pixels fluctuates around 1504. Then, these non-fill pixels were mapped to the active sensor element range 1-1504 using linear interpolation.

The old (black) and new (blue) red band calibration coefficients are plotted in Figure G1a as a function of active sensor element for the most affected nadir camera. The ratio of these calibration coefficients is also plotted in this figure. Note that the actual calibration coefficients can change very abruptly from one sensor element to another, while their ratio, which is used as the correction factor in (G3), changes slowly and smoothly. This smooth behavior of the correction factor guarantees the good performance of the off-axis correction method even when the mapping between image pixels and active elements is only approximate. The correction factor for all nine cameras is plotted in Figure G1b. It is largest for the nadir camera but significant for the other cameras too. It increases from the left (western) edge of the swath to the right (eastern edge). An example of the off-axis correction is shown in Figure G2. Remapped MODIS reflectances were used as reference since they presumably did not suffer from the off-axis error. The red curve shows the absolute difference between the uncorrected MISR and the MODIS reflectances as a function of cross-track position. Note the systematic decrease and change in sign moving from the left edge to the right edge. The green curve shows the reflectance difference after applying the approximate MISR off-axis correction described in this chapter. Finally, the dotted black curve plots the reflectance difference

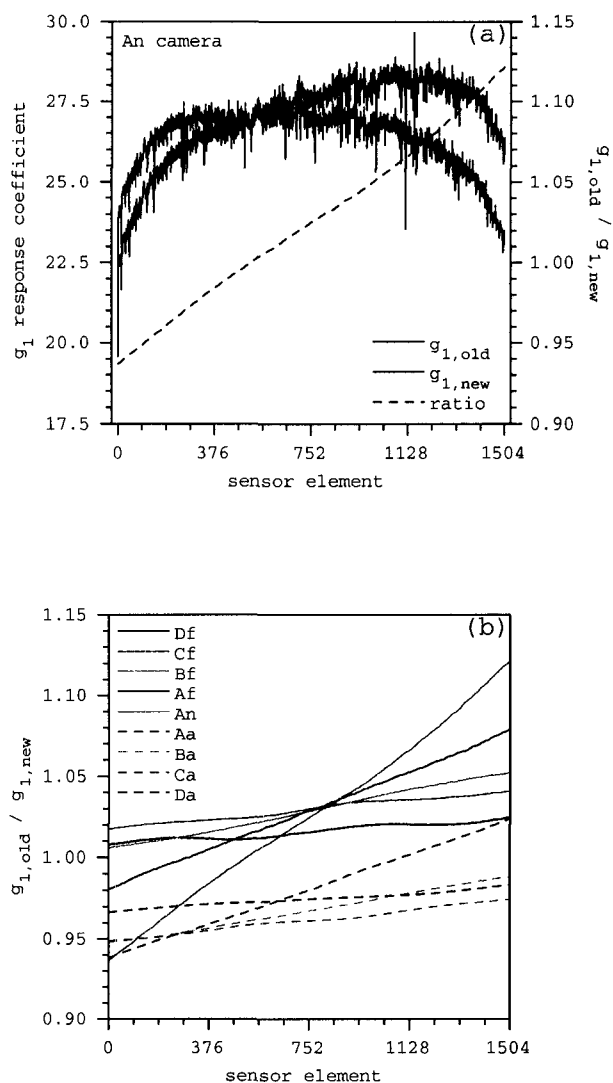


Figure G1 (a) Old and new calibration coefficients, and correction factor for the nadir camera, and (b) correction factors for the nine MISR cameras. The old coefficients are from MISR_AM1_ARP_INFLTCAL_T007_F02_0001.hdf, while the new coefficients are from MISR_AM1_ARP_INFLTCAL_T007_F02_SCF0012.hdf.

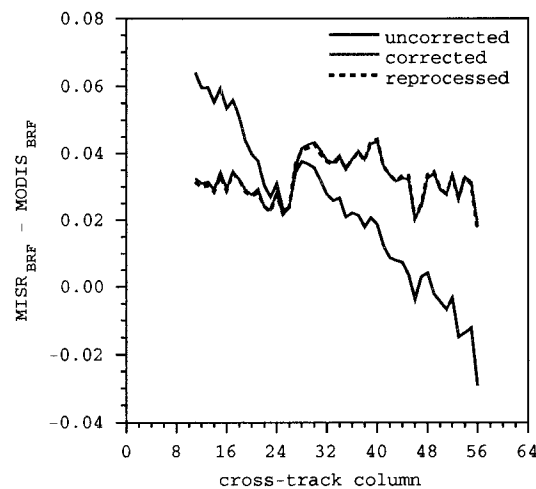


Figure G2 Off-axis calibration correction of block 116 of orbit 6968. The BRFs represent column averages of 2.2-km resolution nadir (A_n) data. No ozone or Rayleigh correction was applied. The red curve corresponds to uncorrected version F01_0007 MISR data. The green curve is version F01_0007 MISR data corrected with (G3). The dotted black line represents reprocessed version F02_0017 MISR data.

for MISR data reprocessed by the DAAC, which incorporates a proper mapping between sensor elements and image pixels. The excellent agreement between the latter two curves demonstrates the good performance of the approximate correction method. After the off-axis correction the reflectance difference does not show a systematic cross-track bias and fluctuates around a constant value of ~3%. This 3% absolute reflectance difference is partly due to the different spectral characteristics (bandpass, response function, etc.) of the MISR and MODIS red bands, which result in atmospheric effects of different magnitudes. The reflectance difference is likely to be smaller when Rayleigh scattering and ozone absorption effects are removed. The sign and magnitude of the discrepancy between MISR and MODIS reflectances is consistent with other studies, which found that MISR measurements generally exceed MODIS observations by a couple of percent (Bruegge, personal communication).

REFERENCES

- Abdou, W. A., C. J. Bruegge, M. C. Helmlinger, J. E. Conel, S. H. Pilorz, W. Ledeboer, B. J. Gaitley, and K. J. Thome, Vicarious calibration experiment in support of the Multi-angle Imaging SpectroRadiometer, *IEEE Trans. Geosci. Remote Sensing*, 40(7), 1500-1511, 2002.
- Ackerman, T. P., D. M. Flynn, and R. T. Marchand, Quantifying the magnitude of anomalous solar absorption, *J. Geophys. Res.*, 108(D9), 4273, doi:10.1029/2002JD002674, 2003.
- Adams, C. N., and G. W. Kattawar, Solutions of equations of radiative transfer by an invariant imbedding approach, *J. Quant. Spectrosc. Radiat. Transfer*, 10(5), 341-&, 1970.
- Akvilonova, A. B., A. Y. Basharinov, A. K. Gorodetskiy, A. S. Gurvich, M. S. Krylova, B. G. Kutuza, D. T. Matveyev, and A. P. Orlov, Cloud parameters measured from the Cosmos-384 satellite, *Atmos. Oceanic Phys.*, 9, 187-189, 1973.
- Amoruso, A., M. Cacciani, A. Di Sarra, and G. Fiocco, Absorption cross sections of ozone in the 590- to 610-nm region at T=230 K and T=299 K, *J. Geophys. Res.*, 95(D12), 20,565-20,568, 1990.
- Atkinson, B. W., *Mesoscale atmospheric circulation*, Academic Press, New York, 1981.
- Berk, A., L. S. Bernstein, and D. C. Robertson, MODTRAN: A moderate resolution model for LOWTRAN 7, Air Force Geophysical Laboratory Technical Report GL-TR-83-0187, Hanscom Air Force Base, MA 01731-5000, 1983.
- Berry, E., and R. Reinhardt, An analysis of cloud drop growth by collection, *J. Atmos. Sci.*, 31, 1814-1831, 1974.
- Blaskovic, M., R. Davies, and J. B. Snider, Diurnal variation of marine stratocumulus over San Nicolas Island during July 1987, *Mon. Weather Rev.*, 119(6), 1469-1478, 1991.

- Boers, R., and L. D. Rotstajn, Possible links between cloud optical depth and effective radius in remote sensing observations, *Q. J. R. Meteorol. Soc.*, 127, 2367-2383, 2001.
- Boers, R., H. Russchenberg, J. Erkelens, V. Venema, A. van Lammeren, A. Apituley, and S. Jongen, Ground-based remote sensing of stratocumulus properties during CLARA-1996, *J. Appl. Meteorol.*, 39, 169-181, 2000.
- Boers, R., J. B. Jensen, and P. B. Krummel, Microphysical and radiative structure of marine stratocumulus clouds over the Southern Ocean: Summer results and seasonal differences, *Q. J. R. Meteorol. Soc.*, 124, 151-168, 1998.
- Borovikov, A. M., *Cloud physics*, Transl. Israel Program Sci. Transl. Jerusalem, US Dep. Commerce, Office Tech. Serv., Washington D.C.
- Breon, F.-M., and P. Goloub, Cloud droplet effective radius from spaceborne polarization measurements, *Geophys. Res. Lett.*, 25(11), 1879-1882, 1998.
- Breon, F.-M., and S. Colzy, Global distribution of cloud droplet effective radius from POLDER polarization measurements, *Geophys. Res. Lett.*, 27(24), 4065-4068, 2000.
- Bruegge, C. J., N. L. Chrien, R. R. Ando, D. J. Diner, W. A. Abdou, M. C. Helmlinger, S. H. Pilorz, and K. J. Thome, Early validation of the Multi-angle Imaging SpectroRadiometer (MISR) radiometric scale, *IEEE Trans. Geosci. Remote Sensing*, 40(7), 1477-1492, 2002.
- Burkholder, J. B., and R. K. Talukdar, Temperature dependence of the ozone absorption spectrum over the wavelength range 410 to 760 nm, *Geophys. Res. Lett.*, 21(7), 581-584, 1994.
- Cess, R. D., and Coauthors, Absorption of solar radiation by clouds: Observations versus models, *Science*, 267, 496-499, 1995.
- Cess, R. D., and Coauthors, Cloud feedback in atmospheric general circulation models: An update, *J. Geophys. Res.*, 101(D8), 12791-12794, 1996.

- Cess, R. D., and Coauthors, Intercomparison and interpretation of climate feedback processes in 19 atmospheric general circulation models, *J. Geophys. Res.*, 95, 16601-16615, 1990.
- Chandrasekhar, S., *Radiative transfer*, Dover, New York, 1960.
- Chrien, N. L., C. J. Bruegge, and R. R. Ando, Multi-angle Imaging SpectroRadiometer (MISR) on-board calibrator (OBC) in-flight performance studies, *IEEE Trans. Geosci. Remote Sensing*, 40(7), 1493-1499, 2002.
- Churchill, D. D., and R. A. Houze, Mesoscale updraft magnitude and cloud ice content deduced from the ice budget of the stratiform region of a tropical cloud cluster, *J. Atmos. Sci.*, 41, 1717-1725, 1984.
- Colton, M. C., and G. A. Poe, Intersensor calibration of DMSP SSM/I's: F-8 to F-14, 1987-1997, *IEEE Trans. Geosci. Remote Sensing*, 37(1), 418-439, 1999.
- Cotton, W. R., and R. A. Anthes, *Storm and cloud dynamics*, International Geophysics Series, Vol. 44, Academic Press, 883 pp., 1989.
- De Bary, E., and F. Möller, Die mittlere vertikale Verteilung von Wolken in Abhängigkeit von der Wetterlage, *Ber. deut. Wetterdienstes*, No. 67, 1-27, 1960.
- De Bary, E., and F. Möller, The vertical distribution of clouds, *J. Appl. Meteorol.*, 2, 806-808, 1963.
- Diner, D. J., J. C. Beckert, G. W. Bothwell, and J. I. Rodriguez, Performance of the MISR instrument during its first 20 months in Earth orbit, *IEEE Trans. Geosci. Remote Sensing*, 40(7), 1449-1466, 2002.
- Diner, D. J., J. C. Beckert, T. H. Reilly, C. J. Bruegge, J. E. Conel, R. A. Kahn, J. V. Martonchik, T. P. Ackerman, R. Davies, S. A. W. Gerstl, H. R. Gordon, J.-P. Muller, R. B. Myneni, P. J. Sellers, B. Pinty, and M. M. Verstraete, Multi-angle Imaging SpectroRadiometer (MISR) instrument description and experiment overview, *IEEE Trans. Geosci. Remote Sensing*, 36(4), 1072-1087, 1998.

- Diner, D., W. Abdou, T. Ackerman, K. Crean, H. Gordon, R. Kahn, J. Martonchik, S. McMuldroy, S. Paradise, B. Pinty, M. Verstraete, M. Wang, and R. West, MISR: Level 2 Aerosol Retrieval Algorithm Theoretical Basis, JPL D-11400, Rev. E, April 10, 2001.
- Evans, K. F., The spherical harmonic discrete ordinate method for three-dimensional atmospheric radiative transfer, *J. Atmos. Sci.*, 55, 429-446, 1998.
- Feingold, G., and Z. Levin, The lognormal fit to raindrop spectra from frontal convective clouds in Israel, *J. Clim. Appl. Meteorol.*, 25, 1346-1363, 1986.
- Ferraro, R. R., F. Z. Weng, N. C. Grody, and A. Basist, An eight-year (1987-1994) time series of rainfall, clouds, water vapor, snow-cover, and sea-ice derived from SSM/I measurements, *Bull. Amer. Meteor. Soc.*, 77(5), 891-905, 1996.
- Gaut, N. E., and E. C. Reifstein, III, Interaction model of microwave energy and atmospheric variables, ERT Tech. Rep. No. 13, Environmental Research and Technology, Inc., 65-66, 1971.
- Gerber, H., Microphysics of marine stratocumulus clouds with two drizzle modes, *J. Atmos. Sci.*, 53, 1649-1662, 1996.
- Glickman, T. S., editor, *Glossary of meteorology*, 2nd ed., 855 pp., American Meteorological Society, Boston, Massachusetts, 2000.
- Gorelik, A. G., and V. V. Kalashnikov, Determination of integrated water content of rain clouds and of rain layer height by a superhigh-frequency radiometric method, *Advances in Satellite Meteorology 2*, Wiley and Sons, New York, 1971.
- Greenwald, T. J., G. L. Stephens, S. A. Christopher, and T. H. Vonder Haar, Observations of the global characteristics and regional radiative effects of marine cloud liquid water, *J. Climate*, 8, 2928-2946, 1995.

- Greenwald, T. J., G. L. Stephens, T. H. Vonder Haar, and D. L. Jackson, A physical retrieval of cloud liquid water over the global oceans using Special Sensor Microwave/Imager (SSM/I) observations, *J. Geophys. Res.*, 98(D10), 18471-18488, 1993.
- Gultepe, I., G. A. Isaac, and K. B. Strawbridge, Variability of cloud microphysical and optical parameters obtained from aircraft and satellite remote sensing measurements during RACE, *Int. J. Climatol.*, 21, 507-525, 2001.
- Hahn, C. J., W. B. Rossow, and S. G. Warren, ISCCP cloud properties associated with standard cloud types identified in individual surface observations, *J. Climate.*, 14, 11-28, 2001.
- Han, Q., W. B. Rossow, and A. A. Lacis, Near-global survey of effective droplet radii in liquid water clouds using ISCCP data, *J. Climate*, 7, 465-497, 1994.
- Hansen, J. E., and L. D. Travis, Light scattering in planetary atmospheres, *Space Sci. Rev.*, 16, 527-610, 1974.
- Hansen, J. E., Multiple scattering of polarized light in planetary atmospheres. Part II. Sunlight reflected by terrestrial water clouds, *J. Atmos. Sci.*, 28, 1400-1426, 1971.
- Hegg, D. A., Comments on "The effects of very large drops on cloud absorption. Part I: parcel models", *J. Atmos. Sci.*, 43(4), 399-400, 1986.
- Henderson-Sellers, A., and K. McGuffie, Are cloud amounts estimated from satellite sensor and conventional surface-based observations related?, *Int. J. Remote Sens.*, 11, 543-550, 1990.
- Hess, M., P. Koepke, and I. Schult, Optical Properties of Aerosols and Clouds: the software package OPAC, *Bull. Amer. Meteor. Soc.*, 79(5), 831-844, 1998.
- Ho, S.-P., B. Lin, P. Minnis, and T.-F. Fan, Estimates of cloud vertical structure and water amount over tropical oceans using VIRS and TMI data, *J. Geophys. Res.*, 108(D14), 4419, doi:10.1029/2002JD003298, 2003.

- Horváth, Á., and R. Davies, Anisotropy of water cloud reflectance: A comparison of measurements and 1D theory, *Geophys. Res. Lett.*, 31, L01102, doi:10.1029/2003GL018386, 2004.
- Horváth, Á., and R. Davies, Feasibility and error analysis of cloud motion wind extraction from near-simultaneous multiangle MISR measurements, *J. Atmos. Oceanic Technol.*, 18, 591-608, 2001.
- Houghton, J. T., Y. Ding, D. J. Griggs, M. Noguer, P. J. van der Linder, and D. Xiaosu, Eds., *Climate Change 2001: The scientific basis*, Cambridge University Press, 944 pp., 2001.
- Hulme, M., Estimating global changes in precipitation, *Weather*, 50(2), 34-42, 1995.
- Junge, C., *Atmospheric chemistry and radioactivity*. Academic Press, New York, 1963.
- Kalashnikov, V. V., and Y. A. Frolov, Prospects for determining rain intensities by the thermal atmospheric emission in the millimeter and centimeter bands, *Advances in Satellite Meteorology* 2, Wiley and Sons, New York, 1971.
- Karstens, U., C. Simmer, and E. Ruprecht, Remote sensing of cloud liquid water, *Meteorol. Atmos. Phys.*, 54, 157-171, 1994.
- Kessler, E., and D. Atlas, Model precipitation distributions, *Aerospace Eng.*, 18(12), 36-40, 1959.
- King, M. D., Determination of the scaled optical thickness of clouds from reflected solar radiation measurements, *J. Atmos. Sci.*, 44, 1734-1751, 1987.
- King, W. D., D. A. Parkin, and R. J. Handsworth, A hot wire water device having fully calculable response characteristics, *J. Appl. Meteorol.*, 17, 1809-1813, 1978.

- Knollenberg, R. G., Techniques for probing cloud microstructure, in *Clouds: their formation, optical properties and effects*, Hobbs, P. V. and A. Deepak, Eds., Academic Press, p. 15-19, 1981.
- Knollenberg, R. G., Three new instruments for cloud physics measurements, in *Preprints International Conference on Cloud Physics*, Boulder, Colorado, USA, Amer. Meteor. Soc., p. 544, 1976.
- Korolev, A. V., J. W. Strapp, G. A. Isaac, and A. N. Nevzorov, The Nevzorov airborne hot wire LWC/TWC probe: Principal of operation and performance characteristics, *J. Atmos. Oceanic Technol.*, 15, 1495-1510, 1998.
- Lacis, A. A., and V. Oinas, A description of the correlated k distribution method for modeling nongray gaseous absorption, thermal emission, and multiple scattering in vertically inhomogeneous atmospheres, *J. Geophys. Res.*, 96(D5), 9027-9063, 1991.
- Lelieveld, J., P. J. Crutzen, H. Rodhe, Zonal average cloud characteristics for global atmospheric modeling, *Rep. CM-76*, Dep. Meteorol. Univ. Stockholm, Sweden, 1989.
- Lenoble, J., *Atmospheric radiative transfer*, 532 pp., A. Deepak Publishing, Hampton, Virginia, 1993.
- Lin, B., and W. B. Rossow, Observations of cloud liquid water path over oceans: optical and microwave remote sensing methods, *J. Geophys. Res.*, 99, 20907-20927, 1994.
- Lin, B., and W. B. Rossow, Precipitation water path and rainfall rate estimates over oceans using special sensor microwave imager and International Satellite Cloud Climatology Project data, *J. Geophys. Res.*, 102(D8), 9359-9374, 1997.
- Liu, G., and J. A. Curry, Determination of characteristic features of cloud liquid water from satellite microwave measurements, *J. Geophys. Res.*, 98(D3), 5069-5092, 1993.
- Liu, G., and J. A. Curry, Retrieval of precipitation from satellite microwave measurements using both emission and scattering, *J. Geophys. Res.*, 97, 9959-9974, 1992.

- Loeb, N. G., and R. Davies, Observational evidence of plane parallel model biases: Apparent dependence of cloud optical depth on solar zenith angle, *J. Geophys. Res.*, 101, 1621-1634, 1996.
- Los, A., and P. G. Duynkerke, Microphysical and radiative properties of inhomogeneous stratocumulus: Observations and model simulations, *Q. J. R. Meteorol. Soc.*, 126, 3287-3307, 2000.
- Lovejoy, S., and G. L. Austin, The estimation of rain from satellite-borne microwave radiometers, *Quart. J. R. Met. Soc.*, 106, 255-276, 1980.
- Macke, A., J. Mueller, and E. Raschke, Single scattering properties of atmospheric ice crystals, *J. Atmos. Sci.*, 53, 2813-2825, 1996.
- Marshall, T. S., and W. Palmer, The distribution of raindrops with size, *J. Meteor.*, 5, 165-166, 1948.
- Mason, B. J., *The physics of clouds*, Oxford Press, 1971.
- Masunaga, H., T. Y. Nakajima, T. Nakajima, M. Kachi, R. Oki, and S. Kuroda, Physical properties of maritime low clouds as retrieved by combined use of Tropical Rainfall Measurement Mission Microwave Imager and Visible/Infrared Scanner: Algorithm, *J. Geophys. Res.*, 107(D10), 10.1029/2001JD000743, 2002.
- Matveev, L. T., *Cloud dynamics*, Reidel, Dordrecht, 1984.
- Miles, N. L., J. Verlinde, and E. E. Clothiaux, Cloud droplet size distributions in low-level stratiform clouds, *J. Atmos. Sci.*, 57, 295-311, 2000.
- Minnis, P., K.-N. Liou, and Y. Takano, Inference of cirrus cloud properties using satellite-observed visible and infrared radiances. Part I: Parameterization of radiance fields, *J. Atmos. Sci.*, 50(9), 1279-1304, 1993a.

- Minnis, P., P. W. Heck, and D. F. Young, Inference of cirrus cloud properties using satellite-observed visible and infrared radiances. Part II: Verification of theoretical cirrus radiative properties, *J. Atmos. Sci.*, 50(9), 1305-1322, 1993b.
- Mishchenko, M. I., A. A. Lacis, and L. D. Travis, Errors induced by the neglect of polarization in radiance calculations for Rayleigh-scattering atmospheres, *J. Quant. Spectrosc. Radiat. Transfer*, 51(3), 491-510, 1994.
- Mishchenko, M. I., W. B. Rossow, A. Macke, and A. A. Lacis, Sensitivity of cirrus cloud albedo, bi-directional reflectance, and optical thickness retrieval accuracy to ice-particle shape, *J. Geophys. Res.*, 101, 16973-16985, 1996.
- Morgan, P. H., L. P. Mercer, and N. W. Flodin, General model for nutritional responses of higher organisms, *Proc. Natl. Acad. Sci. USA*, 72, 4327-4331, 1975.
- Mugnai, A., and E. A. Smith, Radiative transfer to space through a precipitating cloud at multiple microwave frequencies, Part I: Model description, *J. Appl. Meteorol.*, 27, 1055-1073, 1988.
- Nakajima, T., and M. D. King, Determination of the optical thickness and effective particle radius of clouds from reflected solar radiation measurements. Part I: Theory, *J. Atmos. Sci.*, 47, 1878-1893.
- Nakajima, T., M. D. King, and J. D. Spinhirne, Determination of the optical thickness and effective particle radius of clouds from reflected solar radiation measurements. Part II: Marine stratocumulus observations, *J. Atmos. Sci.*, 48, 728-750, 1991.
- Nevzorov, A. N., Aircraft cloud water content meter, in *Communications à la 8ème Conférence Internationale sur la Physique des Nuages*, vol. II, pp. 701-703, Clermont-Ferrand, France, 1980.
- NIMA, Department of Defense World Geodetic System 1984, its definition and relationships with local geodetic systems, NIMA Tech. Rep. TR8350.2, 3d ed., 175 pp., 1997. [Available from the National Imaging and Mapping Agency's (NIMA) Operational Help Desk (ESICS/L-88), 3200 South Second Street, St. Louis, MO 63118-3399; also available online at <http://www.nima.mil>].

- Njoku, E. G., and L. Swanson, Global measurements of sea surface temperature, wind speed, and atmospheric water content from satellite microwave radiometry, *Mon. Weather Rev.*, 111, 1977-1987, 1983.
- Oelke, C., Mikrowellenfernerkundung des Wolkenwassergehaltes über dem Atlantik mit Satellitendaten. Diplomarbeit am Institut für Meereskunde an der Christian-Albrechts-Universität Kiel, 90 p.
- Pandey, P. C., E. G. Njoku, and J. W. Waters, Inference of cloud temperature and thickness by microwave radiometry from space, *J. Clim. Appl. Meteorol.*, 22, 1894-1898, 1983.
- Panegrossi, G., and Coauthors, Use of cloud model microphysics for passive microwave-based precipitation retrieval: Significance of consistency between model and measurement manifolds, *J. Atmos. Sci.*, 55, 1644-1673, 1998.
- Peixoto, J. P., and A. H. Oort, *Physics of climate*, Amer. Inst. Phys., 520 pp., 1992.
- Pilewskie, P., and F. P. J. Valero, Direct observations of excess solar absorption by clouds, *Science*, 267, 1626-1629, 1995.
- Platnick, S., and F. P. J. Valero, A validation of a satellite cloud retrieval during ASTEX, *J. Atmos. Sci.*, 52(16), 2985-3001, 1995.
- Poore, K. D., J. Wang, and W. B. Rossow, Cloud layer thicknesses from a combination of surface and upper-air observations, *J. Climate*, 8, 550-568, 1995.
- Pruppacher, H. R., and D. J. Klett, *Microphysics of clouds and precipitation*, Reidel, Dordrecht, 1978.
- Pruppacher, H. R., and R. Jaenicke, The processing of water vapor and aerosols by atmospheric clouds, a global estimate, *Atmospheric Research*, 38, 283-295, 1995.

- Ramanathan, V., B. Subasilar, G. J. Zhang, W. Conant, R. D. Cess, J. T. Kiehl, H. Grassl, and L. Shi, Warm pool heat budget and shortwave cloud forcing: A missing physics?, *Science*, 267, 499-503, 1995.
- Ricchiazzi, P., S. Yang, C. Gautier, and D. Sowle, SBDART: a research and teaching software tool for plane-parallel radiative transfer in the earth's atmosphere, *Bull. Amer. Meteor. Soc.*, 79(10), 2101-2114, 1998.
- Roeckner , E., L. Dümenil, E. Kirk, F. Lunkeit, M. Ponater, B. Rockel, R. Sausen, and U. Schlese, The Hamburg version of the ECMWF model (ECHAM). In: Boer, G. J. (ed.) *Research Activities in Atmospheric and Ocean Modeling CAS/JSC Working Group on Numerical Experimentation*, 13, 7.1-7.4, 1989.
- Roeckner , E., M. Rieland, and E. Kemp, Modeling of clouds and radiation in the ECHAM model. In: ECMWF/WCRP workshop on clouds, radiative transfer and the hydrological cycle, 199-222, 1991.
- Rosenfeld, D., and G. Gutman, Retrieving microphysical properties near the tops of potential rain clouds by multispectral analysis of AVHRR data, *Atmospheric Research*, 34, 259-283, 1994.
- Rosenfeld, D., and I. M. Lensky, Satellite-based insights into precipitation formation processes in continental and maritime convective clouds, *Bull. Amer. Meteor. Soc.*, 79(11), 2457-2476, 1998.
- Rosenfeld, D., TRMM observed first direct evidence of smoke from forest fires inhibiting rainfall, *Geophys. Res. Lett.*, 26(20), 3105-3108, 1999.
- Rossow, W. B., A. W. Walker, and L. C. Garder, Comparison of ISCCP and other cloud amounts, *J. Climate.*, 6, 2394-2418, 1993.
- Rossow, W. B., A. W. Walker, D. E. Beuschel, and M. D. Roiter, International Satellite Cloud Climatology Project (ISCCP) documentation of new cloud datasets, WMO/TD-No. 737, World Meteorological Organization, 115 pp., 1996. [Available at <http://isccp.giss.nasa.gov/docs/documents.html>].

- Rossow, W. B., and R. A. Schiffer, Advances in understanding clouds from ISCCP. *Bull. Amer. Meteor. Soc.*, 80, 2261-2287, 1999.
- Rossow, W. B., and R. A. Schiffer, ISCCP cloud data products, *Bull. Amer. Meteor. Soc.*, 72, 2-20, 1991.
- Rossow, W. B., Cloud microphysics: Analysis of the clouds of Earth, Venus, Mars, and Jupiter, *Icarus*, 36, 1-50, 1978.
- Sauvageot, H., and J. P. Lacaux, The shape of averaged drop size distributions, *J. Atmos. Sci.*, 52, 1070-1083, 1995.
- Savijärvi, H., A. Arola, and P. Räisänen, Short-wave optical properties of precipitating water clouds, *Q. J. R. Meteorol. Soc.*, 123, 883-899, 1997.
- Sengupta, M., and T. P. Ackerman, Investigating anomalous absorption using surface measurements, *J. Geophys. Res.*, 108(D24), 4761, doi:10.1029/2003JD003411, 2003.
- Sheu, R.-S., J. A. Curry, and G. Liu, Vertical stratification of tropical cloud properties as determined from satellite, *J. Geophys. Res.*, 102(D4), 4231-4245, 1997.
- Slingo, A., and H. M. Schrecker, On the shortwave radiative properties of stratiform water clouds, *Q. J. R. Meteorol. Soc.*, 108, 407-426, 1982.
- Smith, E. A., A. Mugnai, H. J. Cooper, G. J. Tripoli, and X. Xiang, Foundations for statistical-physical precipitation retrieval from passive microwave satellite measurements I: Brightness-temperature properties of a time dependent cloud-radiation model, *J. Appl. Meteorol.*, 31, 506-531, 1992.
- Stamnes, K., and S.-C. Tsay, Optimum spectral resolution for computing atmospheric heating and photodissociation rates, *Planet. Space Sci.*, 38(6), 807-820, 1990.

- Stamnes, K., S.-C. Tsay, W. J. Wiscombe, and K. Jayaweera, Numerically stable algorithm for discrete-ordinate-method radiative transfer in scattering and emitting layered media, *Applied Optics*, 27, 2502-2509, 1988.
- Stepanenko, V. D., Contrasts of radio brightness temperatures in clouds and precipitation, *Transfer of microwave radiation in the atmosphere*, US Dept. of Commerce, Springfield, Va.
- Stephens, G. L., Optical properties of eight water cloud types, CSIRO Division of Atmospheric Physics, Technical Paper number 36.
- Stephens, G. L., *Remote sensing of the lower atmosphere: an introduction*, 523 pp., Oxford University Press, New York, New York, 1994.
- Sun, Z., and L. Rikus, Improved application of exponential sum fitting transmissions to inhomogeneous atmosphere, *J. Geophys. Res.*, 104(D6), 6291 p., 1999.
- Teillet, P. M., Rayleigh optical depth comparisons from various sources, *Appl. Opt.*, 29(13), 1897-1900, 1990.
- Thomas, G. E., and K. Stamnes, *Radiative transfer in the atmosphere and ocean*, 517 pp., Cambridge University Press, New York, NY, 1999.
- van de Hulst, H. C., *Multiple light scattering*, 739 pp., Academic Press, San Diego, California, 1980.
- Wang, J., W. B. Rossow, and Y. Zhang, Cloud vertical structure and its variations from a 20-yr global rawinsonde dataset, *J. Climate*, 13, 3041-3056, 2000.
- Wang, M., and M. D. King, Correction of Rayleigh scattering effects in cloud optical thickness retrievals, *J. Geophys. Res.*, 102(D22), 25,915-25,926, 1997.
- Warner, J., The water content of cumuliform clouds, *Tellus*, 7, 449-457, 1955.

- Warren, S. G., C. J. Hahn, and J. London, Simultaneous occurrence of different cloud types, *J. Clim. Appl. Meteorol.*, 24, 658-667, 1985.
- Warren, S. G., C. J. Hahn, J. London, R. M. Chervin, and R. L. Lenne, Global distribution of total cloud cover and cloud type amounts over land, NCAR Techn. Note, NCAR/TN-273+STR, Natl. Center Atmos. Res., Boulder, Colorado, 1986.
- Weng, F., and N. C. Grody, Retrieval of cloud liquid water using the Special Sensor Microwave Imager (SSM/I), *J. Geophys. Res.*, 99(D12), 25535-25551, 1994.
- Wentz, F. J., A well-calibrated ocean algorithm for SSM/I, *J. Geophys. Res.*, 102, 8703-8718, 1997.
- Wentz, F. J., and R. W. Spencer, SSM/I rain retrievals within a unified all-weather ocean algorithm, *J. Atmos. Sci.*, 55, 1613-1627, 1998.
- Wielicki, B. A., B. R. Barkstrom, E. F. Harrison, R. B. Lee III, G. L. Smith, and J. E. Cooper, Clouds and the Earth's Radiant Energy System (CERES): An Earth Observing System experiment, *Bull. Amer. Meteor. Soc.*, 77(5), 853-868, 1996.
- Wielicki, B. A., R. D. Cess, M. D. King, D. A. Randall, and E. F. Harrison, Mission to planet earth: Role of clouds and radiation in climate, *Bull. Amer. Meteor. Soc.*, 76(11), 2125-2153, 1995.
- Wiscombe, W. J., R. M. Welch, and W. D. Hall, The effects of very large drops on cloud absorption. Part I: parcel models, *J. Atmos. Sci.*, 41(8), 1336-1355, 1984.
- World Climate Research Programme (WCRP) Publication Series No. 7, WMO ITD-No. 149, pp. 119-126, October 1986. The data were compiled by Christoph Wehrli, World Radiation Center (NRC), Davos-Dorf, Switzerland under WRC Publication No. 615, July 1985.